LASER-ASSISTED SCANNING PROBE ALLOYING NANOLITHOGRAPHY (LASPAN) AND ITS APPLICATION IN GOLD-SILICON SYSTEM

A Dissertation

by

LUOHAN PENG

Submitted to the Office of Graduate Studies of
Texas A&M University
in partial fulfillment of the requirements for the degree of

DOCTOR OF PHILOSOPHY

August 2008

Major Subject: Materials Science and Engineering

LASER-ASSISTED SCANNING PROBE ALLOYING NANOLITHOGRAPHY (LASPAN) AND ITS APPLICATION IN GOLD-SILICON SYSTEM

A Dissertation

by

LUOHAN PENG

Submitted to the Office of Graduate Studies of
Texas A&M University
in partial fulfillment of the requirements for the degree of

DOCTOR OF PHILOSOPHY

Approved by:

Co-Chairs of Committee,	Hong Liang
	Winfried Teizer
Committee Members,	Philip R. Hemmer
	Joseph H. Ross Jr.
Chair of Materials Science and Engineering Program,	Tahir Cagin

August 2008

Major Subject: Materials Science and Engineering

ABSTRACT

Laser-Assisted Scanning Probe Alloying Nanolithography (LASPAN) and Its Application in Gold-Silicon System. (August 2008)

Luohan Peng, B.S., Wuhan University;

M.S., Texas A&M University

Co-Chairs of Advisory Committee, Dr. Hong Liang
Dr. Winfried Teizer

Nanoscale science and technology demand novel approaches and new knowledge to further advance. Nanoscale fabrication has been widely employed in both modern science and engineering. Micro/nano lithography is the most common technique to deposit nanostructures. Fundamental research is also being conducted to investigate structural, physical and chemical properties of the nanostructures. This research contributes fundamental understanding in surface science through development of a new methodology. Doing so, experimental approaches combined with energy analysis were carried out. A delicate hardware system was designed and constructed to realize the nanometer scale lithography. We developed a complete process, namely laser-assisted scanning probe alloying nanolithography (LASPAN), to fabricate well-defined nanostructures in gold-silicon (Au-Si) system. As a result, four aspects of nanostructures were made through different experimental trials. A non-equilibrium phase ($AuSi_3$) was discovered, along with a non-equilibrium phase diagram. Energy dissipation and mechanism of nanocrystalization in the process have been extensively discussed. The

mechanical energy input and laser radiation induced thermal energy input were estimated. An energy model was derived to represent the whole process of LASPAN.

To my beloved wife and my parents

ACKNOWLEDGEMENTS

I would like to thank both of my committee chairs, Dr. Liang and Dr. Teizer, and my committee members, Dr. Hemmer and Dr. Ross, for their guidance and support throughout the course of this research. I would like to extend my special thanks to Dr. Liang, my primary research advisor. She provided unlimited resources for me to complete my dissertation. Not only did I learn how to solve technical problems, but I also learned how to be a good scholar.

Special thanks goes to my beloved fiancée, Dr. Fuhui Tong, for her persistent love and help. We spent countless time together studying and working. We got through a lot of hard times until we finally reached our destination. Her sincere love was my best support behind all hard work.

Many thanks go to my friends and colleagues and the department faculty and staff for making my time at Texas A&M University a great experience. Dr. Lin Shao, my best friend, helped me with special experiments, as well as educated me through our discussions. Mr. Huiliang Zhang, my collaborator, helped me set up most of the important facilities with his expertise. Miss Jan Gerston, my graduate advisor, offered tremendous help in all kinds of administrative issues. Thanks to the whole surface science group in the Mechanical Engineering Department and the whole Nanolab group in Physics Department. I enjoyed the time spent in both groups. I also appreciate my many other friends and colleagues who helped me to accomplish my research.

Finally, genuine thanks to my mother Mrs. Hui Luo and father Mr. Xiaoxiu Peng for their continuous encouragement and support. Their true love is always with me along the road. I wish my parents all the best in their life!

TABLE OF CONTENTS

CHAPTER Page

LIST OF FIGURES

FIGURE Page

FIGURE Page

FIGURE Page

LIST OF TABLES

CHAPTER I

INTRODUCTION

In his classic lecture in 1959, Richard P. Feynman[1] suggested fabricating small devices by manipulating matter at the atomic level, a process now referred to as nanomanufacturing. Major breakthroughs in recent years in nanoscience and engineering have further advanced nanomanufacturing. Nanomanufacturing is capable of making structures, patterns and objects at nanometer scale using a number of techniques, such as lithography[2] , vapor-liquid-solid (VLS) process[3], chemical vapor deposition (CVD)[4-7], molecular beam epitaxy (MBE)[8-10], and scanning probe based lithography[11]. Nanostructures fabricated through nanomanufacturing are nanoparticles[12], nanotubes[13], nanofibers[14] and nanowires[15].

Metallic nanostructure fabrication has attracted particular interest in many industries, including semiconductor manufacturing, integrated circuit (IC) fabrication, and micro/nano electromechanical systems (MEMS/NEMS)[16]. Among existing techniques, the micro/nano lithography is one of the most common techniques to deposit nanostructures.[17-19]

This dissertation follows the style of Applied Physical Letters.

This chapter reviews the techniques of lithography, its history, advantages, and the state-of-the art. After that, related fundamental issues such as wear mechanism during the process will be discussed. To date, the fundamental understanding has focused on the structural, physical and chemical properties of nanostructures[20-23]. This chapter will provide an overview of those aspects.

1.1 Review of lithographic techniques at nanometer scale

Lithographic techniques at nanometer scale include optical lithography, electron beam lithography (EBL), focused ion beam (FIB) lithography and scanning probe microscope (SPM) based nanolithography. Lithography literally means "writing on stone." The basic principle of lithography was first investigated by an Austrian author Alois Senefelder[24], and the technique experienced an explosive boost in the mid-20th century. The history of developed lithographic techniques[17] can be found in Table 1.

Table 1 History of developed lithographic techniques

Technique	Representing Author(s)	First Started Year
Lithography	A. Senefelder	1798
Optical Lithography	G. Moore	1965
Electron Beam Lithography	D.A.Buck et al.	1957
X-ray Lithography	E. Spears et al.	1972
Extreme Ultraviolet Lithography	A.M. Hawryluk et al.	1988
Imprint Lithography	G. Whitesides et al.	1994
Scanning Probe Microscope Based Lithography	M. Ringger et al.	1985

In modern nanoscience and engineering, a critical issue is to create metallic nanostructures with few defects. These nanostructures have been created through a number of methods in either top-down or bottom-up approaches. Planar technology is a typical top-down approach where nanostructures are fabricated layer by layer with precise control.[25,26] In this approach, high resolution lithographic techniques, such as optical lithography, electron beam lithography, and x-ray lithography are used to transfer the nanoscale pattern on the substrate. Metal thin films are then deposited via vacuum coating processes, followed by either etching or lift-off to finalize the structure. Alternatively, focused ion beam (FIB) can be used to directly carve metal thin films into nanostructures[27]. The bottom-up approach relies on the molecules' self-assembly process where very fine nanostructures are built up atom by atom, molecule by molecule or cluster by cluster. This approach is less conventional than the top-down approach, but it is synthesized from fundamental building blocks based on different physical or chemical processes[28-32].

The resolution of regular optical lithography strongly depends on the numerical apertures (NAs) of the optics and the wavelength of the light source. A higher NA and lower wavelength will provide better resolution. It is well known that immersion lithography has an advantage in constructing the projection optics in an immersion fluid with numeric aperture greater than one.[33] With immersion lithography, patterns less than 90nm have been demonstrated[34]. On the other hand, in extreme ultraviolet (EUV) lithography, an extremely short wavelength of 13.4nm is applied. Patterns with feature sizes of less than 50nm are expected to be realized [35,36]. In addition, there are other

unconventional lithographic techniques which offer high spatial resolutions of features. Nanoimprint lithography (NIL) has proven to be a promising patterning technique at nanoscale [37]. In 1999, Colbrun et al. first reported step-and flash imprint lithography (SFIL)[38], which has led recent research and development forward. Two-photon 3D lithography [39], a state-of-the-art technique, is able to fabricate 3D micro/nano structures required in more complicated systems, such as photonic crystals[40] and microfluidic devices[41].

It is well known that a tiny sharp tip, ranging from 15 to 50nms, is used in scanning probe microscopes (SPM). The nature of the sharp probe suggests that SPM be employed as a potential nanopatterning and nanolithography tool. The scanning probe microscope has been widely used in many disciplines for surface science research and applications since its invention in the early 1980's[42]. In recent years, researchers have realized that atomic interaction between the scanning probe and interrogated sample surface is not only useful for nano-imaging, but can also be utilized for revolutionizing conventional bottom up nanofabrication methods. These methods include nano-manipulation, nano-deposition, and nano-patterning. The SPM based nanofabrication processes offer unique advantages of high resolution and registration accuracy, in-vivo inspection capability readily available, process automation with computer control, and low cost process under ambient conditions. Application for mass production is also possible with large scanning probe arrays[43-45]. For material deposition and patterning, a popular SPM based technique called the dip-pen nanolithography (DPN)[46-48] has been developed. With the sharp scanning probe tip, DPN can directly dispense a wide variety

of solution-based chemicals onto a substrate surface to create single or arrayed nanoscale pattern or structures[49-51]. The effectiveness of DPN relies on the material transfer from the probe tip to the substrate surface via the water condensation existing in between[52,53]. However, this requirement creates a limitation in the fabrication of metallic nanostructures due to the insolubility of metals in water and solvents.

Laser-assisted processes have been widely applied in nanomanufacturing[54]. These processes include laser-assisted micro/nano machining; laser-assisted materials synthesis and modification (deposition and removal); and laser-assisted nanopatterning. Pulsed lasers are primarily used in the processes. Compared to other nanofabrication techniques, such as electron beam lithography, laser-assisted lithography has the advantage of high precision, easy setup and high yield[55]. Pulsed lasers have been used to enhance the nanoimprint lithography process, in which the polymer film is heated by the pulsed laser, occurring simultaneously with imprinting[56]. The scanning probe microscope (SPM), combined with pulsed laser irradiation, provides a novel means to realize nanopatterning[57]. The mechanism of the SPM-pulsed laser process is rather complicated[58-60]. In the current research, a continuous wave laser is integrated into an atomic force microscope (AFM) system to achieve a more direct nanolithographic process, which opens a new avenue in the nanomanufacturing area.

1.2 Wear mechanism of materials at nanometer scale

As indicated in the previous section, lithography, as well as most nanomanufacturing, involves materials removal and/or transfer. Recent reports on wear are described here.

The removal of surface materials is a rather complicated process in nanomanufacturing. Shiari et al. developed a multiscale numerical simulation approach on single crystal aluminum to further advance the understanding of materials removal mechanisms at the nano-meter length scale [61]. Nanoabrasive wear is expected to be a dominant factor in a contact-sliding lithographic process, such as scanning probe lithography (SPL). The interactions between the sharp tip of SPM and the sample surface are responsible for nanoscale patterning in SPL. Sung et al. have investigated tip-surface interactions in the nanolithography process through both experiments and molecular dynamics simulations[62]. Nano-precision sensing in MEMS is critical, and Narayanan et al. have established a model to achieve this goal in manufacturing low-friction and low-wear parts which have nanoscale resolution of the position control[63].

Wear also plays important roles in our daily life and has many major industrial applications[64-66]. Since its invention, the atomic force microscopy (AFM) has been used for nanoscale studies [42] of materials surface morphology and tribological properties. Nanotribology has then generated great interests in the broad fields of research and application[67-72]. In polysilicon microelectromechanical systems (MEMS), contact within small areas requires highly scratch-wear resistant ultrathin films. This study was made possible by using an AFM [73,74]. Using an AFM, nanowear experiments on polymer films

were conducted successfully [75,76]. Reports have been found that a specifically-processed probe played a crucial role in contemporary AFM-based recording techniques. Among those, Bhushan et al. investigated the wear mechanism between platinum coated probes and recording medium[77]; and Chung et al. studied tribological properties of a metal-doped silicon probe on recording materials[78]. Nanoscale study of tribological properties of AFM probes remains of great interest.

Nanoabrasive wear was observed on stainless steel induced by a diamond AFM probe[79]. Such wear is simply downsizing of the conventional wear found at the macroscale. *In situ* techniques have been applied to nanoscale wear, and it was found that the abrasive wear was initiated by a series of localized onset activities [80]. On the other hand, materials can be transferred by adhesive wear[81]. Friction, in addition, can induce nanoscale crystallization [82]. To date, the roles of materials and fundamental mechanisms of wear need to be further understood, which is possible with emerging techniques and methodologies.

1.3. Stimulated nanoalloying and nanocrystallization

In most nanomanufacturing processes, nanoalloying and nanocrystallization are commonly involved when materials are in contact, i.e. where an interface is formed. Special attention has been paid in previous sections to SPM based nanolithography, in which an interface between the sharp probe and the sample surface is formed during writing. In such type of applications, two materials are involved. In the present research we focus on binary materials systems. In the current section, we firstly define

nanoalloying and nanocrystallizations, and then review the methods generating binary nanoalloys. Finally, recent work on mechanical stimulation induced nanoalloying and nanocrystallization will be reported.

1.3.1 Definitions of nanoalloying and nanocrystallization

According to the Merriam-Webster Dictionary, alloy is defined as "a substance composed of two or more metals or of a metal and a nonmetal intimately united usually by being fused together and dissolving in each other when molten" [83]. Nanoalloying literally means the process through which two elements are mixed in order to form an alloy at the atomic or nanometer scale. During the nanoalloying process, solid crystals can be generated from a uniform solution, melt or a gas phase, under the control of certain external conditions. We define this solid crystal formation as nanocrystallization.

When two different types of elements (metal or non-metal) are mixed, under external mechanical and thermal stimulations, nanoalloys can be synthesized atom by atom, molecule by molecule and cluster by cluster.[84] These nanoalloys have shown enhanced mechanical, catalytical, optical, electronic and magnetic properties[85-88]. Chen et al. discovered a structure of Ag_3Au_{10} with different optical properties from pure Au_{13} and clusters [89]. The same group has reported other gold-silver nanoalloy structures such as $Au_{44}Ag_{44}$[90], which shows high structural, thermal and electronic stability, and a core-shell structure Ag-Au alloy, which has martensitic transformations[91].

1.3.2 Methods to synthesize nanoalloys

Nanoalloys are generated through various compositions of basic elements. Nanocrystallizations will occur under certain treatment such as annealing. There are

mainly six different means to synthesize nanoalloys. Recent reports on bimetallic nanoalloys synthesized by these approaches are presented here:

- Thermolysis. Nazir et al. synthesized iron (Fe)-palladium (Pd) bimetallic nanoalloys by thermal decomposition of Fe and Pd salts at low temperature. The nanoalloys appear to be superparamagnetic in nature. [92]
- Energetic beams methods. Abdelsayed et al. have reported the laser vaporization controlled condensation method to obtain several gold (Au) nanoalloys such as gold-silver, gold platinum (Pt) and gold-palladium (Pd). During the formation, each alloyed nanoparticle corresponds to a selective laser wavelength. The bimetallic alloys synthesized by this approach were found to be superparamagnetic[93].
- Chemical reduction. Kim et al. prepared a tin (Sn)-cobalt (Co) nanoalloy ($Sn_{87}Co_{13}$) by two different chemical reduction agents. The products showed improved electrochemical properties such as good capacity retention. The average nanoalloy particle size can be easily controlled at less than 15nm[94].
- Electrochemical approach. Kim et al. also synthesized a tin-cobalt nanoalloy ($Sn_{92}Co_{8}$) through the electrochemical approach in different solutions, followed by annealing. The particle size can be controlled as small as 10nm[95].
- Radiolysis. Chen et al. generated a tin-bismuth (Bi) nanoalloy through a novel sonochemical approach. This type of nanoalloy powders showed great antiwear property[96].
- Biosynthesis. Senapati et al. obtained a gold-silver nanoalloy through a

biosynthesis approach. The advantage of biosynthesis is that the nanoparticles are entrapped within the cell matrix[97].

1.3.3 Mechanical stimulated nanoalloying and nanocrystalizations

Mechanical stimulation has been found to generate nanostructures. As early as the late 1960s, scientists were able to use electron microscopes to observe smoothed metal surfaces of packed and reorganized atoms due to mechanical polishing[98]. Fundamental study has shown that mechanical stimulation (e.g. friction) triggers chemical reactions that are different from equilibrium chemical reactions. For example, when materials are under friction, they can be oxidized and dissolved by the interaction of frictional stresses and chemical attack in water[99]. The feasibility of friction-stimulated nanostructure growth has been demonstrated on brushite with probe scanning on AFM[100]. Indium has been found nucleated, and then grew into triangular-shaped nanostructures on a silicon substrate due to friction. The interfacial junction between the nanostructures and the substrate is strongly due to the eutectic reactions. The metal-silicon interfaces are of great salience to materials scientists and engineers. The interfacial phenomena involve a non-diffusive interface of silver and silicon (Ag/Si)[101,102], and a diffusive one of gold and silicon (Au/Si), without a stable compound[103].

Mechanical forces present in wide industrial applications. During polishing, surface atoms repack and reorganize under stress leading to a smooth surface.[104] Friction force reportedly triggers chemical reactions that are different from equilibrium processes.[105] With a mechanical force, materials can be oxidized and dissolved in

water[106-109] and form a boundary layer in oil as lubricants.[99,110,111] In addition, mechanical stress introduces deformation, fracture, and wear, resulting in changes in a large number of nucleus positions and therefore the physical motion of an atom.[112] Being able to control surface forces precisely allows the mentioned damages to be significantly reduced or eliminated.

It has been established that silicon alloyed with gold forms a eutectic alloy which can be used as a low melting point solder for silicon devices.[113,114] During soldering, it is desirable for silicon to have a high diffusion rate inside the gold.[103,115] According to the equilibrium phase diagram (shown in the supporting materials), the gold (Au) and silicon (Si) system forms a eutectic with a small quantity of about 5%wt Si at 363 ^{0}C, existing as a perfectly mixed liquid over a fairly broad temperature and composition range.[116] Equilibrium eutectic systems have been used to fabricate nanorods and nanowires at a relatively low-temperature through vapor-liquid-solid synthesis method.[3,5,117-120] Among those, metastable phases of AuSi and Au_7Si appeared with different structural and electronic properties.

To summarize, we have reviewed the existing nanomanufacturing processes by which various nanostructures can be fabricated. Scanning probe based nanolithography is a promising approach to generate ultra small features, due to the nature of the sharp probe. When the probe and the surface come into contact, abrasive wear between them is responsible for the materials removal during writing. With the aid of external mechanical and thermal stimulation, nanoalloying and nanocrystallization processes are present.

1.4 Motivation and objectives

1.4.1 Motivation

Common nanofabrication techniques fall into two categories: top-down and bottom-up approaches. There are two major issues in top-down approaches. One is the imperfection of deposited nanostructures, and the other is that this approach requires costly tools and processes. The major disadvantages of current bottom-up nanofabrication methods are that they generally suffer from low efficiency and throughput. Therefore, this approach is not suitable for mass production. In summary, there are tremendous challenges remaining in the field in creating metallic nanostructures by using conventional top-down or bottom-up techniques. It is even harder to fabricate arrayed metallic nanostructures with controlled size, shape, location and at low cost. A new approach named laser-assisted scanning probe alloying nanolithography (LASPAN) is being developed to address this issue. This method offers real nanoscale resolution fabrication of metallic structures in the ambient. It combines the advantages of both conventional top-down and bottom-up processes: the pattern location and size can be controlled by the AFM instrument and sharpness of the AFM probe, respectively; the nanostructures will grow in a bottom-up manner, i.e. atom by atom, molecule by molecule or cluster by cluster, which could offer crystallized metallic nanostructures. The laser plays an important role for realizing the highly localized heating and precise position control on the tiny AFM cantilever, as well as the possible measurement of the local heating temperature using the interferometry technique. By adjusting the power of laser output, we can obtain a range of different temperatures,

which makes a variety of metal candidates possible. An ideal one-dimensional crystallized metallic nanostructure could be fabricated through LASPAN in a highly controlled manner.

On the other hand, this new approach will further advance our fundamental understanding of the aspects of nanoalloying and nanocrystallization in a gold-silicon system.

1.4.2. Objectives

In this research, we plan to achieve three objectives.

(a) Interfacial phenomena and physical principles

Scientifically understanding the interfacial phenomena and fundamental physical principles of LASPAN is crucial for optimizing the fabrication process. To achieve this objective, I will investigate the feasibility of an alternative theoretical framework of the mechanism that can interpret the experimental results.

(b) Develop LASPAN technology

Understanding the nanoscale material transfer process in LASPAN is critical, in order to extend the maximum capability of this new technology. Another key component is the integration of a laser system to provide sufficient thermal energy. In this objective, we will develop a full scale investigation on the influence on LASPAN of different writing conditions and parameters such as materials, surface condition, sharpness of the probe, and mechanical loading. I will also develop a controllable way to introduce the

laser beam to focus on the AFM probe cantilever, thus achieving the seamless combination of both laser and SPM systems, and enabling the fabrication of nanostructures.

(c) Characterization of nanostructures generated using the LA-SPAN

A series of characterizations of nanostructures generated by LASPAN is needed so as to investigate their structural, physical and chemical properties. In this objective, we will conduct microscopy (e.g. SEM, TEM and AFM) characterizations and other surface characterization techniques (e.g. RBS analysis).

1.5 Structure of the dissertation

This dissertation includes seven chapters. After introduction of the nanofabrication process in Chapter I, a detailed description of the LASPAN instrument development is offered in Chapter II. Then the process development and optimizations of this technique are investigated in Chapter III. Following the new LASPAN process development, discussions about energy analysis and dissipation are provided in Chapter IV. In Chapter V, the nanocrystallization associated with the LASPAN process is demonstrated. Finally, conclusions are drawn in Chapter VI, together with a description of the impacts and future recommendations.

CHAPTER II

LASPAN SYSTEM DEVELOPMENT

Liang et al. have discovered stress-induced nanostructures[82,121-123] through friction. In the present work, an atomic force microscope (AFM) will be developed into a nano-writing system. Assisted by a laser system, it is expected that small features be written through the AFM probe. The proposed process is as following. A sharp AFM probe raster scans over a sample surface. The probe is in contact with the substrate during scanning, which is defined as writing. Room temperature writing was firstly carried out to generate nanostructures through stress and friction. Furthermore, nanostructures were formed more easily if external thermal energy was introduced. On the other hand, the AFM probe is so sharp that the contacted area between probe and substrate is highly localized (within a couple hundred nanometers). A laser system is immediately brought into attention since it offers both highly focused laser beam and precision control, which enhances the overall process.

The atomic force microscope (Nano-R2, Figure 1(a)) manufactured by Pacific Nanotechnology Inc. (PNI) is employed to perform writing. The challenge here is to design and integrate a brand new external system into an existing microscope, and utilize the advantages of both components for nanoscale writing process. In this work, the functionality of this AFM as a processing tool will be discussed, more importantly; the development of LASPAN hardware system is demonstrated in detail. In this chapter, we will first introduce the room temperature writing setup; then the heating stage

implement; finally the integration of an external laser optical system to complete the LASPAN hardware setup.

Figure 1 Atomic force microscope. (a) Pacific Nanotechnology Inc. Nano-R2 AFM (b) A closer view of the objective, scanner, motorized tripod stage and sample holder with moving stage (Courtesy of PNI)

2.1 Room temperature writing by a stand-alone AFM

This technique utilizes an atomic force microscope (AFM) as a writing tool, an AFM probe coated by a thin metal layer as a "nano-pen", to perform raster sliding on a single crystal silicon substrate. The process performed here is a directly nanoscale writing. The precisely control of AFM scanning is the critical part of the SPAN.

2.1.1 AFM functionality as a processing tool

The main components of this microscope are: a 10X Mitutoyo objective, a scanner, a tripod stage and a sample holder (Figure 1(b)). Each of them plays an important role in the writing process development.

The 10X objective plus a CCD camera are capable of producing a resolution as small as 1 micron and display the digitized image on a television screen.

The scanner is the most critical part of the microscope. In Nano-R2's design, the AFM probe physically scans over a fixed sample. The built-in X and Y piezoelectric sensors control tip movement in the horizontal plane. The maximum displacement along one direction is 85μm.

The motorized tripod stage contains a separate Z-piezoelectric sensor, which offers fast and precise manipulation of the scanner's vertical movement. The maximum vertical displacement is 22mm, and the smallest step of vertical movement is 160nm. The sample holder is made of five cylindrical metal pieces. Each piece can be easily inserted or pulled out, to achieve the appropriate height for different specimens. There is an automated X-Y translation stage beneath the sample holder that moves the sample holder below the AFM probe at certain steps (from 1μm to 25000μm).

With the design of Nano-R2, one can quickly locate the point of interest (POI) on the sample and perform a robust scan.

2.1.2 Basic AFM set-up for the writing experiment

The basic set up can be found in Figure 2. We started the writing experiment with a stand-alone AFM at room temperature. This is a process called scanning probe alloying nanolithography (SPAN). The recipe is given in Appendix A.

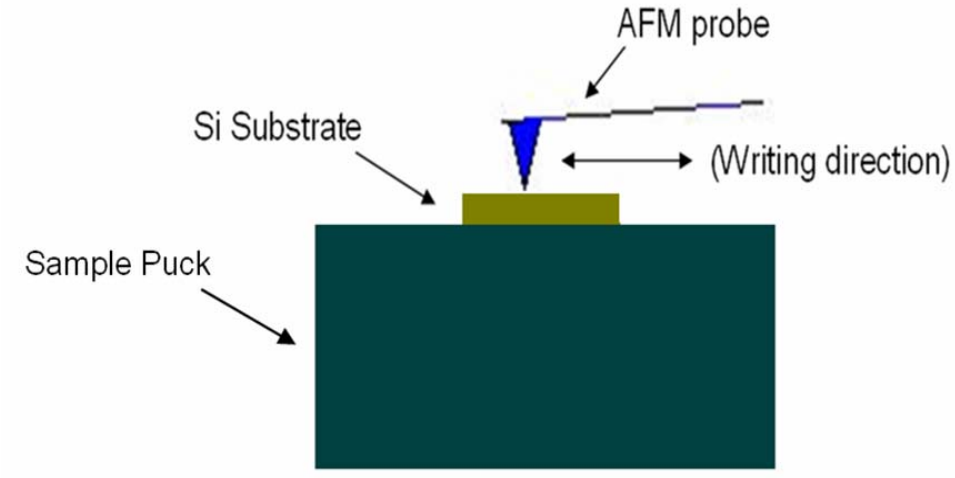

Figure 2 AFM set-up for room temperature writing

2.2 Heating stage implement

In the SPAN process, it was proposed that the induced stress during writing would be a governing factor to form nanostructures. After repeating many room temperature writings, we found that the localized thermal energy input, which is the heat generated by friction, also played an important role in the alloying process. Hence a new sample stage with a built-in electric heater was designed and manufactured. The sample mounted on the stage can be heated up to three hundred degrees (Celsius). The diagram of the system with this heating stage is shown in Figure 3.

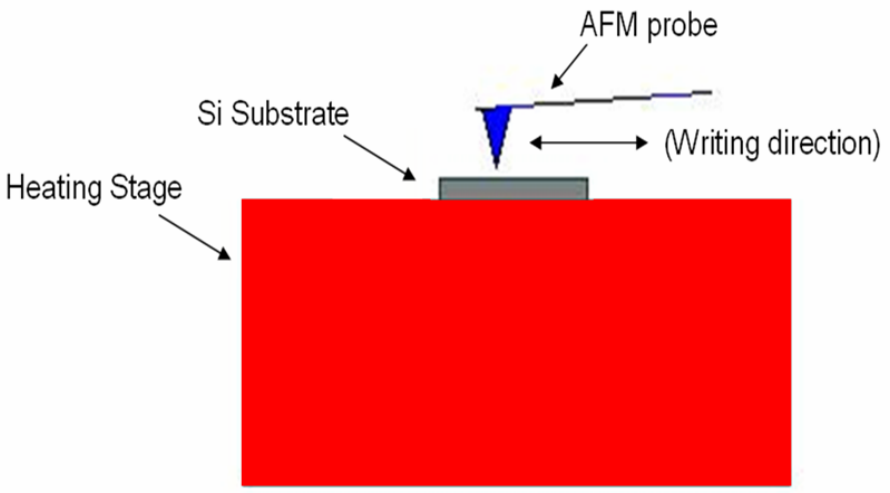

Figure 3 AFM set-up for SPAN with implement of heating stage

2.3 Introduction of a laser optical system

2.3.1 Origination of laser system integration

The heating stage provides a good deal of thermal energy to the substrate during writing. The sample is heated through thermal conduction. However, the piezoelectric sensor in the AFM scanner is integrated behind the tip mount and is highly sensitive to external thermal interference. The critical temperature is approximately 150^{o}C (according to the manufacturer). When the tip comes in contact with the substrate, the scanner is less than one millimeter away from the heat source. Therefore, it cannot function correctly once the substrate is above the critical temperature.

The alloying process during writing requires sufficient thermal energy input in all different binary materials systems. The current setup can only provide a low temperature

environment without damaging the AFM system. An external laser system was introduced to address this issue.

2.3.2 Advantages of a laser optical system

An Nd: YAG solid state laser (532nm) was selected to be integrated into the AFM setup, referred to as the laser-assisted scanning probe alloying nanolithography (LASPAN) system (Figure 4). The laser beam was directly projected onto the backside of the AFM cantilever to provide thermal energy. There are two main advantages of the laser optical system: First, the laser provides highly controllable power output. The maximum output power of the laser in free space is 65mW. By inserting a double spin attenuator (one spinner's selection ranges from 0.0001 to 0.1; the other one ranges from 0.14 to 0.63), we can easily decrease the laser power output to different desired levels. Second, the heating spot is highly localizable. The diameter of the output laser beam can be focused to about 10μm by the objective. This highly focused laser spot can provide highly localized heating without interfering in the piezoelectric sensor in AFM.

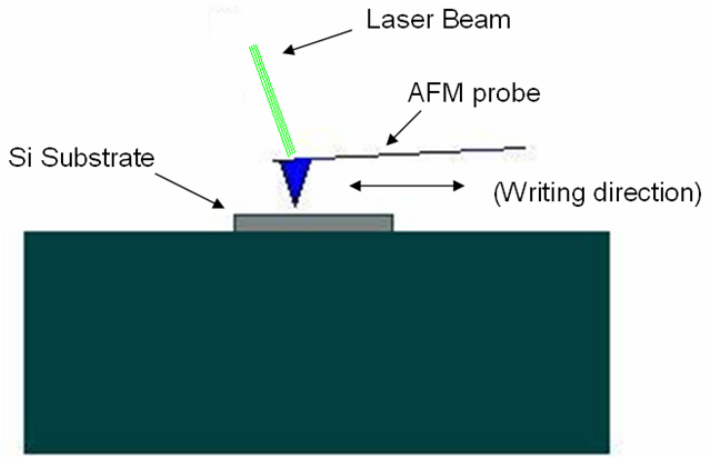

Figure 4 AFM set-up with implement of laser system

2.3.3 Development and optimization of laser optical system set-up

Initially, an optical fiber was used to direct the laser beam out, due to the convenience of it being commercially available (see Figure 5). However, it was found that the laser beam was rather difficult to align through the fiber. In addition, the intensity of the laser beam was significantly decreased by about 70%. These two drawbacks prevented keeping the optical fiber.

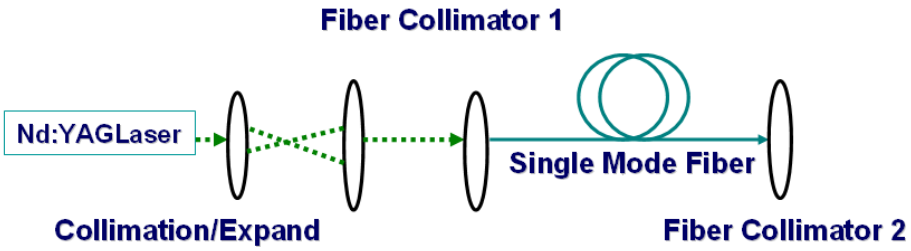

Figure 5 Diagram of laser optical system with fiber

To address these issues, the free space setup is then developed (see Figure 6).

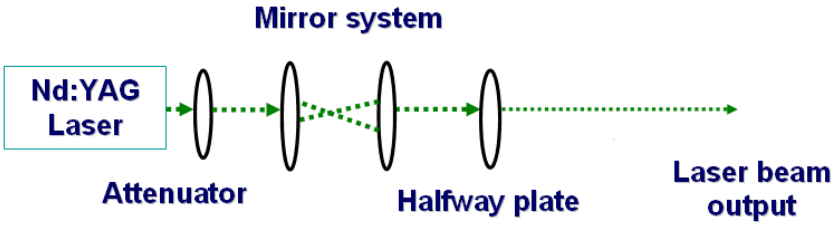

Figure 6 Diagram of laser optical system setup in free space

The double spinner attenuator is set right next to the laser beam emitter to coarsely adjust the laser power output. Four mirrors were used to align the laser beam's height in the free space. A halfway plate (i.e. a polarizer) is inserted after the mirror

system to finely adjust the laser power output. All the parts are mounted on one big breadboard laser desktop by magnetic bases. A number of stainless steel cylindrical block are used to increase the vertical displacement of the whole laser optical system, in order to align the laser beam into the AFM system. An external illuminator provides sufficient sample illumination. The actual laboratory setup is shown in Figure 7.

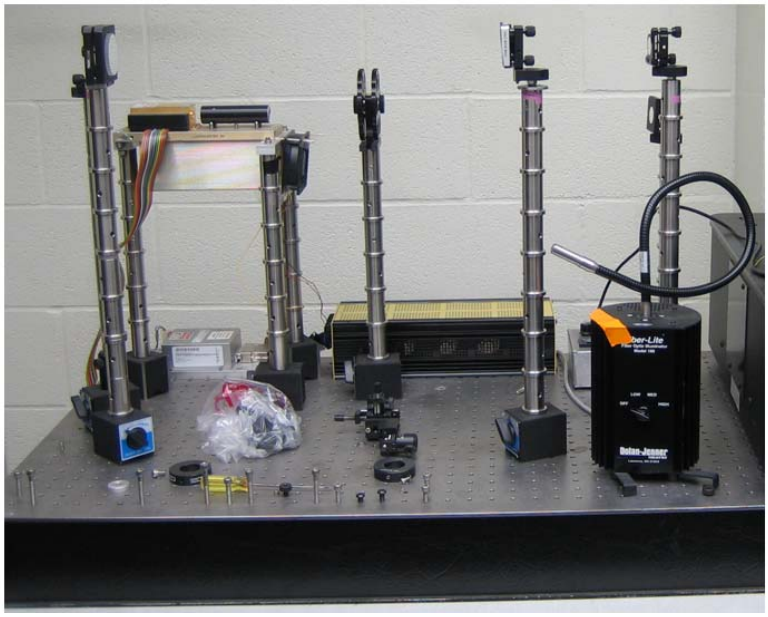

Figure 7 The real laboratory setup of laser optical system

We can use the laser optical system described above to control the output laser power, as precisely as 0.1μW. The power ranges from 30mW to 0.1μW. All the mirrors have two separate knobs; each of them controls laser spot movement along one direction (either horizontal or vertical). Therefore, we can easily adjust the position of the output laser spot.

Overall, this optimized optical system has the ability to manipulate the laser power output and laser spot position in a highly controllable fashion.

2.4 Materials selection

2.4.1 Selection of AFM probes

There are two major commercially available AFM probes: silicon (Si) probes and silicon nitride (Si_3N_4) probes. In the LASPAN process, a thin layer of metal film is deposited on the AFM probes. The coated probe then scratches on the substrate under stress and in-situ laser thermal energy integration. We required that the probe have a certain level of bending capability and good thermal conductivity. After comparison experiments, we decided to use Si_3N_4 probes (Veeco, NP-NC-20). The tip and cantilever specifications of this type of Si_3N_4 probe can be found in Figure 8 and Figure 9, respectively.

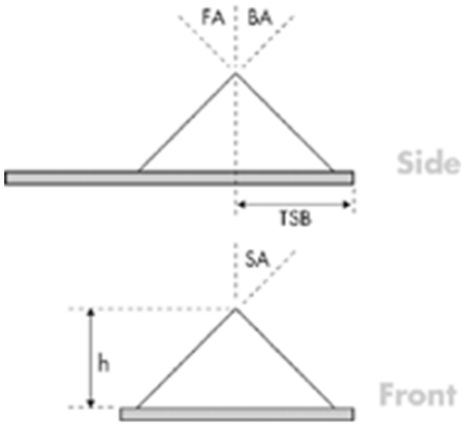

Geometry: Cast
Tip Height: 2.5 μm – 3.5 μm
Front Angle (FA): 35°
Back Angle (BA): 35°
Side Angle (SA): 35°
Tip Radius (Nom.): 20nm
Tip Radius (max.): 60nm
Tip Set Back (Nom.): 4 μm
Tip Set Back (Rng.): 3 μm -- 5.5 μm

Figure 8 Si_3N_4 NP-UC tip specifications.

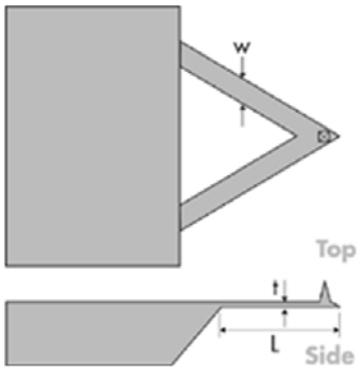

Shape	Length (μ m)	Width (μ m)	Freq. (kHz.)	K (N/m)
A Triangular	115	25	57	0.58
B Triangular	196	41	20	0.12
C Triangular	115	17	56	0.32
D Triangular	196	23	18	0.06

The thickness of the cantilever is 0.6 μ m

There are four "V" shape cantilevers and tips mounted on each probe

Figure 9 Si_3N_4 NP-UC cantilever specifications.

Each Si probe has only one rectangular cantilever, while each Si_3N_4 probe has four different sizes of "V" shape cantilevers, which offer wider selection for one writing without changing probes. In addition, the spring constant k of the Si probe is 0.1N/m, but the Si_3N_4 probe has the k value ranging from 0.06 to 0.58N/m. From Hook's law

$$F = k\Delta Z \tag{2.1}$$

where ΔZ is the deflection (bending) of the cantilever when the tip is in contact with the substrate. With the same bending ΔZ, the Si_3N_4 probe can hold greater load.

Each AFM has its own laser beam output, acting as a force sensor. This internal laser is only used to monitor the movement of the AFM tip. Thus the power of this laser beam is very low. In general, there is a thin metallic coating (e.g. 50nm aluminum) on the back of cantilevers to improve reflectivity of the laser force sensor. However, this metallic coating prevents thermal energy absorption from the external laser. Hence, we do not want such probes with high reflectivity (usually >96%). The Si_3N_4 probe (Veeco,

NP-UC) is the only type of commercially available AFM probe which does not have a coating on the backside of the cantilever (where UC stands for uncoated). A calculation about the absorption of laser energy is shown below:

For Silicon Nitride with 532nm continuous wave

$$n_{SiN} = 2.08 \tag{2.2}$$

$$R = \left(\frac{n_{SiN} - n_0}{n_{SiN} + n_0} \right)^2 = \left(\frac{2.08 - 1}{2.08 + 1} \right)^2 = 12.3\% \tag{2.3}$$

$$T = \frac{4 n_{SiN} n_i}{\left(n_{SiN} + n_i \right)^2} = \frac{4 \times 2.08}{\left(2.08 + 1 \right)^2} = 87.7\% \tag{2.4}$$

$$\alpha_{SiN} = 1.04 \tag{2.5}$$

For 0.6um thickness, total absorption is,

$$1 - \exp\left(-\alpha * t \right) = 46\% \tag{2.6}$$

Total absorption is estimated as,

$$87.7\% \times 46\% = 40\% \tag{2.7}$$

Assume the maximum laser power output is 30mW, and the diameter of the focused laser beam is 10μm; the intensity can be calculated as, 3.9e8W/m^2.

In a word, The NP-UC type of Si_3N_4 probe meets all requirements of the LASPAN process.

2.4.2 Selection of substrate and coating materials

A single crystal silicon (100) wafer is used as substrate, since Si is the most popular material base of modern semiconductor devices. A 150nm layer of gold (Au) coating is applied to the Si_3N_4 probe's surface, with 3nm chromium (Cr) adhesion layer

in between. Gold-silicon is a simple eutectic system; the eutectic temperature in this system is 363°C. The Au-Si binary phase diagram can be found in Figure 10.

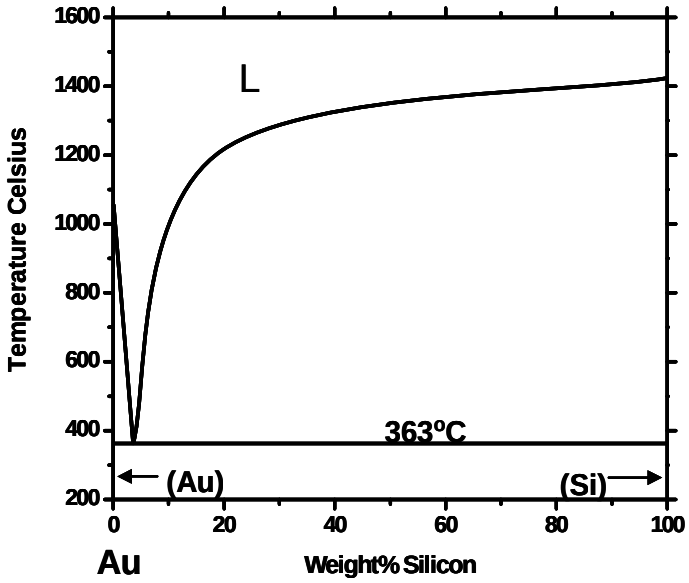

Figure 10 Gold-silicon equilibrium binary phase diagrams with weight%. Au-Si system, eutectic temp 363°C. Source: SGTE phase diagram collection

In the LASPAN process, the gold coating on the sharp AFM tip is brought into contact with the silicon surface. The incoming laser easily raises the temperature of the Au/Si interface to several hundred degree Celsius or more (calibration of temperature will be discussed in the next chapter). Hence in the Au-Si system, the eutectic temperature can be easily reached to realize the alloying process locally.

2.5 Integration of laser optical system and AFM

The Nano-R2 AFM has its own optical system (see Figure 11). This system is mainly used to observe the sample and find the point of interest (POI). The illuminator

can be taken out of the whole setup, leaving a hollow channel. This open channel is a perfect interface to connect both laser optical system and the AFM. The aligned laser beam enters the microscope through the channel, and is then split by a beam splitter (BS) into two beams. One beam goes through the objective and is eventually focused on the cantilever; the other beam is reflected back and filtered out to prevent the CCD camera screen from burning. The complete diagram and actual laboratory setup can be found in Figure 12 and Figure 13, respectively.

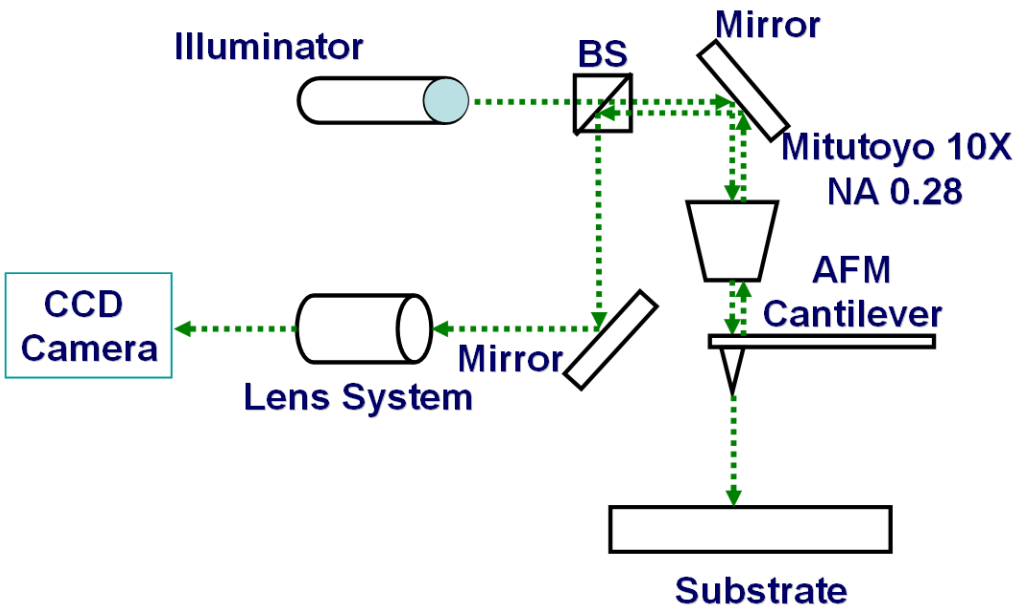

Figure 11 Optical system of Nano-R2 AFM

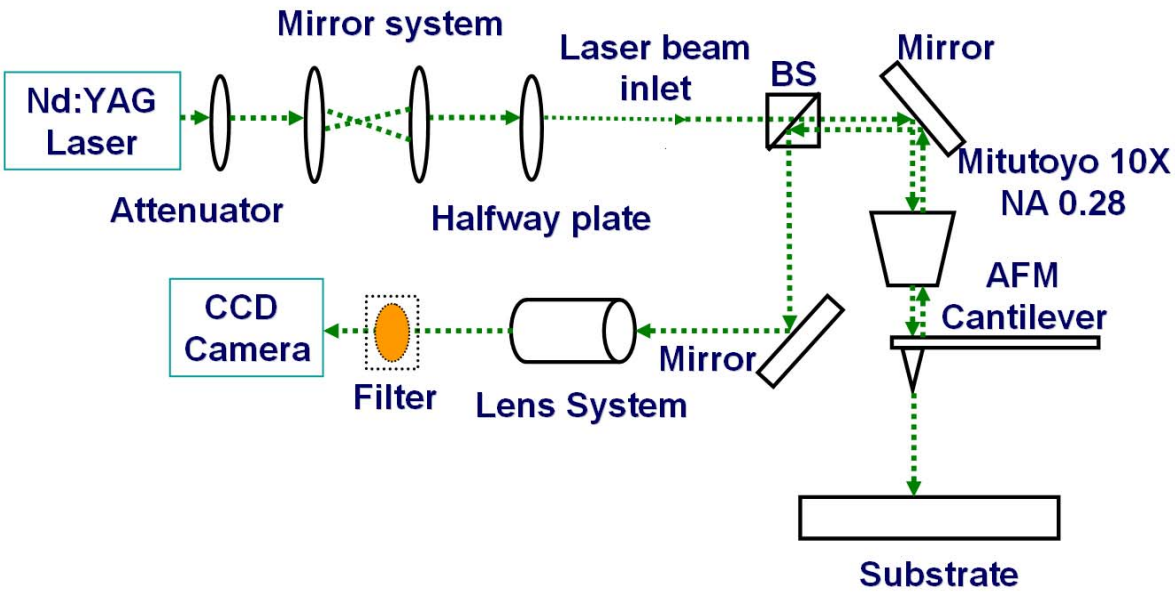

Figure 12 Diagram of integrated laser optical system and Nano-R2 AFM

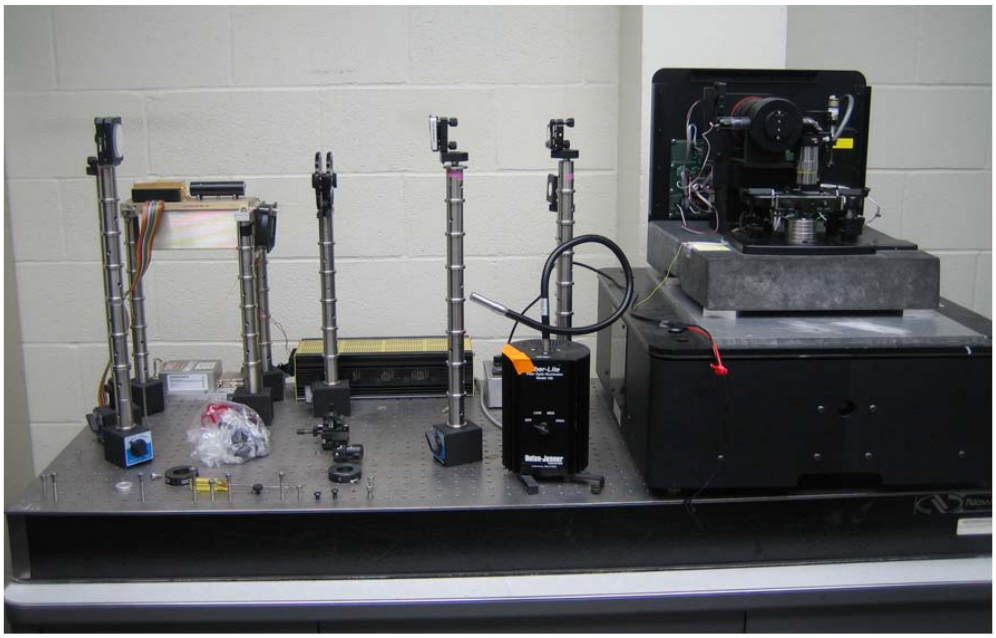

Figure 13 Real laboratory integration of the laser optical system and the Nano-R2 AFM system

In this chapter, the seamless integration of both laser optical system and the commercial Nano-R2 atomic force microscope has been demonstrated. This fully developed LASPAN system has the ability to control all key parameters of the laser-assisted writing in a gold-silicon system. The development of the LASPAN process will be described in the next chapter.

CHAPTER III

LASPAN PROCESS DEVELOPMENT AND OPTIMIZATION

AFM has been employed to realize the nanolithography process through different means such as simple scratch, localized anodic oxidation, and chemical deposition (e.g. Dip-Pen Nanolithography). We developed a novel process to integrate a laser system into the existing Nano-R2 AFM system. This newly built laser-assisted atomic force microscope was then used to perform the laser-assisted scanning probe alloying nanolithography (LASPAN) process.

LASPAN is a novel approach for fabricating nanostructures. The integration of an external laser optical system into a commercial atomic force microscope expands the AFM's functionality as a processing tool. With the LASPAN technique, fine nanostructures can be fabricated under highly controllable procedures. In principle, the process is applicable to a variety of material systems. Hence, this technique opens a new avenue in nanomanufacturing. In this research, the general process of LASPAN is fully developed. Additionally, the application of LASPAN in an Au-Si material system to fabricate nanostructures is optimized. In this chapter, we demonstrate the experimental procedure in detail.

3.1 Principles of LASPAN process

As the name indicates, the LASPAN technique has two major components, i.e. laser-assisted process and scanning probe microscope (SPM) based writing. The fundamental principles of LASPAN are to generate a highly localized interface (at

nanometer length scale) between two pre-selected material candidates, control the alloying process by triggering external thermal energy input, and fabricate nanostructures in the defined region. A diagram of the basic LASPAN process is shown in Figure 14.

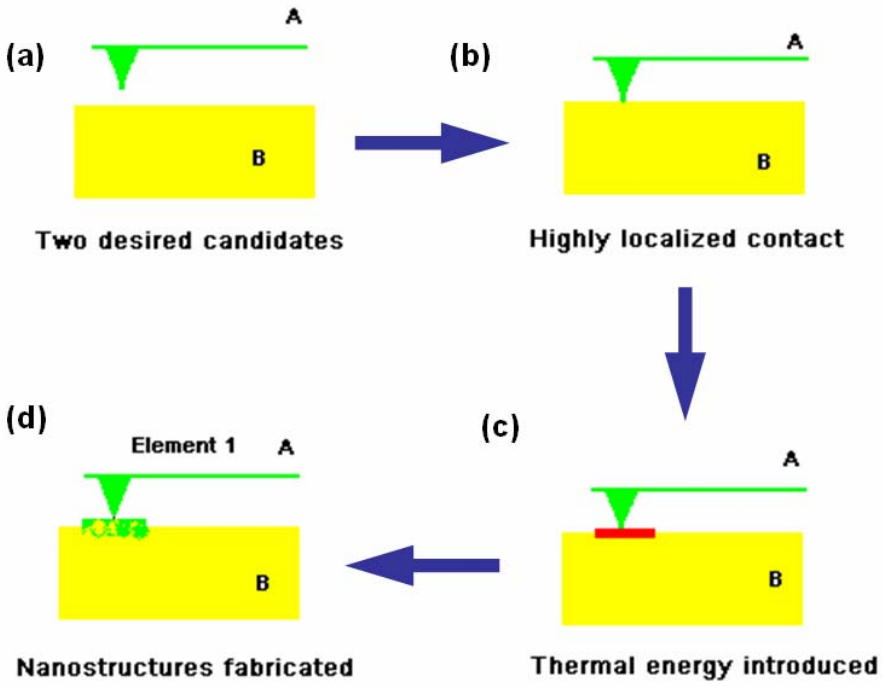

Figure 14 Fundamental diagram of LASPAN process

The LASPAN technique developed here is based on an atomic force microscope (AFM), which has been actively used in many areas of nanotechnology since its invention. An AFM can be used not only as a morphology characterization instrument, but also as a processing tool. One standard function of our AFM (PNI, Nano-R2) is the control of tip scanning. With the aid of software control, the tip can be moved to

anywhere on the sample surface, and perform a raster scan. The radius of the curvature of a sharp AFM tip generally ranges from 15nm to 50nm. The tip is naturally utilized to provide a highly localized interface, when it is brought into contact with the substrate. Once the tip is in place, the laser spot is introduced on the back side of the probe. The thermal energy is absorbed by the cantilever and tip, which results in a local temperature increase in the interface. Overall, to develop the LASPAN process, there are three major challenges: (a) Cross linking between AFM and laser system; (b) Mechanical stress load; (c) Thermal energy input. To overcome such challenges, a systematic approach with high precision is required. The details of the LASPAN process will be discussed in the following sections. The recipe of LASPAN is given in Appendix B.

3.2 Sample preparation

3.2.1 AFM probes preparation

In the LASPAN technique, an AFM probe is employed as a "pen" to write on the substrate. Commercially available (NP-UC-, from Veeco Inc.) contact mode probes are used in our experiments. The as-received probes are made of silicon nitride (Si_3N_4). There are four different types of cantilevers and tips on a rectangular block; two on each side (see Figure 15(a)). The AFM scanner has an "L"-shaped magnetic tip holder. We mount each probe onto a thin, rectangular steel piece using silver paint, before it can fit our Nano-R2 AFM. The probe with a metal piece is seen in Figure 15(b). The metal piece can be reused after cleaning the contaminants.

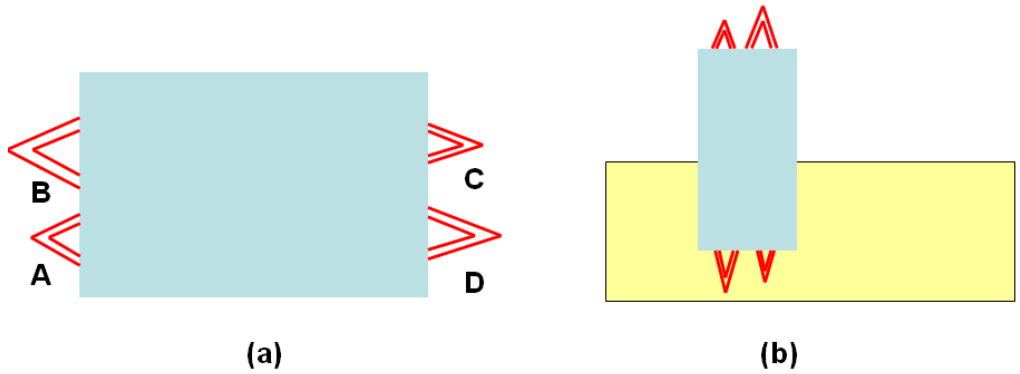

Figure 15 AFM probes. (a) Sketch of a silicon nitride probe as received, four tips with different dimensions; (b) Mounted probe on a metal piece. (The sketch is not to scale)

The prospective materials candidate on the probes is gold (Au), as discussed in the previous chapter. The Au film (150nm) is deposited in a vacuum chamber through thermal evaporation. To improve the adhesion between Au and Si_3N_4, a thin chromium (Cr) adhesion layer (3nm) is applied. The deposition starts while the chamber pressure is less than $5x10^{-6}$torr. A quartz crystal microbalance (QCM) monitors the change in frequency of a quartz crystal resonator, in order to calculate the thickness of the deposited film. The coating rate is generally 2 angstrom per second. The probes are stored in a clean box before writing.

3.2.2 Substrate preparation

The substrate used in the LASPAN process is a single crystal silicon Si (100) wafer, which is cut by a dicing saw into small pieces. Each cut sample is a 1cm x 1cm square, with its thickness being 750μm. The sample is then thoroughly cleaned by water, acetone, and isopropaonal, in that order, and dried on a hot plate.

The desired structure is at the nanometer scale, but the area of the whole substrate is huge compared to the area of the point of interest. The resolution of the AFM optical system is about 1μm; in practicality, we cannot observe any structure smaller than 1μm. Therefore, it is extremely difficult to find the nanostructure for characterization after writing. To address this issue, we fabricate some easy-to-find feature indicating the positions of nanostructures generated by LASPAN. A well designed pattern (see Figure 16) including letters, numbers and dashed lines was fabricated with e-beam lithography (Joel T330, CNST@TAMU). The side length of the square is 50μm, hence the pattern can be easily found under an AFM optical microscope. All the writings are performed within the square. The letters, numbers and dashed lines help to locate the position of the writing trace.

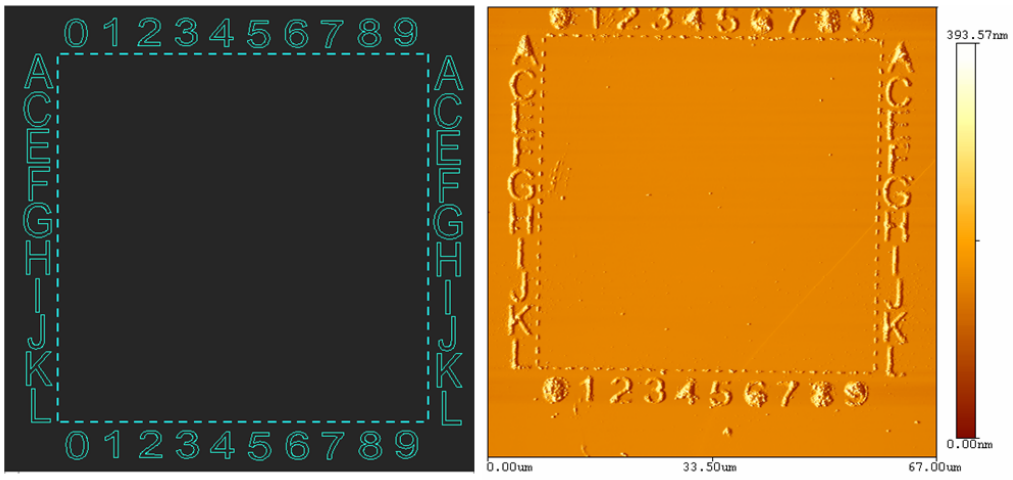

Figure 16 Micro patterned mark. (a) Designed mark pattern for e-beam lithography; (b) AFM topography of fabricated mark. The square size is 50μm

After e-beam lithography patterning, the sample is evaporated into a 50nm thick silver or aluminum film, followed by a lift-off process. The substrate with a number of square marks is ready for LASPAN.

3.3 Development and optimization of LASPAN process

3.3.1 Experimental procedure development and optimization

The LASPAN experimental procedure has four major parts: (a) AFM optimization; (b) Stress loading – bending of cantilever; (c) External laser integration optimization; (d) Writing. Each part will be described in detail as follows.

(a) AFM optimization

Our Nano-R2 AFM must be optimized before writing is started. The substrate and pre-coated probe are first mounted on the sample puck and tip holder. The scanner linearization is then performed automatically by the AFM controller, once a command is sent to the AFM computer. The configuration is loaded as "contact mode."

The tip we use in LASPAN is different from those used in normal contact mode imaging. As described in the previous chapter, we purposely chose the silicon nitride (Si_3N_4) cantilever without a back side metal coating layer that would prevent a heavy loss of incoming laser intensity. Hence the reflectivity of this type of cantilever is fairly low (refer to equation (2.3); estimated value approximately 15% or less). On the other hand, the power of the AFM's internal laser is very weak (around 1mW). In most cases, the reflected signal of the pure Si_3N_4 cantilever is too weak for the detector, thus the detector is unable to sense the signal and give correct feedback. Therefore, we must

manually adjust the tip position, which is one drawback of using a pure Si_3N_4 cantilever. During the whole LASPAN process, the internal laser beam remains off.

The optical system of the AFM observes in-situ the movement of the probe. We first use the objective lens to focus on the tip, record the z-position, then focus on the substrate, and record the z-position again. The software automatically calculates the distance between the measurements, and drives the scanner to guide the tip's coarse approach to the sample surface. After the coarse approach is completed, both the AFM tip and sample surface are in the depth of field of the objective. The XY piezoelectric stage then moves the substrate in the xy plane until the designated position (usually the square with a mark) appears on the screen and the tip falls into the marked area.
The last step in AFM optimization is to initialize the line scan. The scanning parameters, such as length (μm), frequency (Hz), and scanning angle, should be entered before scanning. Once the parameters are set, we run the line scan a few times. The computer will automatically find the initial point for the line scan, according to the value entered. Generally, there is horizontal displacement (up to 50μm) between the physical tip position after the coarse approach and the initial line scan position. The trial scans are important because they eliminate this displacement. The tip should be stopped at the left end point of the line scan, since this position will offer more room for laser spot focus in part (c).

(b) Stress loading – bending of cantilever

After AFM optimization, we want to bring the tip into contact with the surface and apply the load to certain level. Since the feedback system is not engaged, we manually move the scanner downward.

After the coarse approach, the distance between the tip and substrate is approximately 50-70μm. Each step of the main control of the scanner's vertical displacement is 5μm. The tip movement is monitored in-situ by the AFM optical system at all times. The tip moves down until a clear bending appears (see Figure 17), indicating that the tip is in close contact with the sample surface. The fine adjustment of the scanner can be realized by manually moving the tip down (this function is found in the scanning menu). The smallest step is 160nm. Alternatively, retracting the tip and pushing it down finalizes the "zero-load" tip position. Finding one particular empirical standard involves retracting (or lowering) the tip until the tip slippery occurs, then moving the tip back one step in the opposite direction. Once the tip is at "zero-load" position, the load is ready to be applied.

Starting from the "zero-load" position, the tip is lowered down until the desired load is reached. The load f_L is estimated through equation (3.1) as

$$f_L = k \cdot \Delta z \tag{3.1}$$

where k is the spring constant of the cantilever, Δz is the deflection of the cantilever, which is equal to the displacement of the tip from the "zero-load" position. The values for the spring constants of different cantilevers were given by the company (from 0.6 to

0.58 N/m), and Δz ranges from 1μm to 15μm; thus the load applied ranges from 0.6μN to 8.7μN.

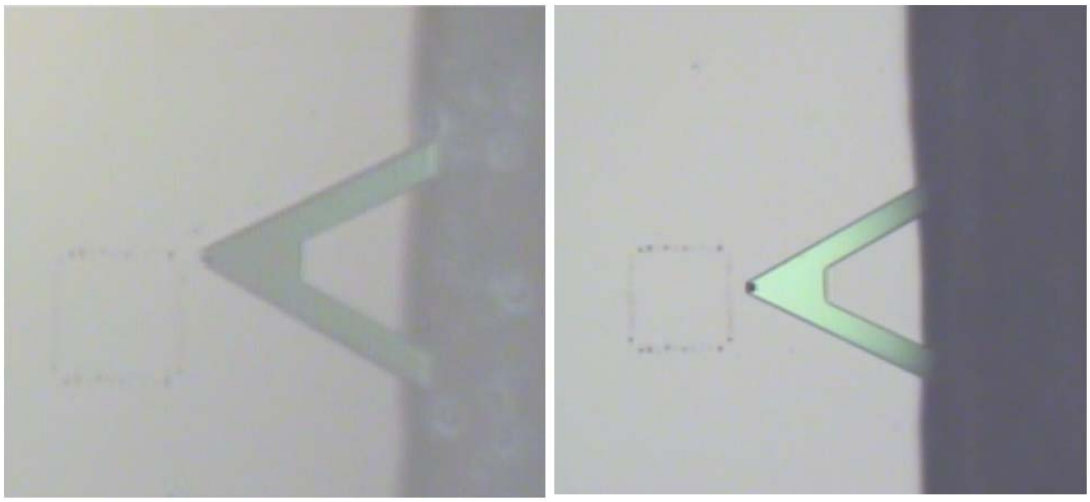

Figure 17 Reflection change on the probe shows tip-surface engagement and clear bending. Left: before tip is in contact with surface; Right: after load is applied

(c) External laser integration optimization

The third part of the LASPAN process is to optimize the external laser integration. After the stress is applied to the AFM probe, the scanner, the tip and the sample will be fixed; only the optical components are manipulated. We need to systematically align the laser beam and make sure the focused laser spot projects to the right spot on the back side of the cantilever. The complete diagram of operations in this part is shown in Figure 18.

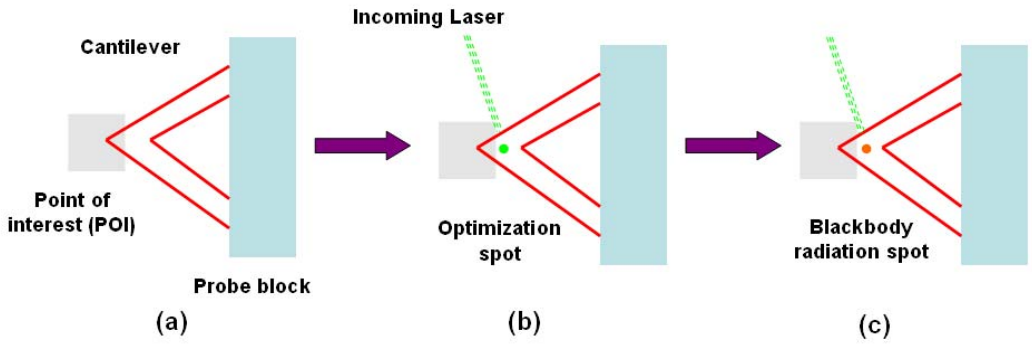

Figure 18 Diagram of laser optimization. (a) Locate point of interest (POI); (b) Laser spot optimization with attenuation and without filter, green spot is present on the backside of cantilever; (c) Blackbody radiation spot optimization with filtering out green laser, shinny flash spot is present indicating localized heating.

The laser beam is introduced into the AFM optical system through the open inlet path (shown in Figure 19), where the AFM illuminator was pulled out. The double spinner attenuator is set at maximum attenuation (about 1/1000000). Thus, the output laser beam is too weak to burn the CCD camera. A green spot appears on the screen, indicating the laser beam's current position. The objective integrated into the AFM can be moved in a horizontal plane by two attached screws. While the objective moves, the green spot stays at the same position. The screen displays the tip moving back and force to approach the green spot. The mirrors are sometimes employed to finely adjust the absolute position of the green laser spot to align it along the cantilever's axis. The manipulations of objective and mirrors are utilized to land the spot on the cantilever.

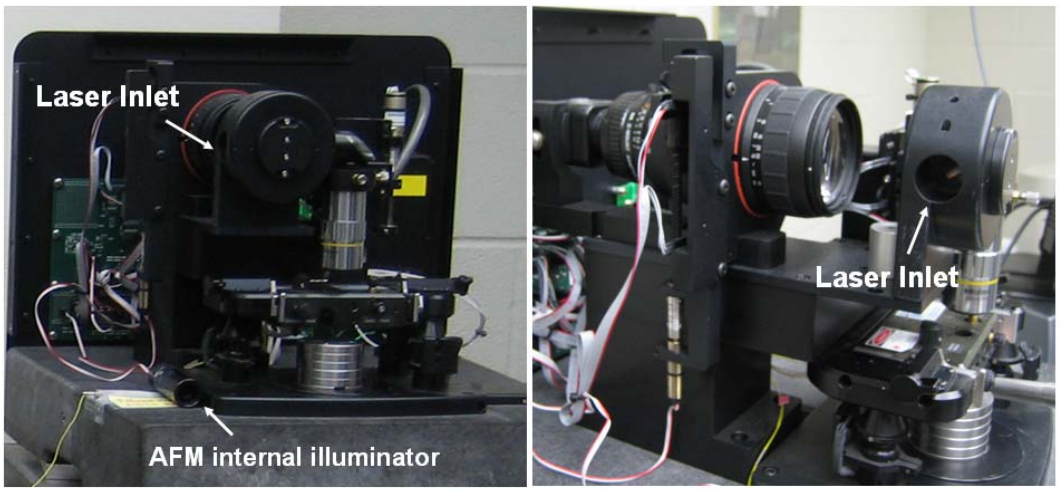

Figure 19 Connection between laser and AFM. Left: front view of laser inlet; Right: side view of laser inlet

A filter is inserted in front of the CCD camera after the green spot is located (refer to the diagram in Figure 12). This filter allows only laser beams with a greater wavelength than 600nm to pass. Hence the green laser beams resulting from the Nd: YAG laser will not damage the CCD camera when the laser power is tuned up.

At this stage, the external laser is engaged to provide thermal energy input. The objective focuses the diameter of the laser beam down to 10μm, and the maximum output power when reaching the cantilever is 30mW. The power intensity can be expressed as:

$$I = \frac{P}{\pi \cdot (D/2)^2} \tag{3.2}$$

where I is the power intensity, P is the output power of laser beam, D is the diameter of the focused laser beam. Plugging the numbers above into (3.2), we can calculate the

value of I as $3.9\text{x}10^{8}\text{W/m}^2$. This intensity is enough to provide localized heating up to several hundred degrees.

In general physics, a matter at any temperature other than absolute zero has blackbody radiation. The Planck's distribution gives the description of energy intensity in terms of the wavelength of emitted light and temperature of the object

$$I(\lambda,T)=\frac{2hc^2}{\lambda^5}\frac{1}{e^{hc/\lambda kT}-1} \tag{3.3}$$

where I is the energy density, T is the temperature of the blackbody, h is Planck's constant, c is the speed of light, and k is Boltzmann's constant. Equation (3.3) indicates that at each temperature of the blackbody, there is one wavelength corresponding to the highest energy intensity, and vice versa. The theoretical plot is found in Figure 20.

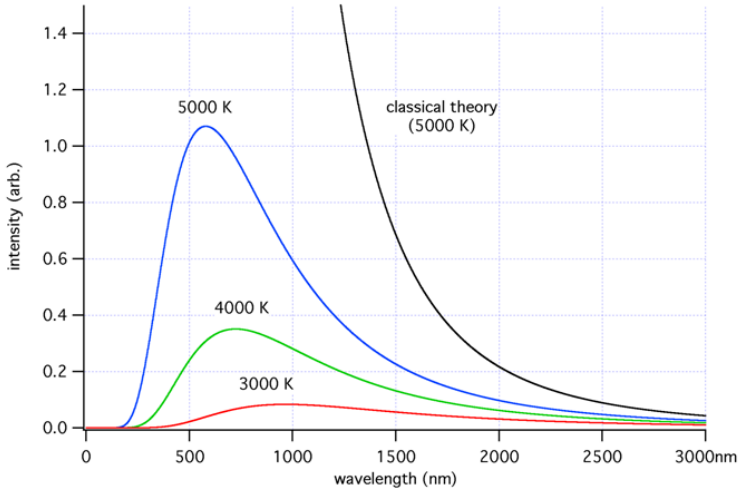

Figure 20 Theoretical curve of Planc's distribution on black body radiation. (Adopted from wiki web encyclopedia)

Experimentally, when the laser beam hits the cantilever, the focused spot rapidly heats up. Hence the heated area will irradiate the light at a certain wavelength (usually between 600nm and 750nm, as a result of incoming laser power control) in all directions. One of the irradiated light waves is sensed by the optical setup and arrives at the CCD camera after passing through the filter. A shining spot is then displayed on the screen, which reflects the real "heated-up" spot on the cantilever.

In the LASPAN process, we measure the laser power by a power meter (ThorLabs). The direct laser output power is 60mW, and the AFM optical system with beam splitter and objective has a 50% energy loss; hence, the maximum real laser output power applied on the tip is 30mW. Then the double spinner attenuator generally reduces it to about 12mW. Finally, the polarizer integrated in the half-way plate finely tunes it down to the desired power output. The fine tuning can be as accurate as 0.01mW.

We often use 10mW laser power output to find the flashing spot on a screen, followed by the cantilever's alignment. The final position of this flashing spot should be along the center axis of the probe, and at Xμm (line scan length) away from the projection of the sharp tip on the cantilever. Experimental images are found in Figure 21.

The optimization of applied thermal energy consequently decreases the laser's output power. A piece of paper is frequently used to block the laser beam, because the high power laser beam might burn out the tip itself. We also need to pay attention to the alignment of the flashing spot, a process which should be completed as quickly as possible. The longer it takes, the more damage will be inflicted on the probe. Usually

this process is completed within 30 seconds. Most of the time, an external illuminator is needed to provide illumination to the sample in order to aid in alignment.

Figure 21 Experimental images during laser optimization. Left: green spot on cantilever, after position optimization; Right: flash spot from blackbody radiation on cantilever, after position optimization

(d) Writing

After the laser beam's optimization, we block the laser beam with a piece of paper. We use a timer to set up the duration of the writing, and double check all parameters. Then the paper is removed and both the line scan and the timer immediately commence.

In the LASPAN writing, the AFM probe scans back and force on the sample surface in a designated area, with a laser spot simultaneously focused on the back side of the cantilever. The laser spot is at a fixed position, but the probe is raster scanning over the sample surface. Due to the integration of both systems, it is difficult to synchronize

the laser spot and tip. However, this does not really affect the thermal energy input, since the size of the whole probe is comparable to the focused laser spot.

When the writing time closes, the line scan is manually stopped, and immediately, the laser beam is blocked by the attenuator. Then, the tip is retracted from the surface by moving the scanner up little by little until it clears the contact area. The objective and scanner are then brought back to their original positions. The filter is removed and the internal AFM illuminator is inserted. We then document the values of three raster writing parameters: the writing time period t (second); line scan length $\boldsymbol{l}$ (μm), scan frequency f (Hz). Then the number of strokes N and the writing speed v (μm/s) can be derived as:

$$N = f \cdot t \tag{3.4}$$

and

$$v = \frac{2f \cdot l}{t} \tag{3.5}$$

Steps (a) to (d) form a complete cycle of the LASPAN process.

3.3.2 Four key parameters in the LASPAN process

There are four key parameters to control in the LASPAN process: the output laser power P (mW); the applied load ΔZ (μm, in terms of cantilever deflection); the writing speed v (μm/s); and the number of strokes N.

The various combinations of these four parameters produce different writing results. The details will be discussed in the next chapter.

CHAPTER IV

THERMAL ENERGY AND DISSIPATION

The LASPAN is a thermal process. Understanding the energy generation and the path of dissipation is important for advancing the LASPAN technique. In this chapter, the methodology to optimize the LASPAN process is developed and considerable experiments were carried out under various experimental conditions. In fundamental aspects, thermal energy and energy dissipation is discussed. This chapter is constructed by four sections. The first part discusses methods of process optimization. Characterization of resulting nanostructures is then introduced. The interfacial reactions between the Au-coated AFM probe and Si substrate is investigated. Subsequently, the frictional thermal energy induced through mechanical sliding is studied. Finally, we demonstrate the capability using experimental approach to evaluate temperatures on an AFM probe due to laser heating. The estimation of thermal energy through laser direct radiation is as well discussed.

4.1 Process matrix and optimization

The LASPAN technique utilizes an atomic force microscope (AFM) as a writing tool, an AFM probe coated by a thin metal layer as a "nano-pen," to perform raster sliding on a single crystal silicon substrate (100). During the process, the AFM tip absorbs the laser energy and is heated to several hundred degrees (lower than the melting temperature of coating materials). Meanwhile, a certain amount of heat is generated by the friction force between the AFM tip and contacting area (doped area) on the substrate.

Together, the mechanical sliding and laser introduce thermal stimulation into the highly localized region, in which eutectic reactions between the coating material and substrate are present.

As pointed out in the previous chapter, there are four independent parameters we can control during the whole process: output laser power P (mW); applied load ΔZ (μm, in terms of cantilever deflection); writing speed v (μm/s); and number of strokes N. Each of them contributes differently to the process. Using the Design of Experiments (DOE) approach, one parameter is tested out while other three are fixed.

The silicon substrate is immediately characterized by the same Nano-R2 atomic force microscope (AFM) after writing. The feedback is used to further process evaluation. A designated silicon probe is used to acquire all images. The result falls in one of the four categories mentioned above. In the current study, a LASPAN process matrix is constructed based on all the morphological results and set of parameters.

4.1.1 LASPAN Matrix and process optimization

A number of experimental trials were carried out, among which, 25 writings were found effective in generating nanostructures. A matrix based on recorded data was constructed, as shown in Table 2. The first four columns are the different values of those four key parameters used during the experiments: number of strokes; laser power; speed and load. The fifth column is the topography result, which will be discussed in detail in section 4.1.3. The explanation of the abbreviations are: “G” means grooves; “N” means non–visible structure; “P” means polished line trace; “Y” means line-like nanostructure

(above surface). The last column is the feedback message from surface characterization that helps improve the yield of the LASPAN process.

The polished line traces are created because of either excessive thermal energy (higher laser power than needed) or extra number of strokes; the grooves are present if too much mechanical load is applied (load is too high); non-visible structures are found are due to various reasons, such as small load or low writing speed. However, according to the matrix, we observe that the LASPAN process is not dominated by a single factor, but by the synergy of all four key parameters.

Table 2 LASPAN matrix with 26 recorded effective writings. Where, "G" means groove line trace; "N" means non obvious structure; "P" means polished line trace; "Y" means line-like nanostructure.

# of Strokes	Laser Power(P, mW)	Speed(v, μm/s)	Load(ΔZ, μm)	Line	Feedback
200	4.5	24	3	G	too many strokes
200	5.5	60	10	G	Not known
100	5	56	10	G	Too much load
90	5	30	9	G	Too much load
60	0	60	15	G	no heat
200	5	60	3	N	load too small
200	5	32	10	N	bad
200	4	32	10	N	bad
50	5	36	1	N	load too small
200	8	32	10	P	too hot, too many strokes
200	7.5	32	10	P	too hot, too many strokes
200	7	32	10	P	too hot, too many strokes
200	6	32	10	P	too hot, too many strokes
42	8	3.2	15	P	slow
54	6	3.2	15	P	slow
42	5	3.2	15	P	slow
42	7	3.2	15	P	slow
150	5.5	36	3	Y	good
150	5	60	5	Y	good
100	6	48	3	Y	good
84	4.5	14	15	Y	good
84	5.5	14	15	Y	good
60	4.5	60	15	Y	good
90	5.5	30	9	Y	good
100	5	52	14	Y	good
100	5	15	4	Y	good

To identify the best combination of all four parameters, we plotted all data points based on the LASPAN matrix, as shown in Figure 22. The horizontal axis is laser power and the vertical axis is speed. Each data point represents one writing. There is no doubt that thermal energy input (laser power, P) is a leading factor, since a significant change will occur if P changes. In most cases, the number of strokes (N) is purposely controlled as a similar value. The ultimate goal of the LASPAN process is to keep the value of N as a fixed minimum value. Hence, we only use writing speed (v) and load (Δz) as our second and third index to generate two plots.

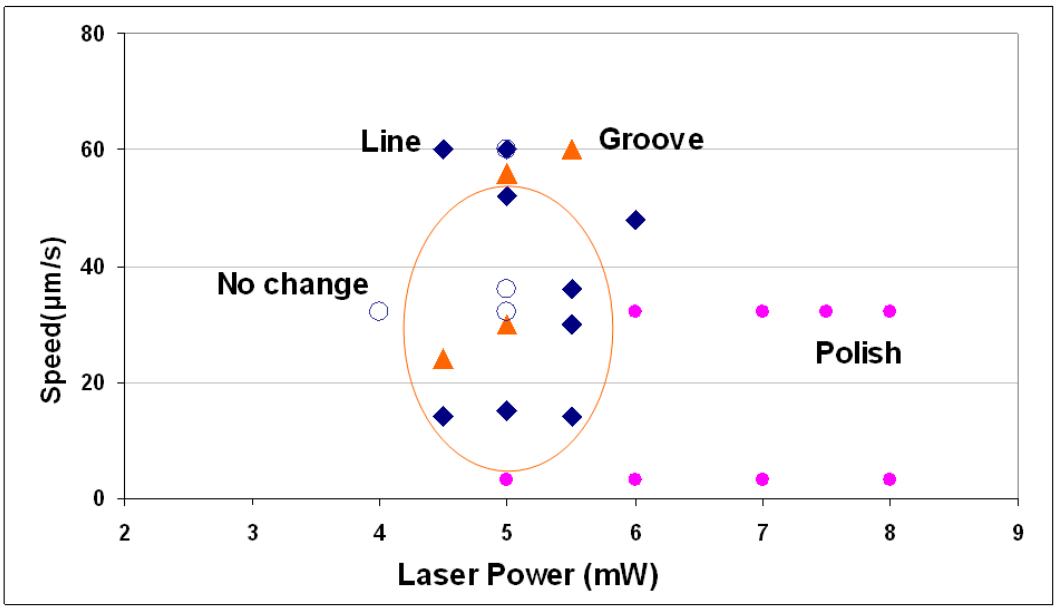

Figure 22 Plot of writing speed verse laser power. Each data point represents one type of writing result. All data points are separated by different shape and label. Circled area has most points in line-like nanostructure category.

The first plot (see Figure 22) contains three facts: (i) there is no change on the surface once P is less than 4.5mW; (ii) polished line traces are made if P is greater than or equal to 6mW; (iii) a line-like nanostructure can be formed with a broad range of v (from 15μm/s to 60μm/s). The circled area has the greatest number of data points representing lines. Notice that speed does not affect the process. Therefore, we introduced load, in addition to writing speed. The second plot (see Figure 23) is constructed based on speed*load versus laser power, which represents the combined effect of v and Δz. One can read from this plot that most of data points representing line-like nanostructures are included in the circled area. This indicates that speed and load are two complementary parameters during the LASPAN process.

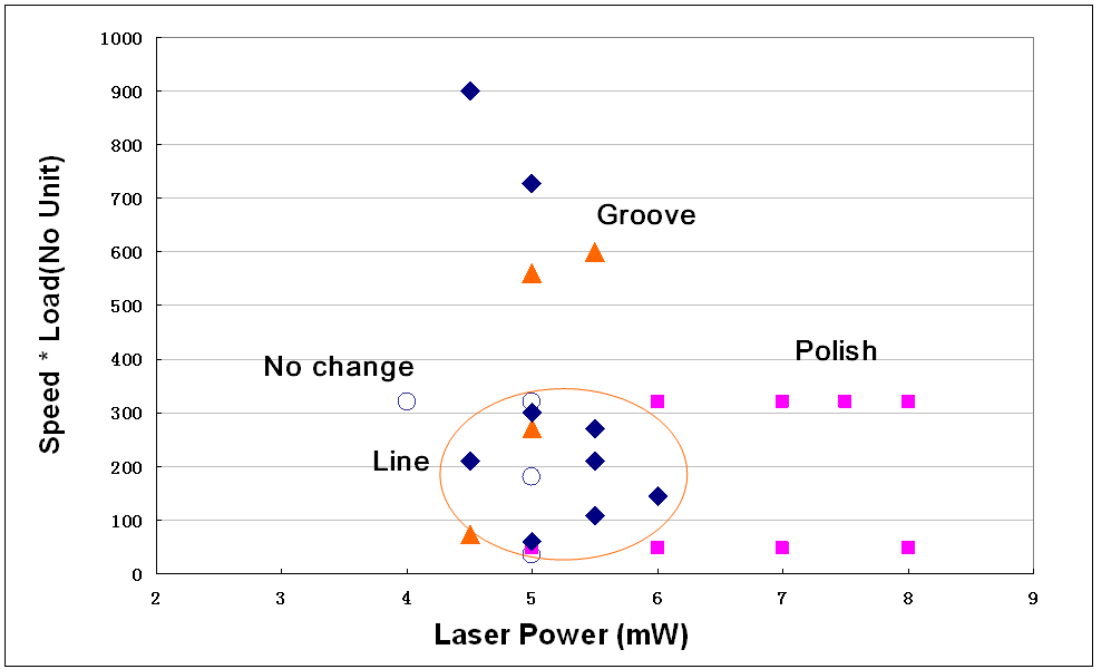

Figure 23 Plot of writing speed*load vs. laser power. Each data point represents one type of writing result. All data points are separated by different shape and label. Circled area has most points in line-like nanostructure category.

From the LASPAN matrix and these two plots, we identify the optimized parameters set needed to fabricate line-like nanostructures, as shown in Table 3. In this figure, the range of each parameter is given, as well as a constraint between speed and load.

Table 3 Optimized parameters set and a constraint for LASPAN to fabricate line-like nanostructures.

(i) Laser Power *P*: 4.5~6mW
(ii) Speed *v*: 15~60 μ m/s
(iii) Load Δz: 3~15 μ m
(iv) # of Strokes: 60~150
(v) Constraint:

$$|v \cdot \Delta z| <= 300$$

where $|v \cdot \Delta z|$ *is the pure value without units of speed and load.*

4.1.2 AFM topography imaging

Normally, an AFM is a tool for surface imaging (see schematics in Figure 24). The sharp tip is used for raster scanning over a sample surface, while the laser and light lever act as force sensors. During the scanning, the tip senses the repulsive force (more precisely, Van de Waals force) between the atoms on the very front tip and substrate. The position change of the light cantilever is recorded and processed by the feedback control unit (FCU) of the system. The recorded electric signal is then converted through software and forms a final surface morphology image.

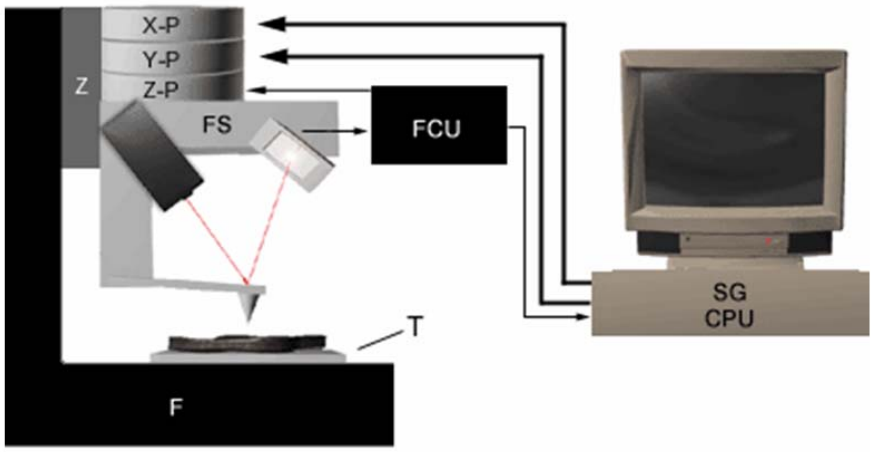

Figure 24 Schematics of an AFM (courtesy of PNI)

There are two common imaging modes associated with this AFM: contact mode and close contact mode (tapping mode). In the contact mode, the deflection between tip and sample is kept constant, which is proportional to the force between the tip and surface. The deflection is measured during a scan. Height images and lateral force images are generated in this scanning mode. In the close contact mode, the light cantilever vibrates over the surface at a given frequency during the scan. The vibration amplitude and phase change when the tip interacts with the sample. These changes are measured and can be related to the force on the sample surface. Height images and phase images are obtained through this mode. Generally, the height image acquired in close contact mode will offer higher resolution than that in contact mode. In this work, unless specified, all the images are taken in close contact mode.

4.1.3 Defining categories

The LASPAN process modifies the substrate surface in four different categories: non-visible structures; polished line traces; grooves; and line-like nanostructures. Obviously the last one represents the most favorable result of this technique. We will demonstrate topography and phase images together with a line analysis in each category (except the first one) in sequence. Note that in the line analysis, the selected line represents the average dimensional information. We proceed given the following definitions:

(a) Non-visible structures: no significant change of morphology of the same scanning area before and after writing. The images are not shown since there are no observable nanostructures.

(b) Polished line trace: a line trace follows the tip movement, and the width of the line trace is much larger than the tip radius (usually <100nm for a newly coated probe). More importantly, the roughness within the trace is one order lower than the original surface. The height and phase images are shown in Figure 25. The whole scanned area is 8μm. A clear polished trace is found in the center of the image, and a few particles (dust on the substrate) are present along the line edge; the corresponding 3-dimensional image can be found in Figure 26. The line analysis shows that the width and depth of this polished line trace are 864μm and 1.0nm, respectively (see Figure 27). Figure 28contains the roughness comparison. The overall roughness of the surface is 29.98nm, but the selected area (green) inside the polished line trace has the roughness 0.99nm. This means that the line trace was polished when the AFM probe scanned over.

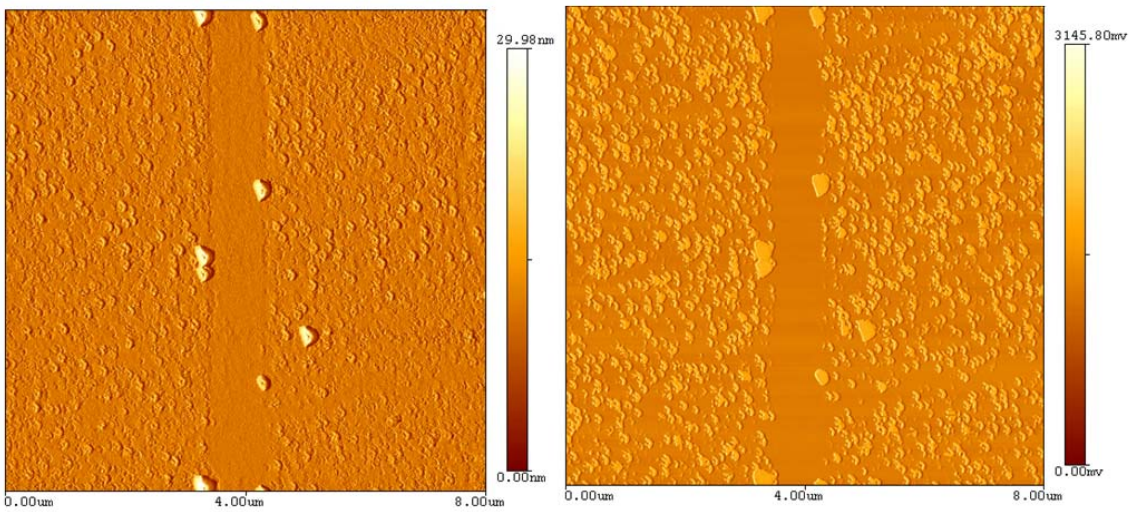

Figure 25 2D image of a polished line track. Left: height image; Right: phase image

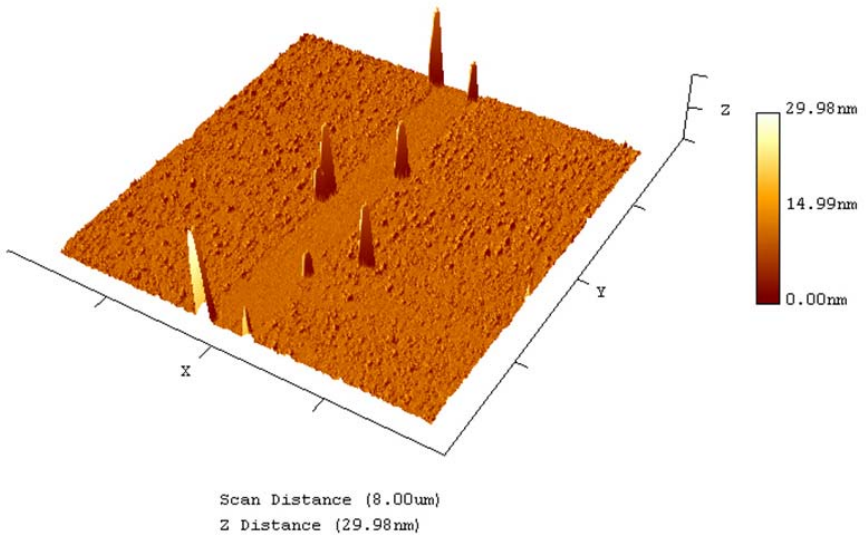

Figure 26 3D image of a polished line track.

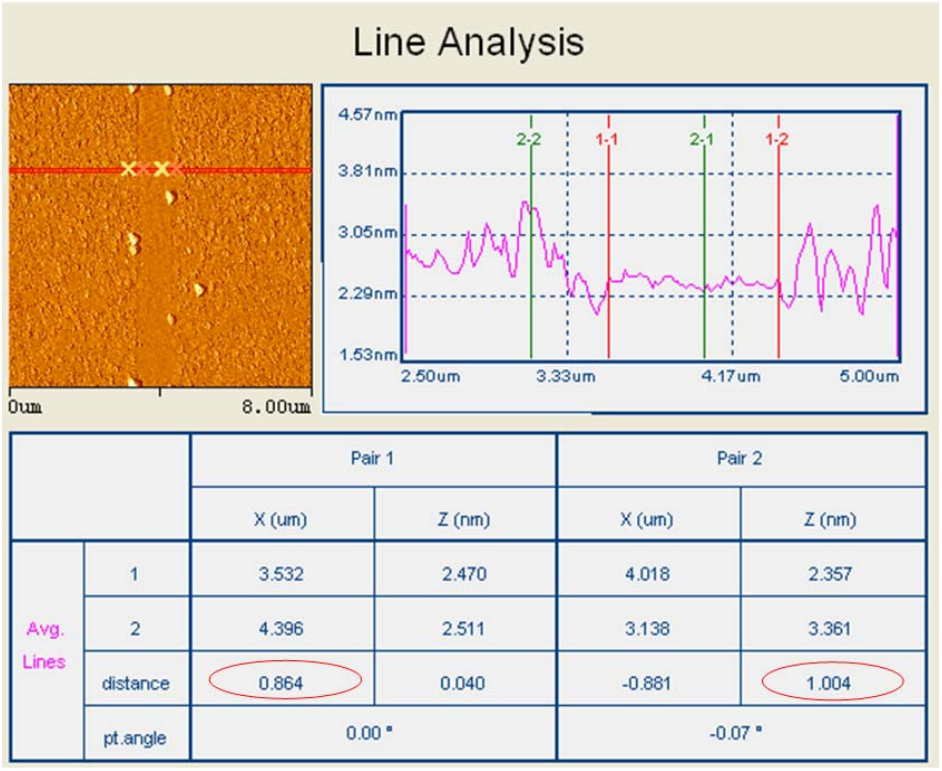

		Pair 1		Pair 2	
		X (um)	Z (nm)	X (um)	Z (nm)
Avg. Lines	1	3.532	2.470	4.018	2.357
	2	4.396	2.511	3.138	3.361
	distance	0.864	0.040	-0.881	1.004
	pt.angle	0.00 °		-0.07 °	

Figure 27 Line analysis of a polished line track.

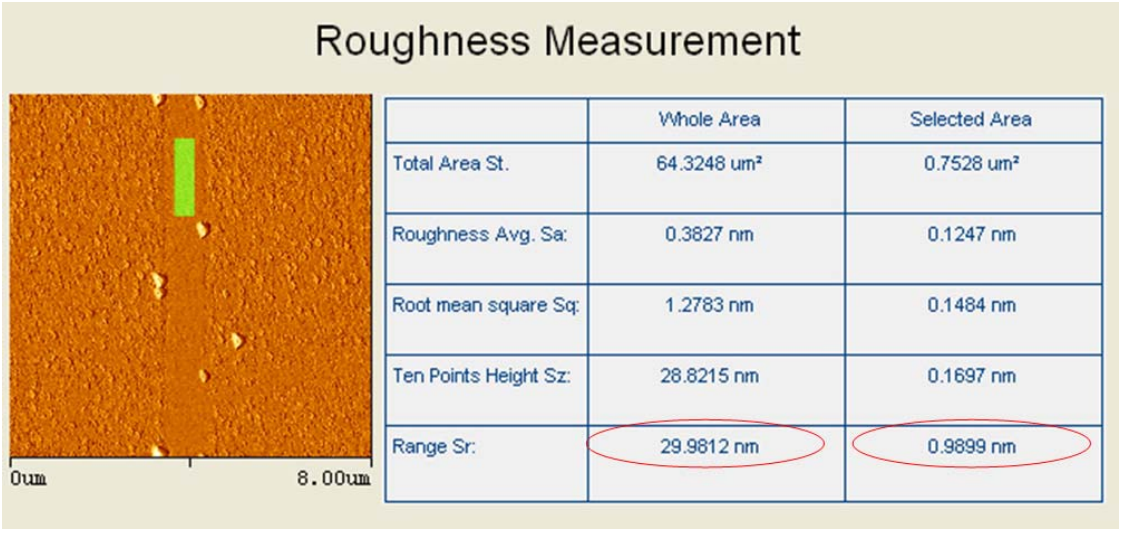

	Whole Area	Selected Area
Total Area St.	64.3248 um²	0.7528 um²
Roughness Avg. Sa:	0.3827 nm	0.1247 nm
Root mean square Sq:	1.2783 nm	0.1484 nm
Ten Points Height Sz:	28.8215 nm	0.1697 nm
Range Sr:	29.9812 nm	0.9899 nm

Figure 28 Roughness analysis of a polished line track.

(c) Groove line traces: a line trace that follows the tip movement, with the width of the line trace being comparable to the tip radius. The scanned area is lower than the original surface, and the topography is literally a groove. The height and phase images are shown in Figure 29. The whole scanning area is 10μm. A clear groove line trace is found in the center of the image. The entire track is straight, and the line width maintains to be uniform through out. A three-dimensional image at the same scale can be found in Figure 30, and the line analysis of the groove line track is shown in Figure 31. The width and depth of the groove line track are 148nm and 0.7nm, respectively. In this category of results, the AFM tip plows the surface during writing.

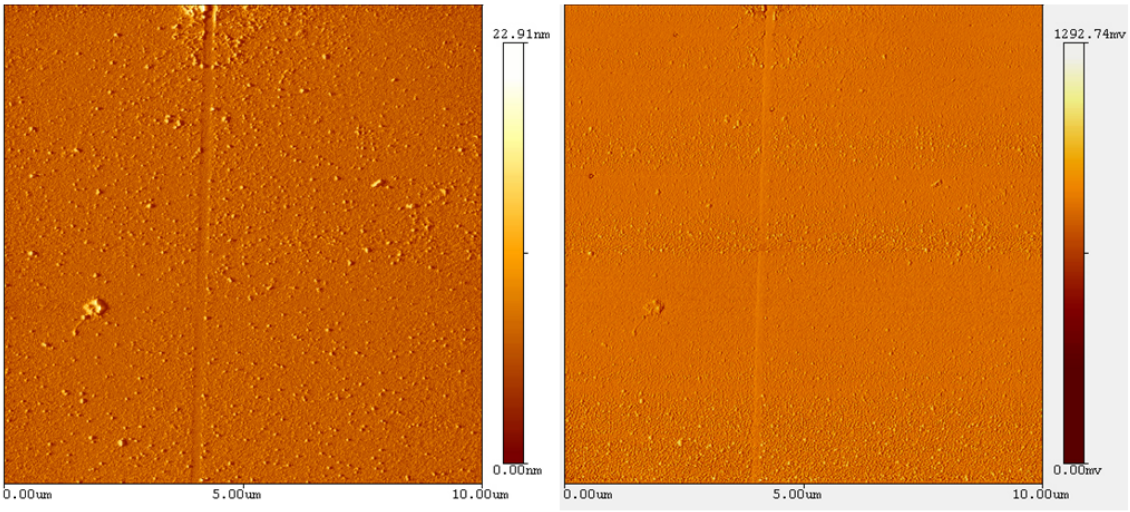

Figure 29 2D image of a groove line track. Left: height image;
Right: phase image

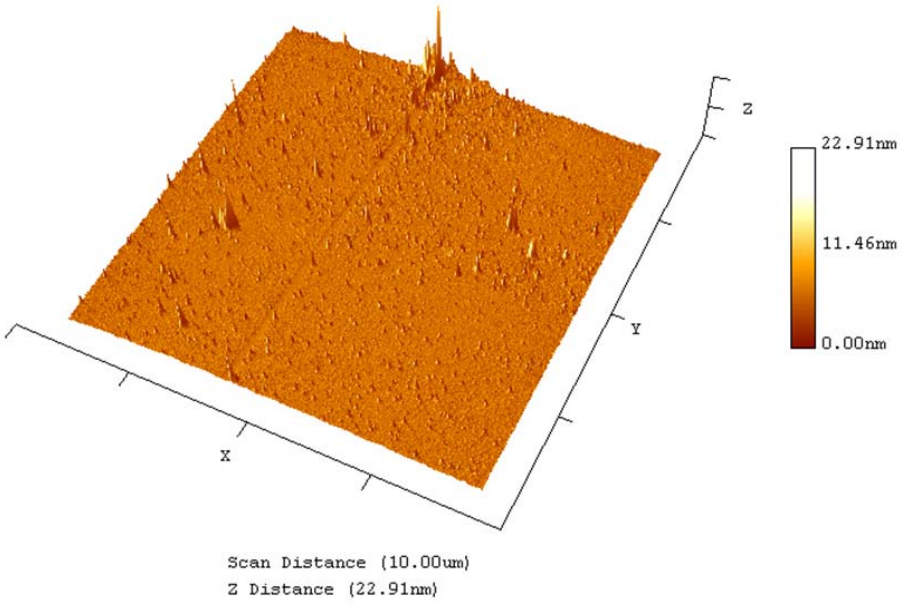

Figure 30 3D image of a groove line track.

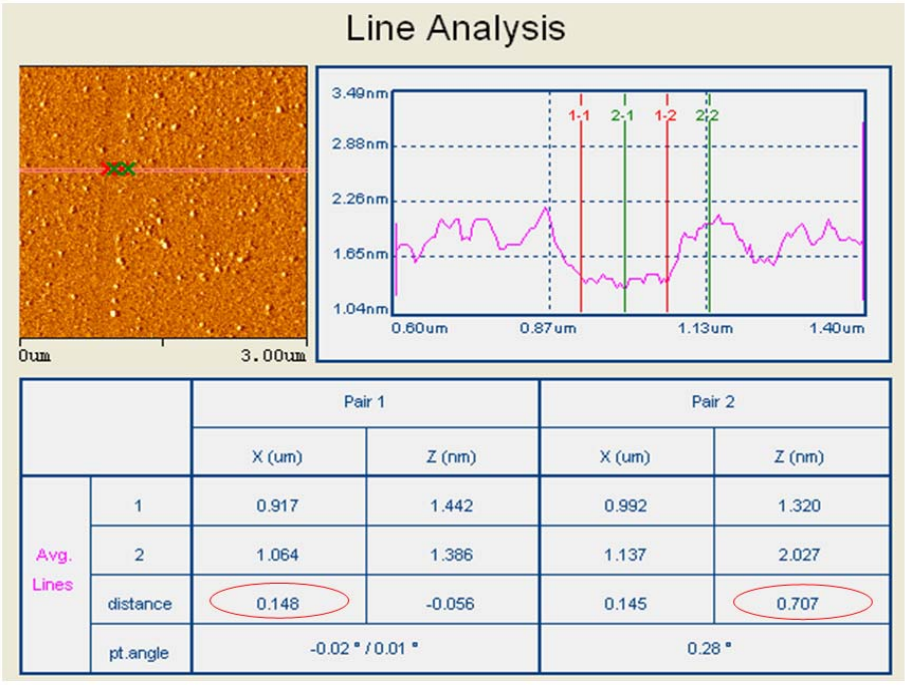

		Pair 1		Pair 2	
		X (um)	Z (nm)	X (um)	Z (nm)
Avg. Lines	1	0.917	1.442	0.992	1.320
	2	1.064	1.386	1.137	2.027
	distance	0.148	-0.056	0.145	0.707
	pt.angle	-0.02 ° / 0.01 °		0.28 °	

Figure 31 Line analysis of a groove line track.

(d) The last category of results is the output of the LASPAN process, and as we expected, a line-like nanostructure is found. We define the line-like nanostructure as a line trace which follows the tip movement, with the width of the line trace being comparable to or less than the tip radius. The fabricated structure has a certain height above the original surface. The topography is literally a line-like nanostructure, or more precisely, a nanobelt. The height and phase images are shown in Figure 32. The whole scanning area is 18.7μm. A clear line trace is found in the center of the image. A closer view of this line shows that materials adhered to the substrate and formed nanostructures (see Figure 33). The whole track has a certain shift in the range of 50nm, which is due to the tip torsion during writing. A three-dimensional image at the same scale (18.7μm) can be found in Figure 34, and the line analysis of the line-like nanostructure is shown in Figure 35. It is found that the width and height of the line-like nanostructure are 52nm and 0.55nm, respectively. The total length of this line is 30μm. In this category of results, the AFM tip fabricates the nanostructure over the surface during the writing. The nanostructure is highly localized in the tip scanning area.

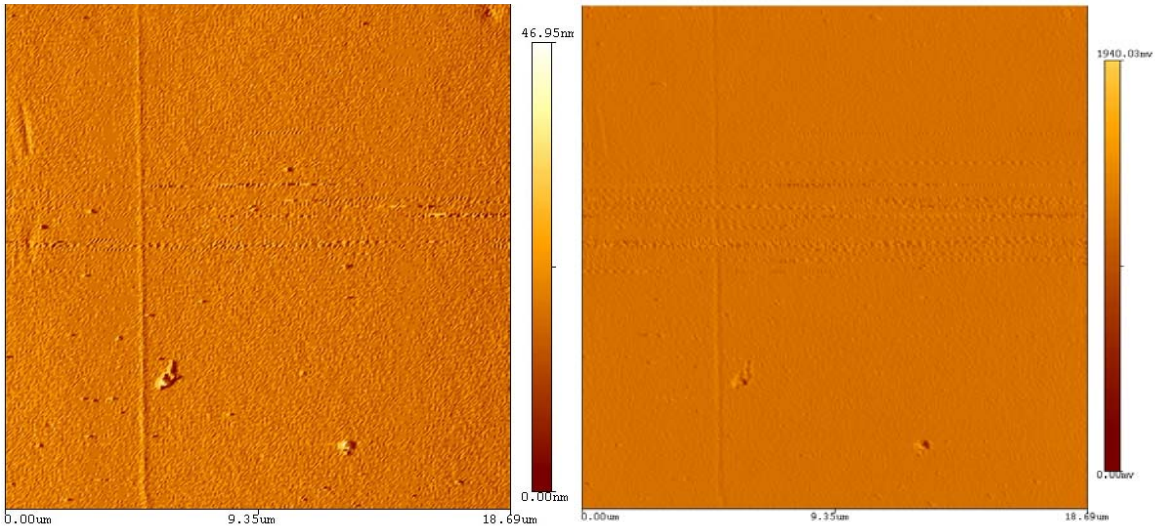

Figure 32 2D image of a line track. Written at 5mW, 60um/s, 150strokes

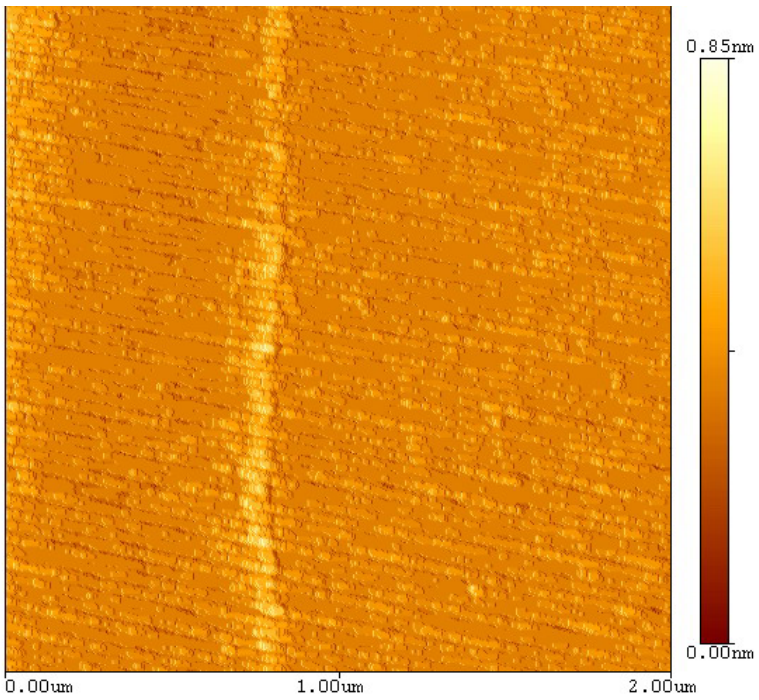

Figure 33 Closer view of the line structure, scanning area: 2µm

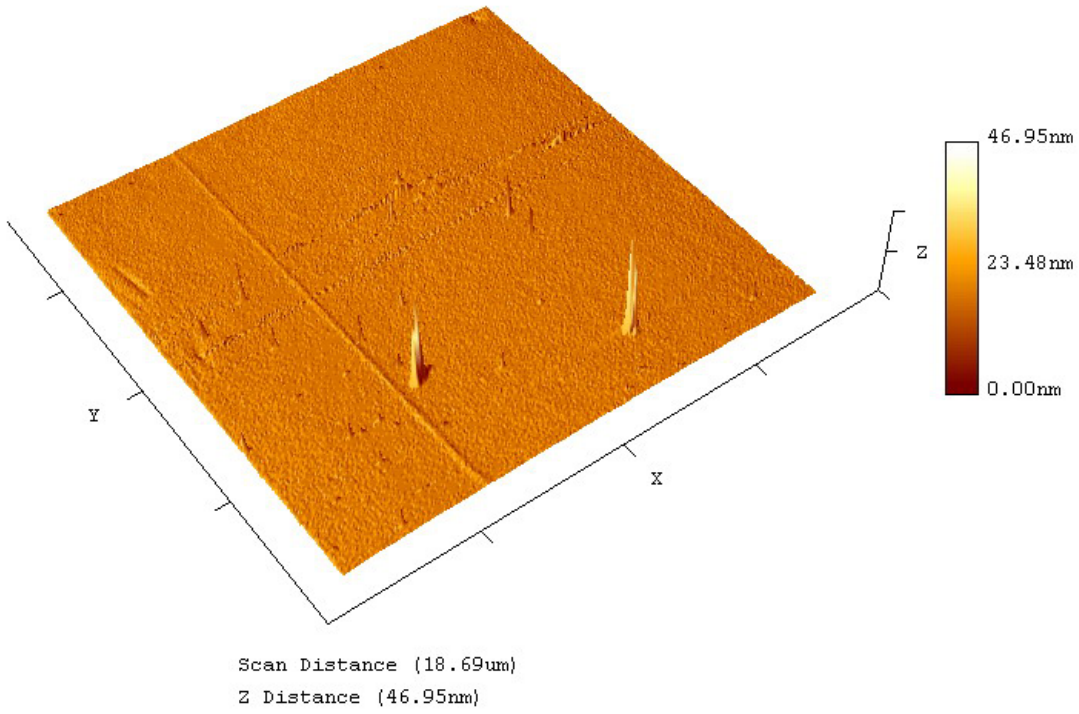

Figure 34 3D image of a line track.

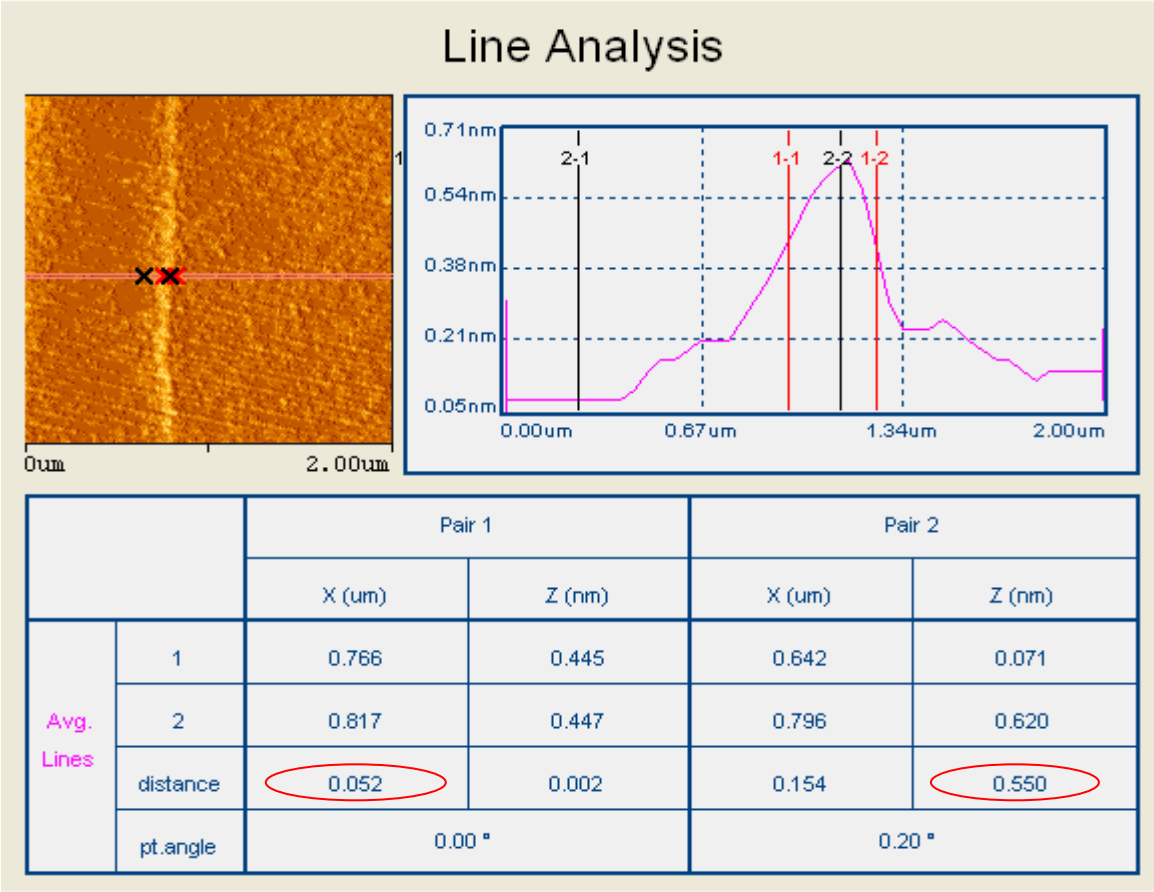

		Pair 1		Pair 2	
		X (um)	Z (nm)	X (um)	Z (nm)
Avg. Lines	1	0.766	0.445	0.642	0.071
	2	0.817	0.447	0.796	0.620
	distance	0.052	0.002	0.154	0.550
	pt.angle	0.00 °		0.20 °	

Figure 35 Line analysis of a line track.

4.2 Energy dissipation

We have demonstrated different results from LASPAN using a different parameters set, in which each factor contributes. A highly localized area is formed when the gold coated AFM probe is in contact with the silicon surface. Both mechanical sliding and laser radiation provide thermal energy, and a eutectic reaction between gold and silicon is present. This is indeed an alloying process at nanometer scale (nanoalloying), and it is driven by thermal energy. However, based on the results from

the LASPAN matrix, the thermal energy input must be within a certain range. At one extreme, the nanoalloying process will not happen if the thermal energy input is not enough; at the other extreme, the materials will melt and be removed if the thermal energy input is too high. The nanoalloying process only takes place when the right amount of thermal energy is introduced, for line-like nanostructures to be fabricated. We define the total thermal energy input required for this nanoalloying process as E_{Tot}, and we have:

$$E_{Tot} = E_{Mech} + E_{La} \tag{4.1}$$

where E_{Mech} is the energy input from mechanical sliding; E_{La} is the energy input from laser radiation.

In the next two sections, the estimation of mechanical energy input and laser radiation input will be discussed respectively.

4.3 Interfacial interactions between tip and substrate

In this section, we use a nanoscale approach to study the wear behavior of eutectic material systems. Simple sliding experiments (without laser) were conducted using gold (Au) coated AFM probes to slide on a single crystal silicon (Si) wafer. The extreme dimensions of the AFM probes were observed using high resolution techniques. We found that nanowear resulted from mixed modes of abrasion and adhesion. We propose that with the addition of frictional heating, it is possible to observe morphological change due to eutectic reaction. The present research contributes to fundamental understanding of nanoscale wear mechanisms.

4.3.1 Mechanical sliding experiments

A silicon nitride (Si_3N_4) AFM probe (Contact Mode probes from Nanoink) was used in this study. The probe was coated with an adhesion layer of 5nm thick chromium (Cr) and subsequently, a 145 nm thick gold (Au) layer. The film was deposited through vacuum evaporation. A single crystalline silicon (100) wafer was used as the substrate, and an atomic force microscope (AFM, Nano-R2, PNI) was used for sliding experiments as well as characterization.

The sliding experiment was processed in a contact mode. During the probe's approach, there were two sequential steps. The probe was first brought into physical contact with the sample surface in the approaching mode (controlled by the software), with no stress applied on the cantilever. The probe was then forced down with the cantilever bent. The amount of bending can be controlled through the software with the number of down steps. A total of three steps were applied and each step was 5μm down. The sliding speed was set at 480μm/s, with the test duration at 0, 5, 10, 20, 40 and 100 strokes. At each point, the probe was characterized using a field emission scanning electron microscope (FE-SEM, Zeiss1350). Chemical composition at the probe tip was analyzed using energy dispersion spectroscopy (EDS). Micro- and nanohardness tests were conducted using a Vickers hardness tester and a nanoindenter (Hysitron). The morphological analysis of the wear track on the silicon substrate was carried out using the same AFM with a different probe.

4.3.2 Morphology of AFM tips

The Au-coated probe slid against the silicon. The applied load (N) was 504nN and the sliding speed was 480μm/s[124].An FE-SEM was used to observe the wear scar at fixed sliding distances (0, 5, 10, 20, 40 and 100 stokes). Results are shown in Figure 36, which is the top view of the Au coated probes before and after sliding; in this figure, the center plateau is the wear scar of coated probes indicating abrasive wear.

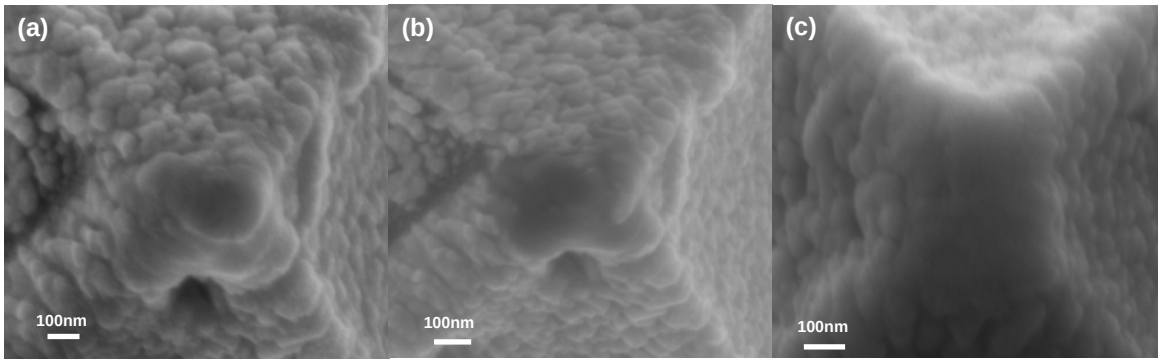

Figure 36 SEM images of AFM probes. (a) Au-coated probe before sliding (b) Same probe after sliding 5 strokes (c) Same probe after 100 strokes

To quantitatively study the abrasive wear behavior, we defined the diameter of the wear scar (D) as the average diagonal length of the observed rectangle. The diameter of the wear scar versus the number of strokes was plotted (Figure 37). The error bars reflect the systematic uncertainty. As seen in the figure, the final scar diameter reaches the size of 400nm, which is much greater than the original tip diameter (less than 100nm). This indicates the material's removal due to mechanical sliding.

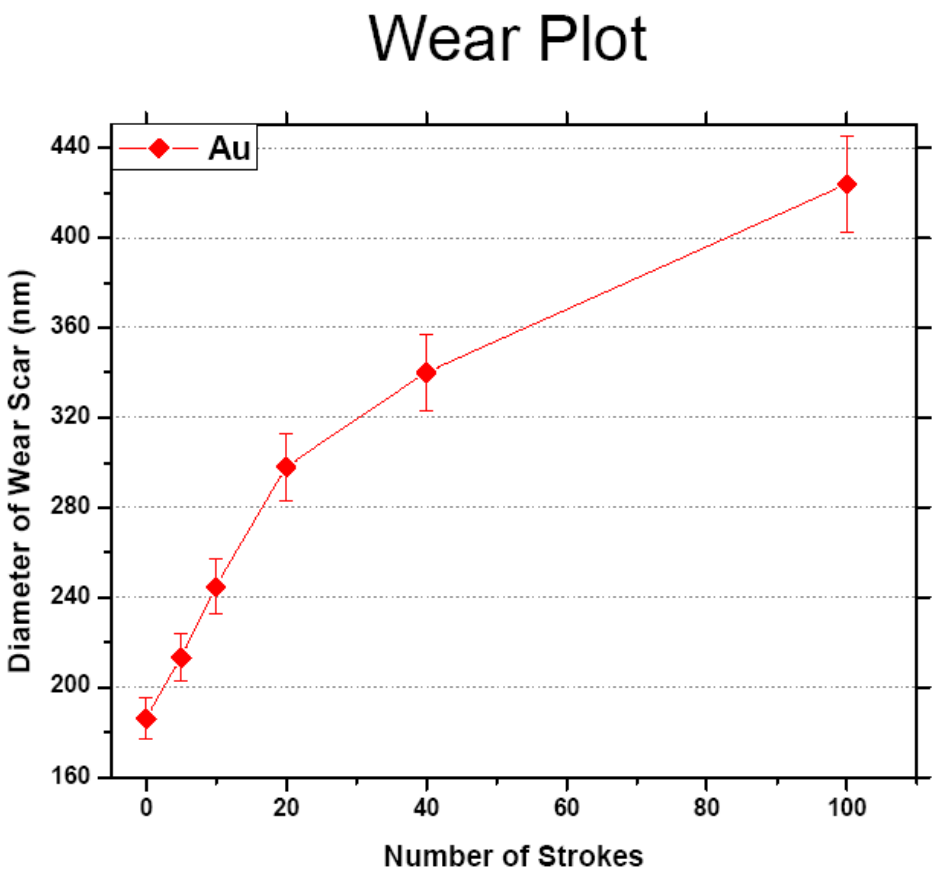

Fig 37 Plot of diameter of wear scar vs. # of strokes for Au coated probe. The probe is showing abrasive wear.

4.3.3 Chemical analysis

Energy dispersive x-ray spectroscopy (EDS) analysis was conducted on both unused and worn probes. The areas of detection were exactly the same on each tip. The accelerating voltage was 20kV. The data is shown in Table 4. Here the silicon weight percentage within the interested area significantly changed, both before and after sliding, by 22.73%: silicon was transferred from the substrate surface onto the AFM tip due to sliding.

Table 4 Au weight% and atomic% on probe before and after sliding

	Element	%Wt		Element	%Atomic
Before sliding	Au	89.32	Before sliding	Au	54.39
	Si	**10.68**		Si	**45.61**
After sliding	Au	66.59	After sliding	Au	22.13
	Si	**33.41**		Si	**77.87**

4.3.4 "Wear" tracks

The morphology of the silicon substrates was characterized using the same AFM with a silicon probe. Results are shown in Figure 38. A well-defined line of 240 nm, is seen here, in addition to a wear groove. This structure was seen in the Au wear tracks as a developed line.

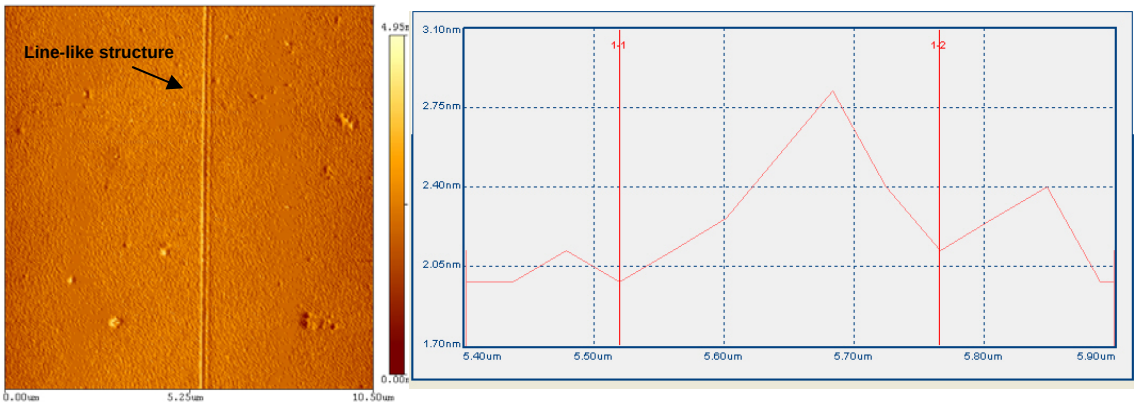

Figure 38 AFM height images and profile of silicon surface after scratching. A line-like structure was found along the track of sliding. The line is 60um long, average height and width are 0.9nm and 240nm, respectively

To investigate whether the hardness of these two materials is responsible for the nanowear, we conducted micro hardness tests on bare silicon wafers and gold thin films. The results (data not shown) indicated that silicon has higher hardness while gold has lower ($H_{Si} > H_{Au}$): Au deforms more than Si.

We define the tip wear volume as V_w, the volume of the line structure as V_l. Here V_w can be estimated from the diameter of the wear scar (D) from the AFM tip, V_l can be estimated from the dimensions of the line structure. It is shown in Table 5 that V_l is greater than V_w. The volume comparison indicates that the line is indeed formed from mixed Au-Si.

Table 5 Volume comparison between wear volume on the probe V_W and volume of the line structure V_l. One can see $V_l > V_W$

	$V_W(nm^3)$	$V_l(nm^3)$
Au-Si	**$1.2*10^7$**	**$1.3*10^7$**

In the EDS analysis, silicon was found to adhere onto the Au tip during sliding. Well-defined line structures were found on the substrate in addition to the groove. All the facts suggest that in the highly localized area, the stress induced nanowelding, such that the tip material was transferred onto the Si substrate. The wear mechanism of an Au-Si system at the nanometer scale was found to be a combination of abrasive wear and localized adhesive (transfer) wear.

4.3.5 Thermal energy estimation due to mechanical sliding

In mechanical sliding, stress-induced friction generates heat, which is the main contribution to the thermal energy input of E_{Mech}.

$$E_{Mech} = \alpha E_f \tag{4.2}$$

where α is the absorption coefficient, such that $0 < \alpha < 1$.

Assuming the frictional force is F_t, and the sliding distance is L, the frictional energy E_f can be expressed as

$$E_{Mech} \propto E_f = F_t \cdot L \tag{4.3}$$

where F_f can be estimated as a tangential component of the load N, thus

$$F_f \simeq N \tan\theta \tag{4.4}$$

where θ is half of the top angle (35degree) of the AFM pyramid tip. Notice that N is 504nN, and L is the total distance of 100 strokes of sliding (120μm per stroke). E_f can be calculated as 1.9×10^{-9} J or 1.2×10^{10} eV.

As mentioned earlier, gold-silicon (Au-Si) is a simple eutectic system [125]. The equilibrium phase diagram is presented in Chapter II (Figure 10). The eutectic temperature for bulk Au-Si binary systems is 363°C. Observed mixed phases due to eutectic reactions for Au-Si systems have been reported [126]. Frictional heating is a widely accepted concept [127] and our results indicate the presence of heating through a eutectic reaction. The low eutectic temperature for Au-Si means it would require low energy to trigger the Au-Si reaction. This raises the question of whether frictional energy would be enough for the reaction to take place.

The heat change for one specific material can be calculated as:

$$\Delta Q = m \cdot c_p \cdot \Delta T = \rho \cdot V \cdot c_p \cdot \Delta T \tag{4.5}$$

where ΔQ is the heat change, m is the mass of material, c_p is the specific heat capacity, ΔT is the temperature change, ρ is material density and V is the volume of material. From equation (4.4), the thermal energy needed for eutectic reactions to take place within the highly localized area can be estimated. Let V be the volume of the effective contact volume (equal to the largest wear scar diameter*thickness of coating layer*scanning length, i.e. 3.8×10^{9}nm^3), and ΔT be the temperature difference between Au-Si eutectic point and room temperature, i.e.

$$\Delta T = 363^o C(636K) - 27^o C(300K) = 336K \tag{4.6}$$

The density of gold and silicon are $19.3 g \cdot cm^{-3}$ and $2.33 g \cdot cm^{-3}$, respectively; the specific heat capacity of gold and silicon are $129.1 J \cdot kg^{-1} K^{-1}$ and $700\ J \cdot kg^{-1} K^{-1}$, respectively. Plugging in these numbers, we get

$$\Delta Q(Au) = 3.2 \times 10^{-9} J \tag{4.7}$$

$$\Delta Q(Si) = 2.1 \times 10^{-9} J \tag{4.8}$$

$$2.1 \times 10^{-9} J < \Delta Q(Au - Si) < 3.2 \times 10^{-9} J \tag{4.9}$$

where $\Delta Q(Au - Si)$ represents the minimum heat required to reach eutectic temperature in the highly localized area. Recalling the value of E_f, one can read

$$E_{Mech} < \Delta Q(Au - Si) \tag{4.10}$$

This means that in the Au-Si system, the pure frictional heat is not high enough to raise the localized temperature to the eutectic point.

In this section, we conducted a simple sliding experiment with an AFM to investigate wear mechanism in an Au-Si system. It was found that wear behavior was a combination of tip material abrasion and localized adhesion. Frictional heating was responsible for triggering all interactions at the interface. Energy analysis indicated that the Au-Si system requires more thermal energy for interfacial reactions, in addition to the thermal input from pure mechanical sliding. This issue will be addressed by introducing laser direct radiation. This novel approach proved to be a powerful tool for nanoscale wear analysis that was previously not possible.

4.4 Temperature distribution through laser direct radiation

Thermal energy input from laser radiation is critical in the LASPAN process, as the laser will provide sufficient thermal energy for the gold-silicon system by heating up the AFM probe. In this research, we designed and constructed a near infrared (NIR) pyrometer microscope to measure the temperature at the AFM tip, upon which the laser beam is projected. We used a NIR pyrometer because the target temperature's spectrum peak is mostly in near infrared or infrared regions. The temperature leads to the estimation of laser radiation induced thermal energy input.

4.4.1 NIR pyrometer microscope

A pyrometer is defined as a non-contacting device which intercepts and measures thermal radiation. The word pyrometer comes from the Greek words for fire and meter; it literally means: "an instrument for measuring temperatures especially when beyond the range of mercurial thermometers" (from Merriam-Webster Dictionary). Usually the temperature of the object's surface is determined from the pyrometer's measurement.

The schematic diagram of our home-made NIR pyrometer microscope is found in Figure 39. This pyrometer has an optical system and a detector; the optical system focused the thermal radiation onto the detector. The thermal radiation or irradiance is collected by the detector and relayed to the detector output signal, which is temperature T. The thermal radiation and temperature are related through the Stefan-Boltzman law:

$$j^* = \varepsilon \sigma T^4 \tag{4.11}$$

Where j^* is the thermal radiation or irradiance, σ is the Stefan-Boltzmann constant, and ε is the emissivity of the object.

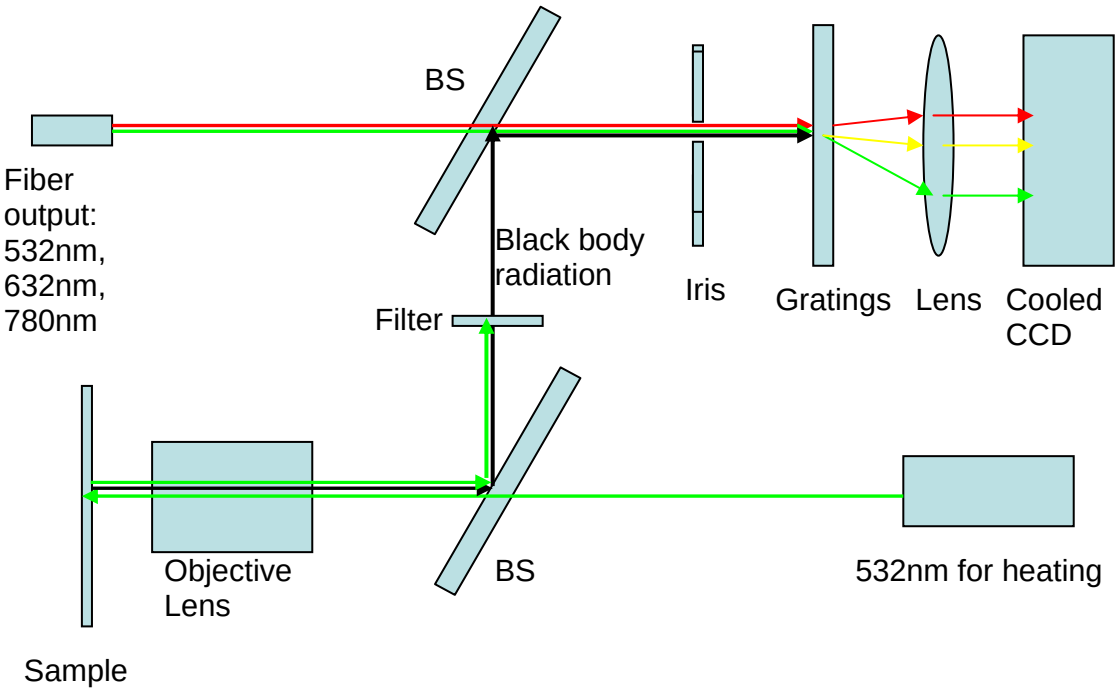

Figure 39 Schematic diagram for NIR Pyrometer Microscope

In our pyrometer design (see Figure 39), the bottom part is exactly the same as the setup in our LASPAN system, in order to provide accurate measurement. A green laser with a wave length of 532nm was used for heating. It passed through a beam splitter (BS) and a 10X objective, finally reaching the sample (the same AFM probe used in the LASPAN process). The filter blocked the reflected green light. When the tip was heated up, the thermal blackbody radiation signal was emitted from the sample, and arrived at the detector (cooled CCD camera) along the path of the black arrow (see Figure 39). In the meantime, three laser beams with different wavelengths (532nm,

632nm, and 780nm) were projected on the detector through another path. These three laser beams made three bright spots on the CCD screen. We used these spots as references to help calibrate the thermal irradiation signal. The thermal irradiation signal on the detector was a spread band, inside of which the intensity had a certain distribution. All the values of intensity at each pixel on the CCD screen were recorded. The laboratory setup of this NIR pyrometer is shown in Figure 40.

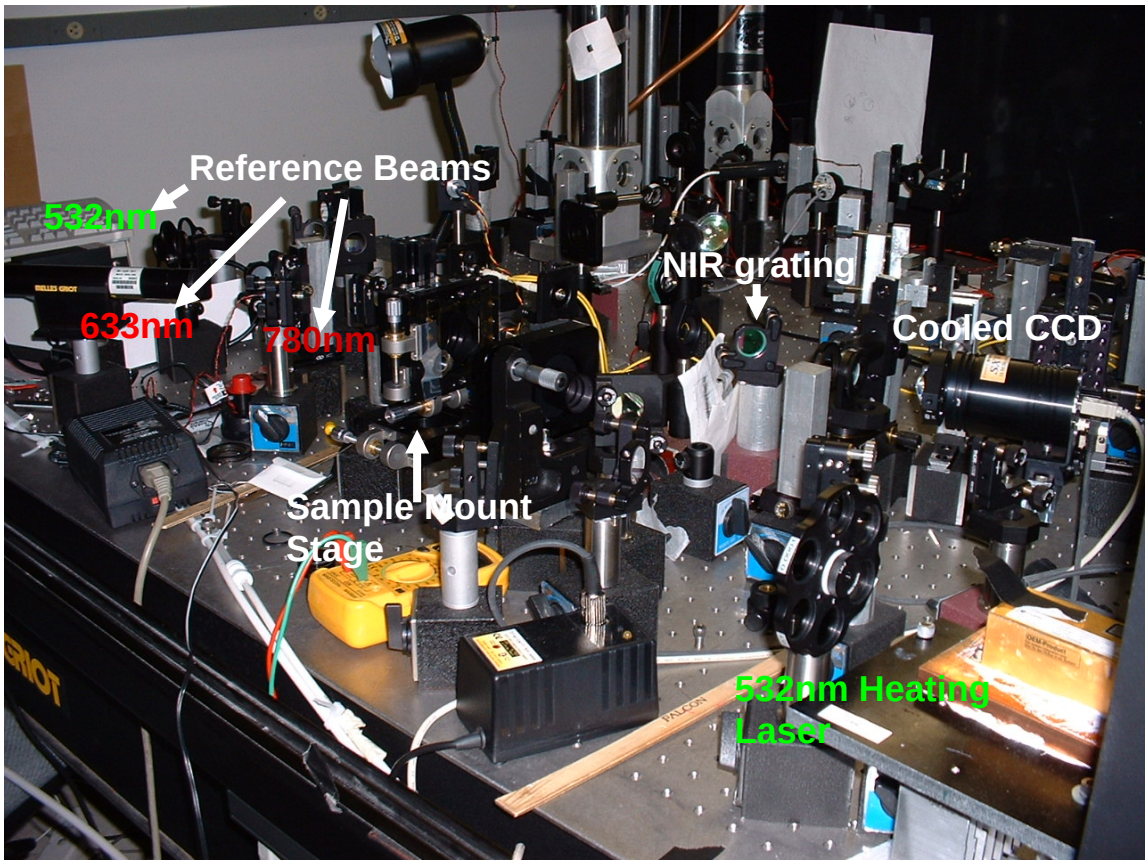

Figure 40 Real set-up for NIR pyrometer microscope

4.4.2 System calibration

A special light bulb (from Intematix Corp.) was used to calibrate the NIR pyrometer system. The filament of this bulb is designed to be thermally stable as long as a passing direct current is less than 1.5319A. Each given current electrically heats up the filament to a certain temperature T. Therefore it emits the thermal irradiation signal corresponding to one of the color temperatures for the value of T, as given by the manufacturer (see Figure 41). We set the direct current of the light bulb at those three different values, and measured the irradiation signal with the NIR pyrometer microscope. The experimental results, together with the theoretical curve, are also shown in Figure 41. The effective wavelength of the detector ranges from 740nm to 940nm. In the same figure, the vertical axis represents intensity (normalized no units). We can generate a compensation curve by a simple operation: divide the value of each data point in the experimental curve by the value of the corresponding data point in the theoretical curve, and then re-plot all the data points as a compensation curve. This compensation curve is used for future calibration of experimental data.

Calibrated lamp (Intematix Corp.)
I=1.5319A, CCT=3000K; I=1.2200A, CCT=2493K; I=1.0000A, CCT=2063K

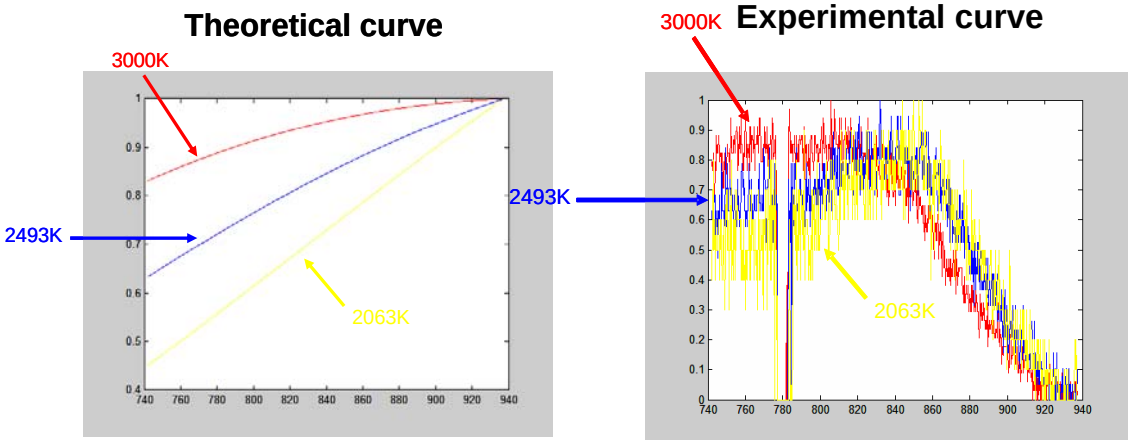

Figure 41 Calibration of this NIR pyrometer. Left: theoretical curve of three color temperatures. Right: Normalized experimental curve due to intensity uniformity

4.4.3 Laser irradiation on probe and temperature measurement

In this experiment, we applied 12mW laser output power onto the AFM probe. The data was collected by NIR pyrometer, then normalized and calibrated by the compensation curve. The results are shown in Figure 42. The normalized experimental curve was then fitted by three different theoretical curves at T=500K, 800K and 1000K, respectively; the experimental curve best fit the theoretical curve of T=800K. This means that the temperature at the laser spot is 800K when the incoming laser power is 12mW.

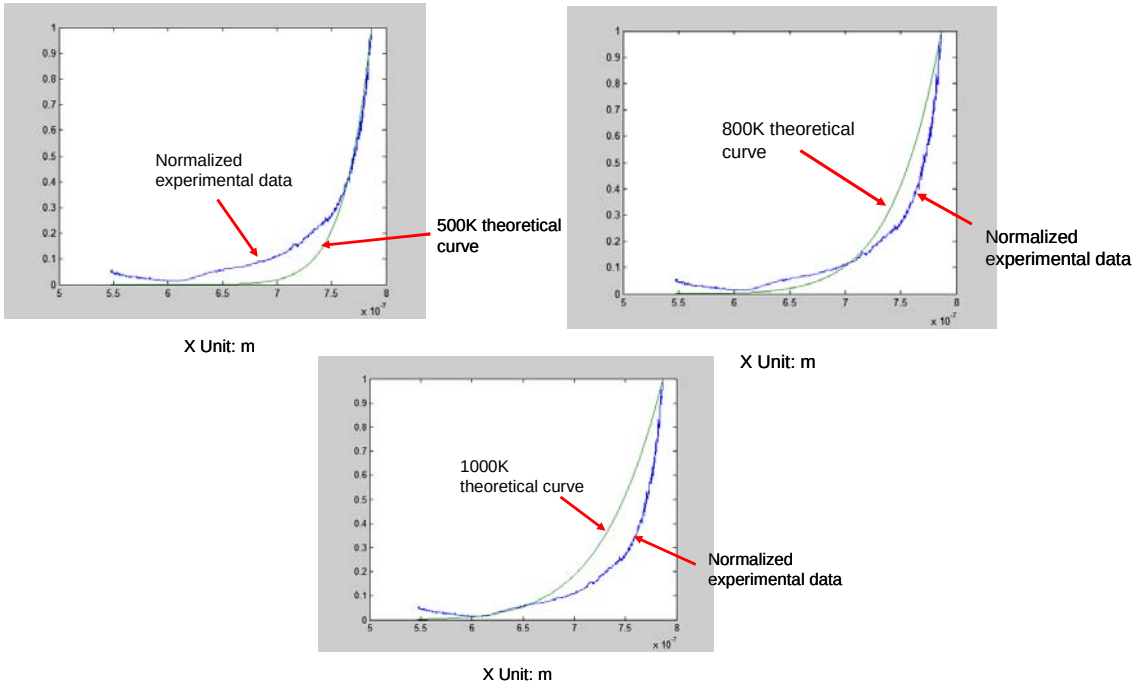

Figure 42 Temperature measurement of a laser heated AFM probe. Three fittings with T=500K, 800K and 1000K normalized theoretical curve. T=800K is the best fit.

It is difficult for this NIR pyrometer to provide accurate temperature measurement when the object temperature is low. In theory, the peak of intensity moves toward the direction of long wavelength region (refer to Figure 21). In other words, the lower the expected temperature, the weaker the radiation signal can be emitted from the object. Our NIR pyrometer has a wavelength limit (λ_{max}=940nm); therefore at some point, it is unable to sense the thermal irradiation signal. However, as long as there is enough laser power applied, this method can be used to estimate the localized temperature.

4.4.4 Laser thermal energy estimation

In order to estimate the thermal energy input from laser direct radiation, we made an assumption: if incoming laser radiation is prevented from melting the coating layer, there is no phase transformation of the coating material on an AFM probe, such that the probe has a linear response to laser radiation induced heating.

If a laser beam is continuously projected on the AFM probe, the temperature at the focused laser spot rapidly increases, such that the probe reaches an equilibrium state. At this equilibrium state, the temperature no longer changes, and the incoming heat balances the conduction loss and convection loss. Each given laser power should correspond to one equilibrium state at a specific temperature, based on our assumption. Therefore, the relationship between incoming laser power (P) and temperature (T) of the heated probe may be expressed as

$$T = \alpha P + \beta \tag{4.12}$$

where α and β are two constants.

From the experimental results, T=800K when P=12mW. Additionally, T=300K (room temperature) when P=0mW. Thus we can solve equation (4.12) as

$$T = 41.6P + 300 \tag{4.13}$$

In (4.13) the unit for T is Kelvin (K), for P is miliwatt (mW).

In principle, one can estimate the temperature with a given laser power. The temperature values of the probe with half-integer incoming power (from 4mW to 6mW) are shown in Table 6.

Table 6 The values of temperature in Fahrenheit and Celsius, corresponding to a specific given incoming laser power (from 4mW to 6mW)

P (mW)	4	4.5	5	5.5	6
T (K)	466	487	508	529	550
T (^{o}C)	193	214	235	256	277

Recall that in the optimized parameters set from section 4.1, the laser power must range from 4.5mW to 6mW, to fabricate line-like nanostructures. Based on the estimation, the localized temperature is between 214^{o}C and 277^{o}C, which seems lower than the eutectic temperature in the Au-Si system. However, additional thermal energy contribution is simultaneously provided through mechanical sliding. Both thermal energy inputs contribute to the nanoalloying process.

In this chapter, we first developed a LASPAN process matrix and provided an optimized parameters set. The line-like nanostructures can be made by using the optimized parameters combination. In the second part, we investigated the nanoscale wear mechanism and estimated the thermal energy input from pure mechanical sliding. The energy calculations showed that pure frictional heat was not sufficient to drive the interfacial reactions in an Au-Si system; laser direct radiation enhancement was therefore introduced. In the third part, we demonstrated the measurement of temperature on the AFM probe under laser direct radiation. Thermal energy input from the laser was also estimated.

Above all, we proved the feasibility of fabricating expected nanostructures by the LASPAN process. In addition, the total thermal energy required for the interfacial reactions to take place can be precisely delivered with a combination of mechanical sliding and laser radiation.

CHAPTER V

NANOCRYSTALLIZATION AND PHASE TRANSFORMATION

The LASPAN technique utilizes an atomic force microscope (AFM) as a writing tool, using an AFM probe coated by a thin gold film layer as a "nano-pen," to perform raster sliding on a single crystal silicon substrate (100). During the process, the AFM tip absorbs the laser energy and is heated to several hundred degrees (lower than the melting temperature of coating materials). Meanwhile, a certain amount of heat is generated by the friction force between the AFM tip and contacting area on the substrate. The load applied on the tip introduces stress on the gold-silicon interface. Together, the sliding and laser introduce mechanical and thermal stimulation into the highly localized region, in which eutectic reactions between the coating material and substrate are present. The energy induced nanoalloying process promotes the formation of nanostructures in the doped area. These structures can be as thin as a few atomic layers and as long as a few tens of microns.

In this chapter, fundamentals involved in the LASPAN are discussed, with a focus on nanoalloying and nanocrystallization. While extensive research has been done to investigate the nature of the fabricated nanostructures, our approach is the first of its kind with significant advantages, as mentioned earlier. In this chapter, we first proved the Au presence on Si surface in the highly localized area after writing, through Rutherford backscattering spectrometry analysis. A series of annealing experiments of gold-coated silicon samples were conducted, followed by X-ray diffraction (XRD) characterization. The used AFM probes were also examined by a field-emission

scanning electron microscope (FE-SEM). The results that showed the crystalline nanostructure can be manufactured under certain thermal energy input. More importantly, an in-situ transmission electron microscopy (TEM) characterization was conducted on the Au-Si interface through a carefully designed experiment. A stress-induced new phase of nanostructure, i.e. gold silicide ($AuSi_3$) was found to be present at the interface.

One of the most important goals of this research is to understand the fundamental principles governing the nanoalloying process. In the last part of this chapter, we review the Au-Si binary equilibrium phase diagram leading to construction of a non-equilibrium diagram of the same binary system associated with mechanical energy.

5.1 Rutherford backscattering spectrometry (RBS) analysis

A key question to be addressed in our study is whether gold (Au) atoms are transferred from the tip to the silicon (Si) substrate. By conducting Rutherford backscattering spectrometry analysis, we obtained clear evidence of Au presence on the Si surface.

RBS analysis has been extensively used for accurate determination of film composition and surface contamination of solid state targets. The technique was developed from the well-known “Rutherford scattering experiments”. The application of RBS technique in characterizing film composition is illustrated in Figure 43. Basically, ions scattered from a sample’s surface have energy characteristics of the mass of target atoms. The ratio of energy of backscattered ions to incident ions is determined by the

detecting angle, masses of target atoms and projectiles. By measuring the energy of backscattered ions, we can tell the mass of impurities presented on the substrate surfaces.

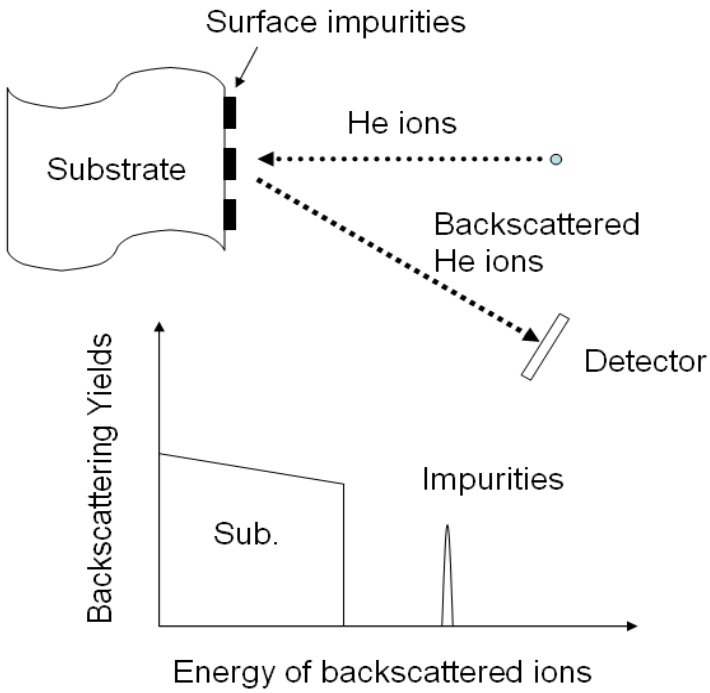

Figure 43 A schematic drawing of yield vs. energy for backscattered Helium ion from a surface engineered sample in Rutherford backscattering spectrometry (RBS) analysis

RBS quantitatively determines the amount of surface atoms. The relative number of particles backscattered from a target atom into a given solid angle for a given number of incident particles is related to the differential scattering cross section. The scattering cross section is basically proportional to the square of the atomic number of the target atom.

RBS analysis was performed by using a 2.0 MeV Helium (He) ion beam with a semiconductor detector positioned 165^{o} away from the incident beam. The detector

energy resolution was around 20 keV. The sample was a Si (100) wafer after sliding by an Au-coated Si_3N_4 probe. To maximize the Au signals in RBS spectrum, the sliding was continuously repeated on a pre-selected region. RBS analysis was limited to the marked region. The ion beam was accurately positioned by using a four axis goniometer with accuracy of 0.01^o in titling and rotation, and 0.01mm in translation. Figure 44 shows the RBS spectrum obtained. The inset shows an RBS peak observed at a channel of around 465. The peak position corresponds to the backscattering of He ions from the mass of Au atoms. Figure 44 also shows that the amount of Au detected was extremely small.

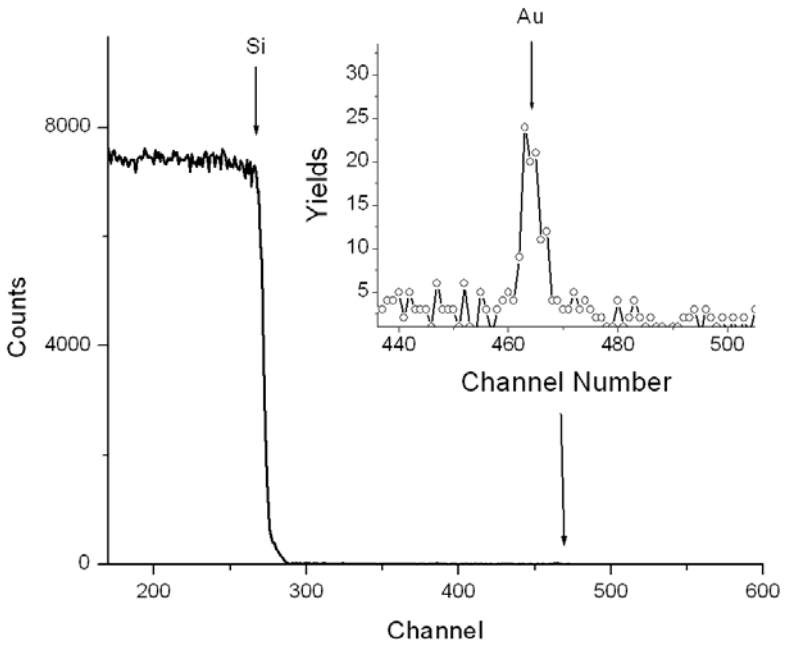

Figure 44 RBS spectrum obtained from a Si (100) surface after sliding with an Au-coated Si_3N_4 probe.

In Figure 45, we compared the RBS spectrum and RUMP simulation. The red line is a fitting curve which assumes that Au atoms have an aerial density of 2.8×10^{13} atoms/cm^2 on the Si surface.

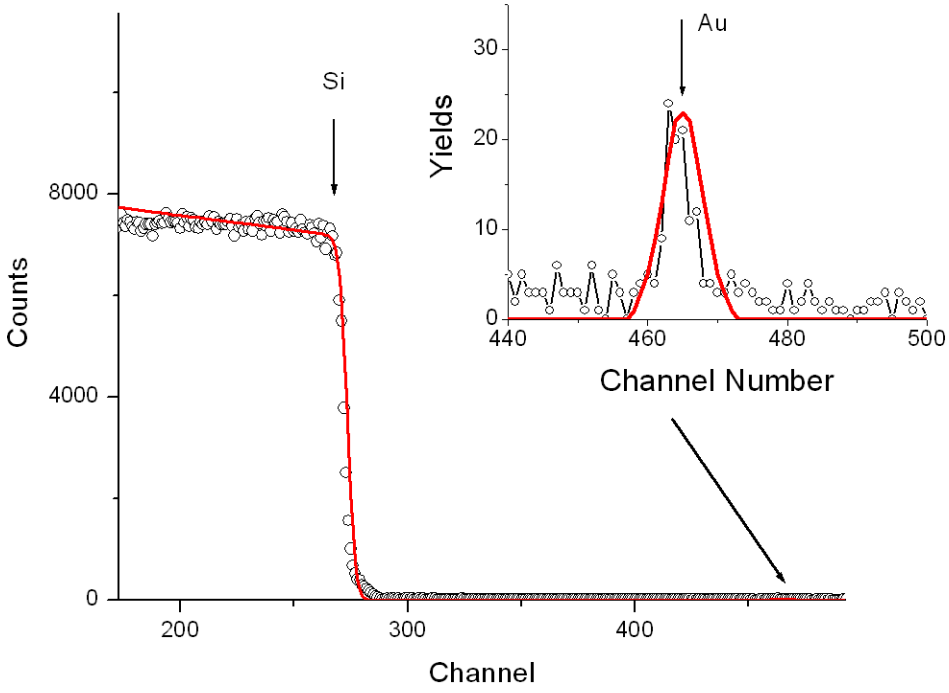

Figure 45 Comparison between RUMP simulation and RBS spectrum for a (100) Si after sliding with an Au-coated Si_3N_4 probe.

The RBS analysis provides clear evidence that Au is present on the sample surface through the LASPAN process. Therefore in the process, an interface of gold and silicon is formed in the highly localized area which is defined by AFM tip dimensions. The RUMP simulation gives the aerial density of gold atoms in the fabricated nanostructures. This can be used to estimate the concentration of gold in the Au-Si nanostructures.

5.2 Nanocrystallization in a gold-silicon system

As demonstrated in previous chapters, nanostructures can be fabricated through the LASPAN process in a highly controllable fashion. In general, thermal treatment, such as annealing, can help modify the crystal structure.

5.2.1 Annealing experiment and X-ray diffraction (XRD)

To study effects of thermal treatment on crystalline structures, we performed a series of annealing experiments on a gold-coated silicon wafer.

A single crystalline silicon wafer (100) was cut by a dicing saw into small square pieces; each with side dimensions of 1cmx1cm. A 25nm gold film was then sputtered onto the silicon surface. A standard, electrical box furnace was used to anneal the Au-coated samples. The furnace offered an ambient thermal treatment at a preset temperature (up to 1300^{o}C); the duration of treatment can be precisely controlled. Four samples were annealed at 200^{o}C, 400^{o}C, 600^{o}C, and 800^{o}C, respectively. Each sample went through a period of rapid increase in temperature and then the temperature was stabilized at the designated temperature for 30 minutes. After annealing, the samples were furnace cooled to room temperature.

A Bruker-AXS D8 advanced Bragg-Brentano X-ray powder diffractometer was used to characterize the structural properties of the gold coated substrate, before and after annealing thermal treatment. The diffractometer is equipped with a D8 goniometer, a scintillation counter with graphite monochromator and copper x-ray radiation source. Five samples (four annealed plus one as-deposited) were characterized. The scanning angle (2θ) ranged from 35 to 90 degrees, the X-ray scanning step time was 1 second, and

the step size was 0.02 degrees. The data was collected and analyzed by special software named “power XRD.”

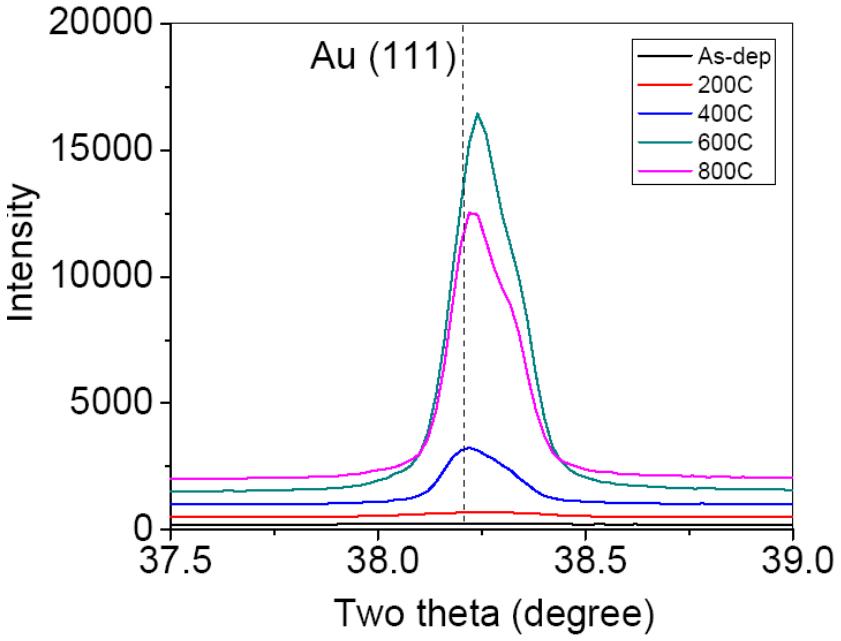

Figure 46 X-ray diffraction plot of annealed gold-coated silicon samples at different temperatures

In the plot in Figure 46, the horizontal axis is the scanning angle; the vertical axis is the intensity of the peak. The dashed line is the index of Au (111) orientation (2θ=38.2 degrees). The curve of the as-deposited sample is at the bottom, and it does not show any peak intensity at Au (111). This means that the sputter-coated Au thin film is possibly amorphous. As temperature increased, from 200^{o}C to 600^{o}C, the Au (111) peak intensity significantly increased and the peak became sharper. This means that the possible gold phase transformation and crystallization take place during annealing. The plot also

shows that the 800^{o}C annealing curve has a lower peak intensity of Au (111) than at 600^{o}C. This could be due to re-crystallization which is activated at a critical temperature between 600^{o}C and 800^{o}C. Another reason could simply be misalignment in the experiment.

As indicated above, thermal treatment is assumed to promote the generation of crystalline structure. During the LASPAN process, laser radiation and friction induced heating are the source of in-situ annealing on the fabricated nanostructures. The post–process annealing can also be accomplished with a laser or even a furnace. As such, crystalline nanostructures can be fabricated through the LASPAN process with the aid of thermal energy input.

5.2.2 FE-SEM images on probe

After the LASPAN process, Au was found present on the Si surface. Since we are also interested in finding what was happening to the AFM probes, every AFM probe was characterized using a field-emission scanning electron microscope (LEO 1530). The probe samples were mounted on a pin holder. A small amount of silver paint was applied to make a conductive path from the probe to the sample holder in order to reduce the charging effect. The accelerating voltage was 5kV; work distance was set at 10mm. The sample stage was tilted to make the viewing angle within a range from 45^{o} to 60^{o}, such that high resolution side view images were obtained. Figure 47 and Figure 48 show the morphology of different probes after the LASPAN process.

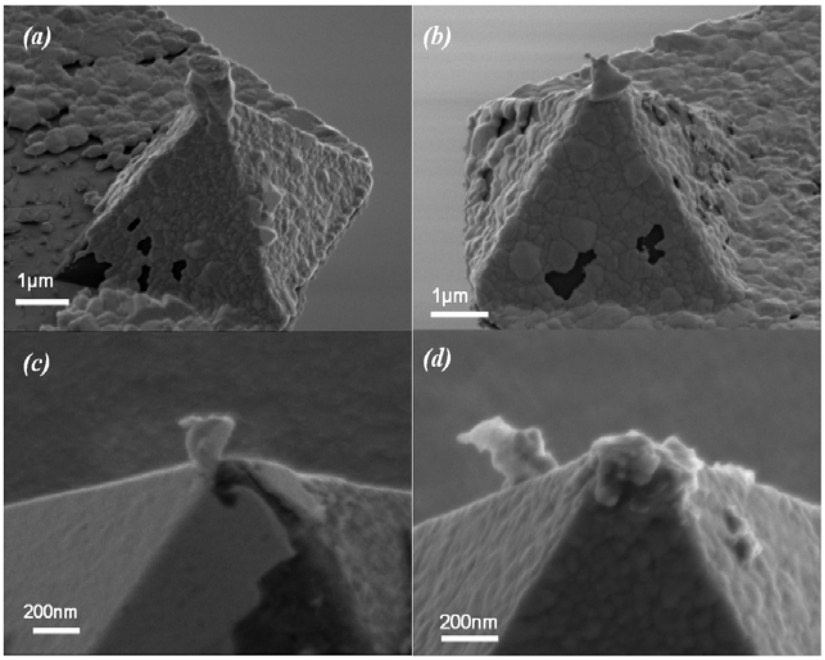

Figure 47 Side view SEM images on four different AFM probes after LASPAN writing. Materials adhesion is present in all cases.

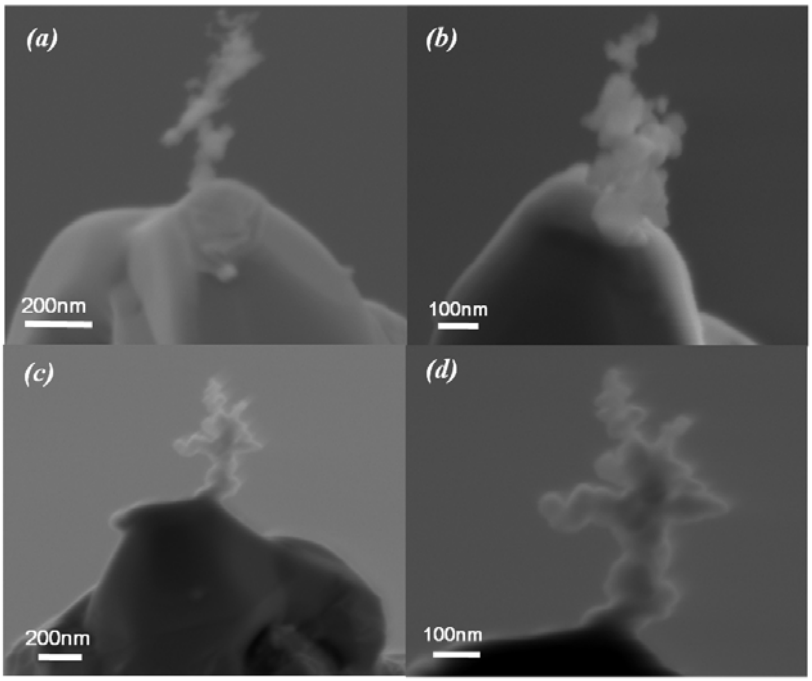

Figure 48 An AFM probe which has a growing nanostructure. (a) and (b) were taken right after LASPAN process; (c) and (d) were taken after 30 days.

Previously, abrasive wear behavior was investigated through SEM characterization on AFM probes which underwent pure mechanical sliding. Here materials adhesion was found on a number of probes after the laser-assisted writing process. Figure 47 lists four different probes on which materials were adhered. In Figure 48, an AFM probe was observed twice, with the second occurring after 30 days. The probe was observed after the LASPAN process (at P=12mW for 15 minutes). Figures 48 (a) and (b) were characterized right after the writing. An erecting structure with a dimension of less than 50nm was found at the end of the tip. More interestingly, a well-shaped tree branch nanostructure was found at the same place when the same probe was characterized again after 30 days. An energy dispersion spectroscopy (EDS) was carried out on the right side of the grown nanostructure. The EDS spectrum and elemental analysis are shown in Figure 49. Using a qualitative approach, the concentration data was derived after filtering other impurities. The main component in the nanostructure grown on the AFM tip was gold; the silicon represented only a small percentage. From equation (4.13), we can estimate the temperature on the tip under this laser power, i.e. $T=526^{o}C$. This temperature is higher than the eutectic temperature of an Au-Si system. Under pure sliding, the nanostructures at the AFM tip were neither observed on the AFM tips nor on the substrate, meaning that mechanical sliding is not sufficient to induce nanostructures. Heating is necessary to enhance the formation of nanostructures. Laser heating provides the energy needed at the localized area. This thermal energy is the driving force for the formation of nanostructures. Here the silicon acts like a catalyst to activate the change of Au, resulting in Au-Si alloying. The eutectic point of Au-Si is

much lower than the melting point of gold. When silicon is mixed with gold, it activates the localized eutectic reactions with the aid of external thermal energy introduced by laser radiation. In other words, a laser is used to ensure enough thermal energy input for nanocrystallization and phase transformation in the process to fabricate nanostructures.

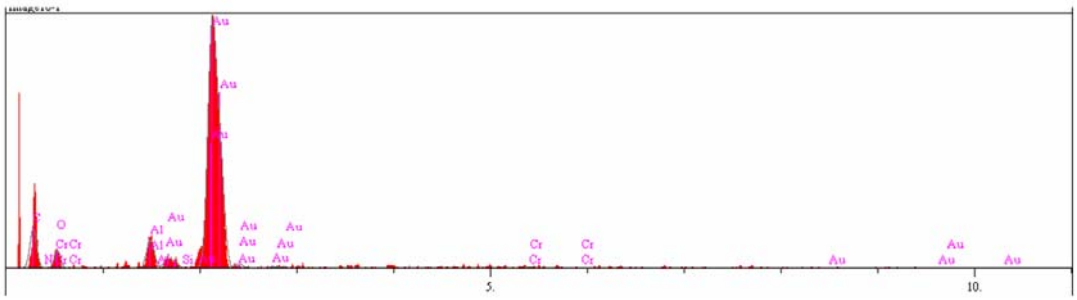

Element	Concentration (wt.%)
Si	4.6
Au	95.4

Figure 49 The EDS spectrum on nanostructure on the AFM probe and elemental analysis. It is showing that in the nanostructure, most concentration is gold.

5.3 Stress-induced nanostructured gold silicide

Now that we have proven that a laser assists in the formation of nanostrucures, the next question is how mechanical energy affects the resulting nanostructures. LASPAN is a synergetic process which involves both mechanical and thermal stimulation. An immediate question is, what is the chemical composition of the nanostructures fabricated through the LASPAN process? To answer this question, we conduct investigation on a simple eutectic binary system, i.e. the Au-Si system.

It is almost impossible to directly extract the chemical and physical information from the line-like structure on the silicon surface. The dimension of the nanostructure is extremely confined, such that the amount of the nanostructure is too small to be detected by using most state-of-the art techniques. To address this issue, a carefully designed experiment was conducted to investigate the compositional information of the fabricated nanostructures.

To understand principles behind the stress-related phase transformation, an *in situ* nanoindentation experiment was conducted inside a transmission electron microscope (TEM). It was found that, when an Au-coated nanoindenter was pressed against the silicon surface, the gold silicide ($AuSi_3$) was formed due to stress. The approach presented here precisely controls the structural and phase changes at the Au-Si interface within a highly localized area.

In this experiment, we apply mechanical forces to generate non-equilibrium states of solids, potentially as nanodevices. This is achieved using an atomic force microscopy (AFM) and an *in situ* technique, which includes a nanoindentor being incorporated inside a transmission electron microscope (TEM). We focused on the Au-Si eutectic system. A gold-coated AFM probe was used to slide against a single crystalline silicon substrate. The mechanical force was controlled through the amount of bending of the AFM cantilever. The *in situ* TEM was used to study the surface structure after indentation. This technique has been reported to study the deformation-induced grain growth during nanoindentation at room temperature.[128] An *in situ* TEM observed topotaxial evolution of a gold silicide island at the interface of crystal eutectics-silicon[129]

as well as the Au-Si diffusion interface.[130,131] In the present study, we observed the interface of Au-Si under stress.

For the *in situ* experiments, a gold film was coated on a worn nanoindenter's diamond tip. The gold thickness was about 1μm. The single crystalline silicon was processed using a focused ion beam (FIB) so that it could be observed in the TEM. The Mohr hardness of the single crystal Si was around 7.0[132] and that of gold was 2.5-3[133]. The hardness of the gold film was less than the pure gold due to porosity generated during sputtering.

In situ nanoindentation experiments in a transmission electron microscope have been used by Miner over the past few years.[134,135] A sample stage consists of a diamond indenter attached to a metal rod that was actuated by two mechanisms. For coarse positioning, the indenter could be moved in three dimensions by turning screws attached to a pivot at the end of the rod. For fine positioning, including the actual indentation, the indenter was moved in three dimensions with a piezoelectric ceramic crystal, which expanded in response to an applied voltage.

The indenter was manually loaded onto the silicon surface that was observed through the TEM. The *in situ* experiments were conducted on a single crystal silicon (100). The indenter was made of a diamond indenter (Berkovich geometry) coated with a gold film having a thickness less than 1 μm. The single crystal silicon was prepared using a focused ion beam (FIB). The basic method for FIB sample preparation is to mill out two opposing trenches on a flat piece of material, which leaves behind a thin window that is electron transparent (<~250 nm in thickness). The FIB process is meant to protect

the sample from damage caused by the incident 30-kV Ga+ ion beam. The Au-coated indenter was mounted on a piezoceramic actuator that controls the 3-D position and the applied force. During *in situ* indentation, the on-going events were observed and recorded in real time. For *in situ* TEM characterization, either a bright-field or dark-field imaging condition was used. Diffraction patterns were taken directly before and after the indentation experiments.

Nanoindentation using a gold indenter on silicon was conducted with the *in situ* TEM. Figure 50 (a) is the image taken right before indentation. In this figure, the indent is shown in the top right area and the bottom left is the surface of the single crystalline silicon. Fringes indicate the thickness of the silicon. The X-Ray diffraction pattern of silicon is shown in Figure 50 (b) where the crystal planes are labeled. Figures 51 (a) and (b) are TEM micrographs after indentation for the Au tip and Si surface respectively. X-ray diffraction results (of Si) are shown in Figures 52 (a)-(c). Figure 52 (a) shows the analyzed area. Figure 52 (b) shows the rings and dots of the diffraction patterns. Figure 52 (c) shows identified patterns, marked as $AuSi_3$. The *in situ* TEM results of the complete indentation process were extracted as several images at different time points, as shown in Figure 53. Results show that before and after indentation, there were changes in diffraction patterns. Before indentation, the Si surface was single crystal. After indentation, a phase with the composition of $AuSi_3$ was identified.

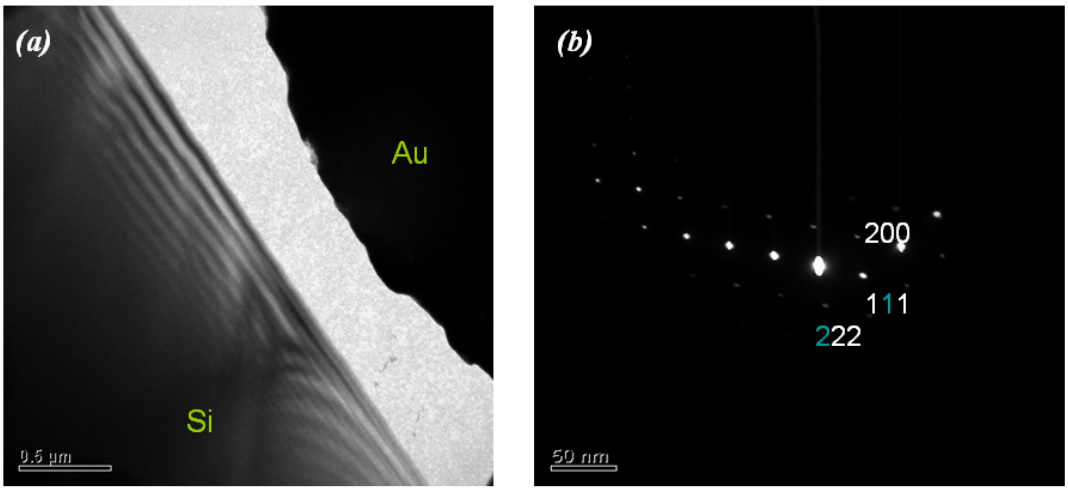

Figure 50 TEM images before indentation. (a) before indentation; (b) X-Ray diffraction pattern of pure single crystal Si where the crystal planes are labeled with 200, 111, and 222 planes.

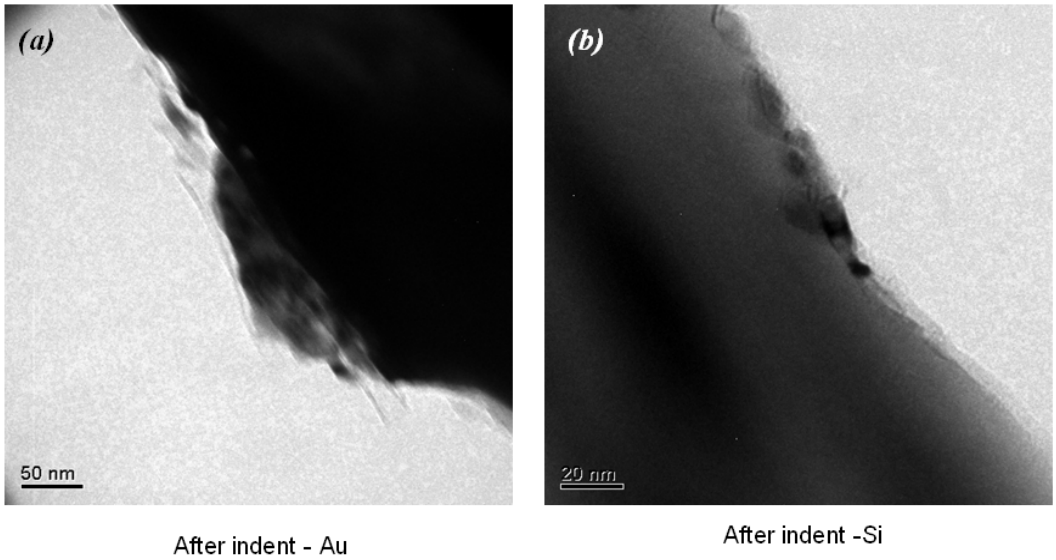

Figure 51 TEM images after indentation. (a) Image of Au after indentation; (b) Si after indentation.

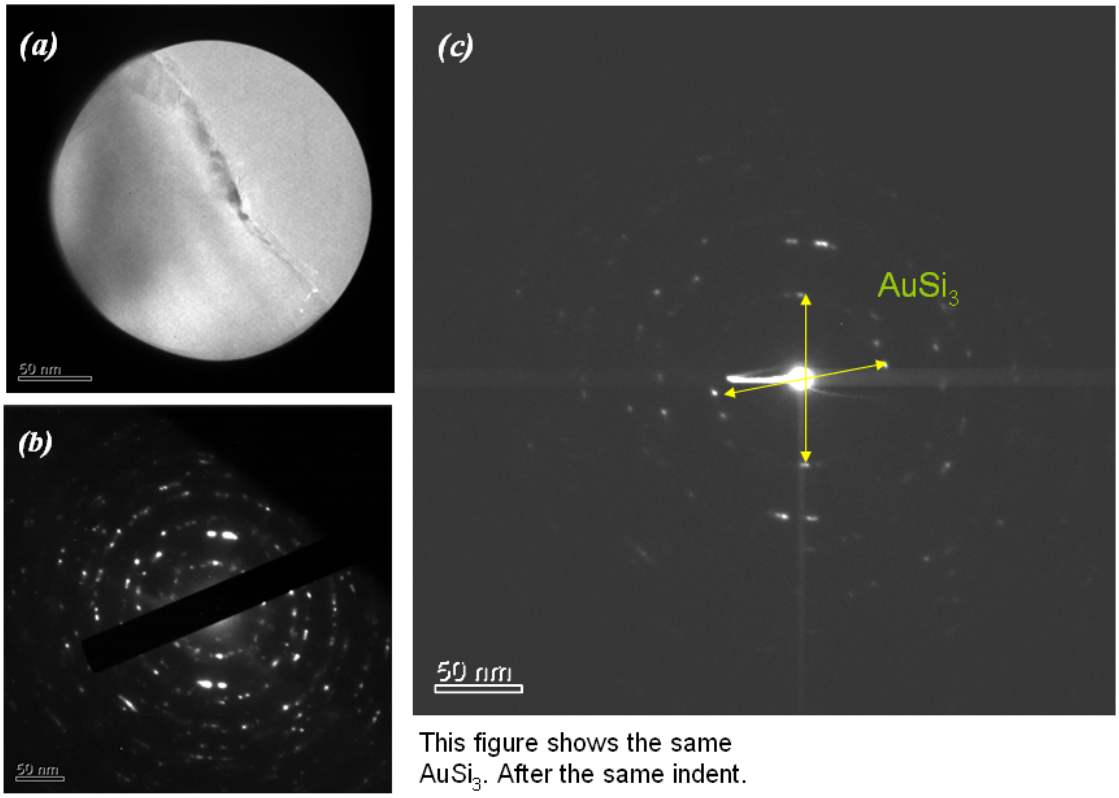

Figure 52 In-situ TEM results. (a) Area on the Si for TEM and X-ray diffraction analysis; (b) the X-Ray pattern showing rings and dots through diffraction; (c) shows the identified patterns, marked as AuSi3.

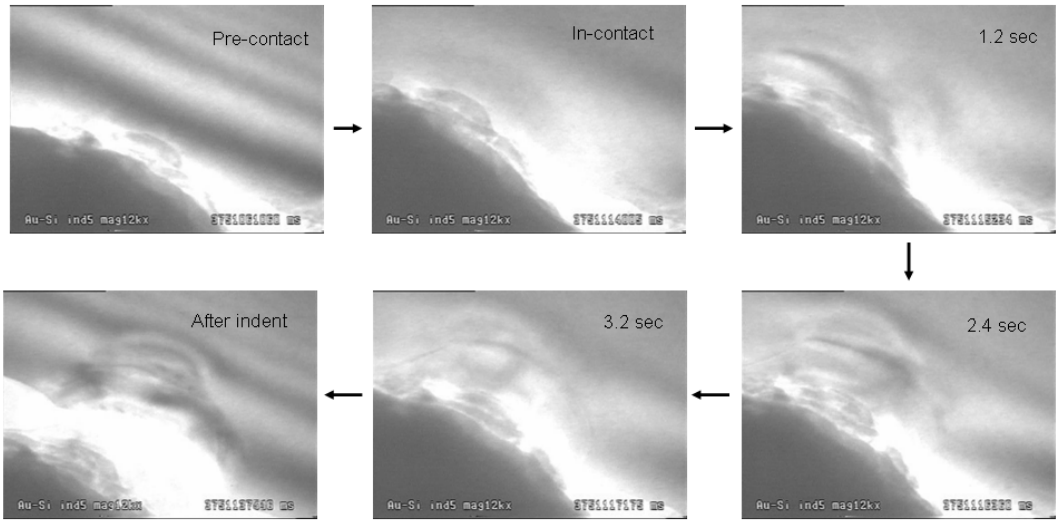

Figure 53 In-situ TEM screen shot of Au-Si indentation process at different time point.

Although the hardness of the gold is less than that of silicon (i.e., 2.5-3 Mohr), while the Mohr hardness of Si is 7.0, the soft gold did indeed penetrate into the silicon surface with an indent of approximately 50 nm in depth (Figure 51 b). Comparing the tip before and after indentation, the Au indenter was larger than the indent on Si. In the same figure, the dark colored Si edge inside an indent shows a visible amount of Au. The adhesion of Au onto Si was earlier observed after the AFM sliding experiments. Our results show that the indentation wear involves simultaneous adhesion and fracture at the Au-Si interface. The soft Au wears through abrasion, and the hard Si deforms and fractures simultaneously.

The Au and Si can be adhered together based on three possibilities: forming primary bonding, creating mechanical locking through surface roughness, or making a new alloy. The Au and Si are soluble between each other at low temperatures (with a

high diffusion rate of Si into Au). In this situation there is no clear interface to be formed. In the present work, our TEM image shows that the surface roughness is not high enough to form mechanical locking. The adhesion mechanism between Au and Si is believed to be the stress-induced junction. The bond was promoted by the formation of $AuSi_3$ and was proven in Figures 50-51.

The effects of mechanical forces on material properties and surfaces within a small length scale have been reported using an AFM in both nanomachining[100,136-138] and sliding modes.[139,140] In the nanomachining mode, the AFM removes atoms from the surface through fatigue wear.[141,142] This type of interaction is based on Hertz contact, in which the maximum shear stress occurs below the surface. Under sufficient load, the sample will plastically deform, bonds will break, and material will be removed.[143] In sliding, small islands of material on a surface are stimulated beneath the AFM tip. Unique surface phenomena such as dissolution, regrowth, and material movement along lattice direction have been reported.[144-147] In the present work, when a soft Au indenter pressed a hard Si surface, we observed the stress-induced adhesion. Through sliding, small structures were formed.

It was mentioned earlier that chemical interactions are possible due to indentation stress. Our results showed that the driving mechanical force through indentation introduced two types of damages: formation of an indent and/or new phases. The new phase, $AuSi_3$, was observed to be associated with adhesion, where the material was transferred to the counterpart material (Figures 50-51). In our earlier study in dry sliding, it was shown that the frictional heating could increase the temperature to a few hundred

degrees.[82] The external thermal energy through friction apparently is sufficient to form an adhesion through $AuSi_3$ as a bonding layer.

In summary, using an *in situ* nanoindentation approach, we forced a soft Au-coated indenter against a hard Si substrate. We found that stress induces the formation of gold silicide having the composition of $AuSi_3$. This bond promotes the formation of unique and small structures. The stress-induced formation of the non-equilibrium state of $AuSi_3$ does not appear in the equilibrium Au-Si system. Techniques used here precisely control the structural change at the interface within a highly localized area. In addition to the benefit of formation of small features, we observed the stress-related non-equilibrium process that might be common at the nanometer length scale.

5.4 Non-equilibrium phase diagram of Au-Si

The LASPAN process has been fully developed, and nanostructures can be fabricated through exercised parameter sets. Especially in the Au-Si system, we practically applied the LASPAN technique to generate line-like nanostructures. The eutectic system was selected as a model system for this study in order to observe the effects of force and temperature on such a reaction.

In the equilibrium Au-Si system, gold and silicon undergo eutectic reactions at $363^{o}C$, i.e., eutectic temperature. At the eutectic temperature, three phases are in equilibrium: liquid, Au and Si phases.

In the present research, we discovered three facts: (i) gold and silicon can be mechanically forced to form an interface within the highly localized area. Both materials

have inter-diffusion during the LASPAN process; (ii) a non-equilibrium phase of gold silicide ($AuSi_3$) is generated at the Au-Si interface under stress; (iii) thermal energy input helps to form crystalline structures. The non–equilibrium phase $AuSi_3$ can be presented at the line-like nanostructures fabricated by the LASPAN process, along with others. These metastable phases can be diagramed into a non-equilibrium one as guidance for phase and energy consideration. Such a diagram is important particularly for nanostructured materials.

In this section, the establishment of the equilibrium Au-Si phase diagram is first reviewed. The non-equilibrium Au-Si phase diagram is further developed, based on the equilibrium one.

5.4.1. Review of equilibrium Au-Si phase diagram

A sketch of the equilibrium phase diagram of the binary system Au-Si is shown in Figure 54. The horizontal axis is the concentration of gold with weight%, the vertical axis is temperature.

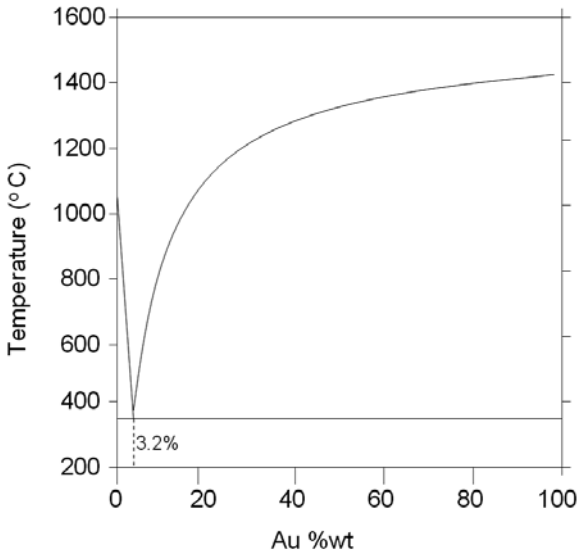

Figure 54 Equilibrium phase diagram of Au-Si.

This phase diagram shows coexistent phases in equilibrium. The general condition for equilibrium in a heterogeneous closed system (assume at constant pressure) at constant temperature can be expressed in terms of the chemical potential of the components of the phases in equilibrium:

$$\mu_j^{\alpha} = \mu_j^{\beta} = \ldots \tag{5.1}$$

where α, β… denotes different phases, and *j* denotes the different components (j is an integer) of the system. In the binary system of gold and silicon, the condition yields to

$$\mu_{Au}^{\alpha}(x_{Au}^{\alpha}) = \mu_{Au}^{\beta}(x_{Au}^{\beta}) \tag{5.2}$$

$$\mu_{Si}^{\alpha}(x_{Au}^{\alpha}) = \mu_{Si}^{\beta}(x_{Au}^{\beta}) \tag{5.3}$$

$$x_{Au}^{j} + x_{Si}^{j} = 1 \tag{5.4}$$

where x_{Au}^{α} and x_{Au}^{β} are the mole fractions of Au in the phases α and β (same for x_{Si}^{α} and x_{Si}^{β}) at equilibrium.

The equations (5.2) and (5.3) must be solved simultaneously to determine the compositions of the two phases at coexistence. The general approach is to solve the equations graphically.

The chemical potentials of gold and silicon can be rewritten as

$$\mu_{Au} = G + (1 - x_{Au})\frac{dG}{dx_{Au}} \tag{5.5}$$

$$\mu_{Si} = G - x_{Au}\frac{dG}{dx_{Au}} \tag{5.6}$$

where G is the Gibbs energy of the given solution at a particular composition x_{Au}. Hence the equilibrium conditions can now be derived graphically from Gibbs energy versus composition curves by the common tangent construction.

The Au-Si binary system is a simple eutectic system; the establishment of its equilibrium phase diagram is shown in Figure 55. All the plots are schematic, units are not to scale.

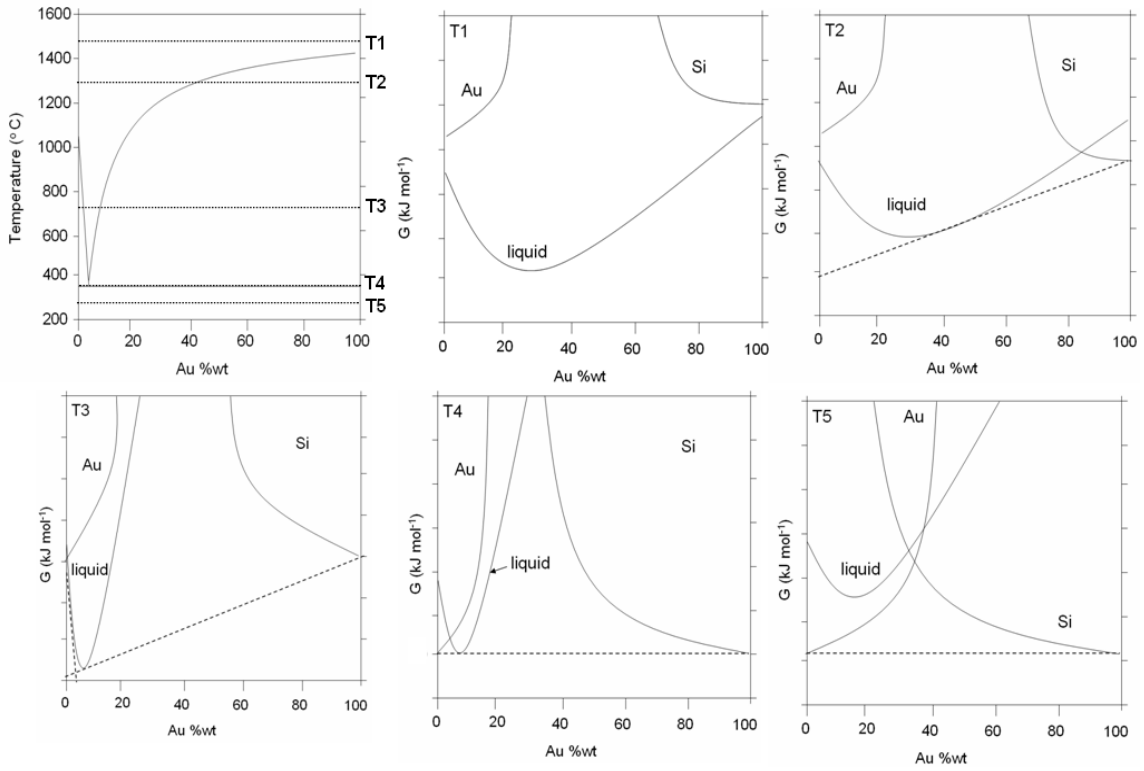

Figure 55 Establishment of Au-Si equilibrium phase diagram

There are five different temperatures (from T1 to T5, decreasing) in the sketches. In the equilibrium Au-Si phase diagram, the five horizontal bars denote these five temperatures. At temperature T1, which is higher than both melting points of gold and silicon, the Gibbs energy curve has the lowest value in the liquid phase of both materials, at any compositions. At temperature T2, which is lower than the melting point of silicon, but higher than that of gold, the liquid phase and solid phase of silicon coexist; the tangent line (dashed line in the third sketch) determines the composition of Au/Si of the equilibrium state at this temperature. At temperature T3, there are two compositions of Au/Si in the equilibrium state. The first composition (on the left) denotes the coexistence

of gold solid and liquid; the second composition (on the right) denotes the coexistence of silicon solid and liquid. Between the two compositions, the liquid phase is stable. At temperature T4, which is the eutectic point, the three phases are in equilibrium; the eutectic reaction can be expressed as

$$Liquid \rightleftharpoons Au(solid) + Si(solid) \tag{5.7}$$

At temperature T5, which is lower than the eutectic temperature, a sample in equilibrium consists of the crystalline phase of gold, silicon or a two phase mixture.

The equilibrium Au-Si phase diagram is established from Gibbs versus Au wt. % curves at each temperature, followed by the procedure described above.

5.4.2. Non-equilibrium phases of the Au-Si system

The equilibrium Au-Si phase diagram is dominated by temperature, i.e. thermal energy. In our LASPAN process, thermal energy was introduced from both laser radiation and sliding friction. As we estimated earlier, mechanical sliding contributes to the total energy input. A non-equilibrium phase, gold silicide ($AuSi_3$) was presented at the Au-Si interface as the stress-induced product.

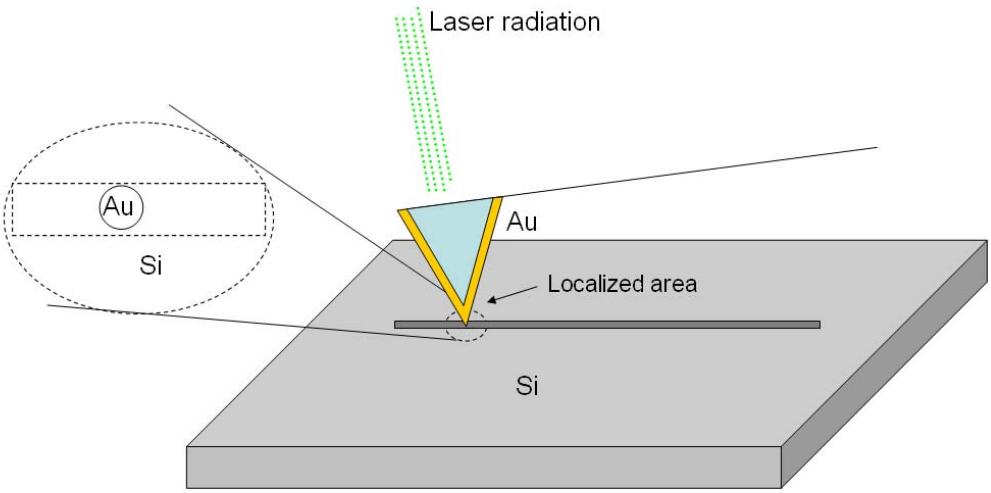

Figure 56 A sketch showing Au-Si interface in the LASPAN process

When the gold-coated AFM probe is brought into contact with the silicon surface, the Au-Si interface is formed. The highly localized region is indeed silicon rich (as shown in Figure 56). At this point, let us assume we introduce only thermal energy (through laser radiation). Diffusion could lead to the eutectic reaction. At the eutectic temperature, the eutectic concentration is 3.2%wt, as shown in Figure 54. However, in the LASPAN process, mechanical load is applied. The mechanical force (friction) rubs the surface atoms of both Au and Si, promoting the diffusion process. This process promotes the disorderliness of surface atoms leading to under melting (before reaching the eutectic temperature). As such, a non-equilibrium eutectic could be introduced that

was already proven in our experimental results. Detailed discussions will be conducted in the following.

The amount of mechanical energy can be denoted as E_{Mech}. According to the Gibbs energy discussed earlier, the existence of mechanical energy can be added to form the following equations,

$$\mu_{Au} = G^{'} + (1 - x_{Au}) \frac{dG^{'}}{dx_{Au}} \tag{5.8}$$

$$\mu_{Si} = G^{'} - x_{Au} \frac{dG^{'}}{dx_{Au}} \tag{5.9}$$

where $$G^{'} = G + E_{Mech} \tag{5.10}$$

The addition of mechanical energy promotes the further reduced eutectic temperature, as illustrated in Figure 57. The dashed lines represent the liquidous line as modified by mechanical force. As mentioned above, the new liquidous line is lower than the original one from the equilibrium state. The indexed vertical dashed line represents a new stoichiometric phase—$AuSi_3$, which is a non-equilibrium phase, appears at its composition (~30%), and has higher Gibbs energy than the equilibrium ones (see Figure 58). The horizontal dashed line represents a modified eutectic point (<363^{o}C). Hence the non-equilibrium eutectic reaction can be expressed as

$$Liquid \rightarrow Au(solid) + AuSi_3(solid) \tag{5.11}$$

In the right region of $AuSi_3$, other non-equilibrium phases may exist. Further investigations are needed for the plot, which is beyond the scope of this research because we focus on eutectic reactions.

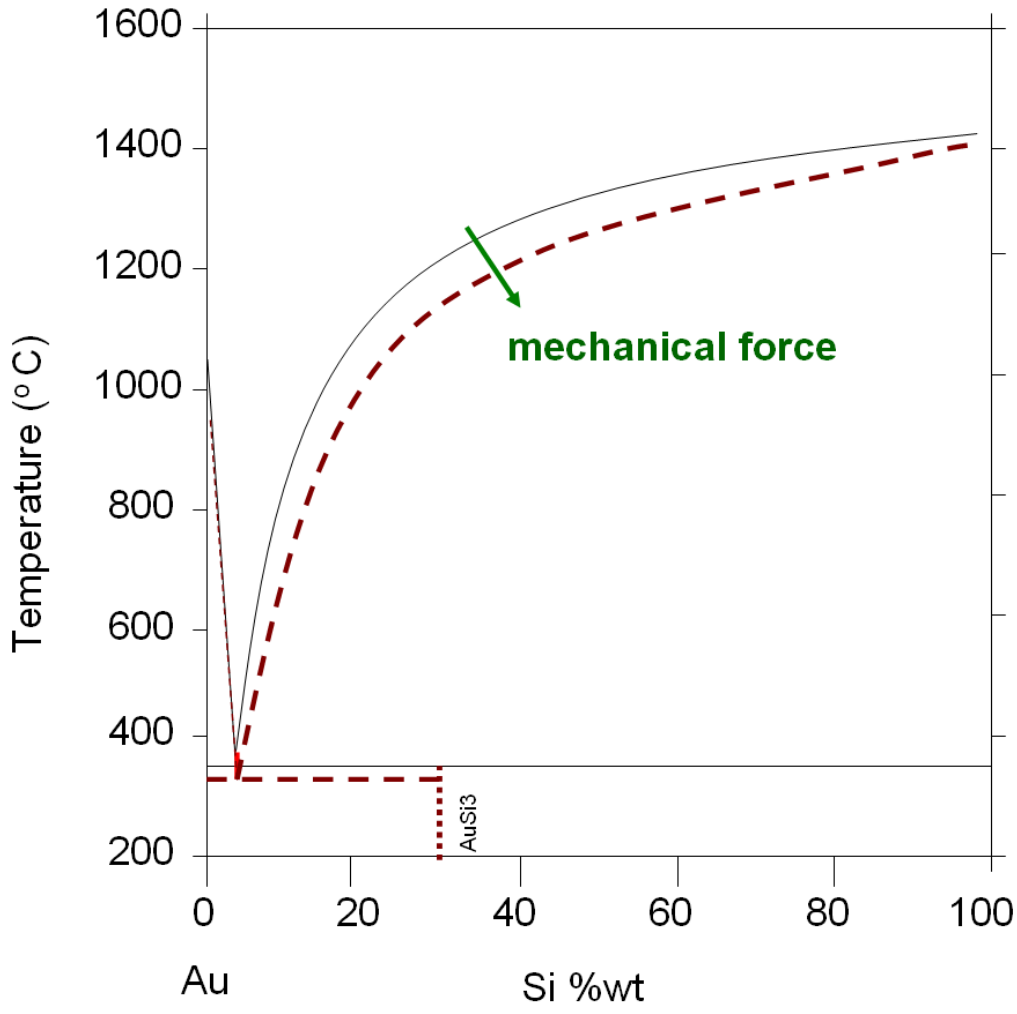

Figure 57 Non-equilibrium phase diagram of Au-Si.

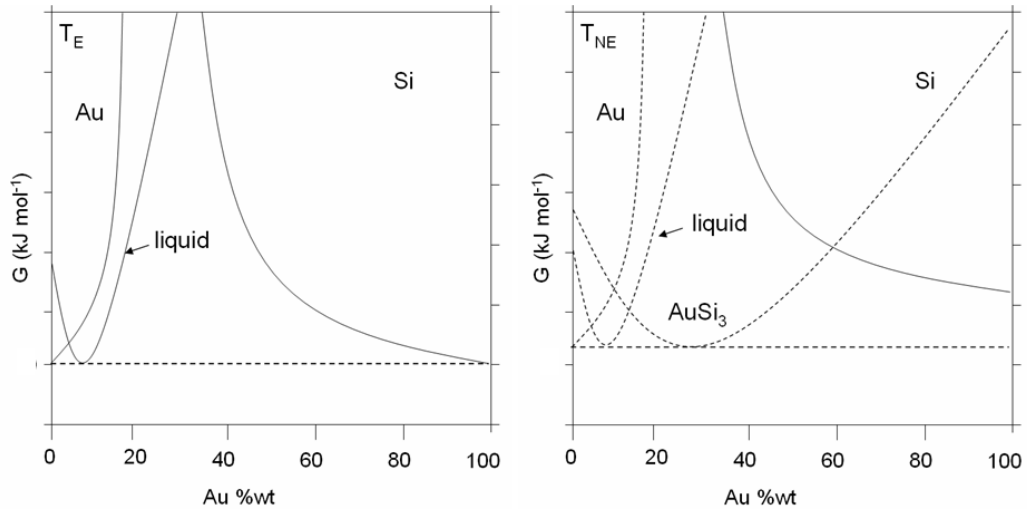

Figure 58 Sketches of Au-Si phase diagram. Left: equilibrium phase diagram at T_E=363^{O}C; Right: non-equilibrium phase diagram at T_{NE}<T_E

We have demonstrated the establishment of a non-equilibrium Au-Si phase diagram based on our experimental findings. The mechanism of the LASPAN process and structure of fabricated nanostructures can be understood from this new diagram. On the other hand, the LASPAN is a unique process to combine both mechanical sliding and direct thermal energy input to study the binary material system. Non-equilibrium phases can be explored and studied.

5.4.3 (Nano-)energy model

We employed an Au-Si system, a simple eutectic system, to study the LASPAN process. Mechanical sliding was introduced to form interface (stress) and shear materials off (sliding friction); the laser radiation provided sufficient thermal energy input for the chemical reactions taking place, and generated nanostructures. Experimentally, we

observed the presence of non-equilibrium phases, which are not the most stable phases, thus more energy is required to drive the formation. In this section, we demonstrate the energy comparison for the whole process and develop a generalized model for LASPAN. The nanostructure formation or, in other words, the non-equilibrium phase presence, is indeed a chemical reaction. Hence specific activation energy is associated with the reaction. To investigate the activation energy for an Au-Si system, we performed lateral force microscopy (LFM) measurement using the same AFM. A contact mode silicon probe was used to scan an Au coated substrate. The output signal was recorded as $V_{L\text{-}R}$ in the unit of milivolts (mV). Two sets of scanning were carried out at room temperature (T_1=293K) and another higher temperature (T_2=323K), respectively. The experimental data can be found in Table 7. The analysis will be further discussed below.

Table 7 Lateral force microscopy (LFM) data on Au coated substrate at two different temperatures. $V_{L\text{-}R}$ is the voltage readout from AFM, it has the unit of milivolt (mV). (Note: this value is the average of all points within scanning area) T_1 and T_2 are two different temperatures at which LFM measurements were performed

	$V_{L-R}^{Au}(mV)$
T_1(293K)	139 ± 18
T_2(323K)	554 ± 22

Recall Arrhenius equation:

$$k = Ae^{-E_a / RT} \tag{5.12}$$

where k is chemical reaction rate, A pre-factor, $R = 8.31 \text{J}\cdot\text{K}^{-1}\cdot\text{mol}^{-1}$ gas constant.

During sliding, the value of $V_{L\text{-}R}$ directly reflects the amount of frictional force, thus it is proportional to the thermal energy generated, which is related to the chemical reaction rate. Therefore, we construct the relationship between $V_{L\text{-}R}$ and k as

$$V_{L-R} \propto k \tag{5.13}$$

With two different temperatures and normalization, equation (5.5) can be rewritten as

$$\frac{V_{L-R}(T_1)}{V_{L-R}(T_2)} = \frac{k(T_1)}{k(T_2)} = \exp[-(\frac{E_a}{RT_1} - \frac{E_a}{RT_2})] \tag{5.14}$$

Solving (5.6), we get

$$E_a = \frac{RT_1T_2}{T_1 - T_2} \ln \frac{V_{L-R}(T_1)}{V_{L-R}(T_2)} \tag{5.15}$$

Plugging in all the numbers into (5.15), we calculate the activation energy (using data from Table 7) for Au-Si system as E_a(Au-Si)=3.63×10^4 Jmol^{-1}. Since 1mole=6.02×10^{23} molecules, we express the activation energy as E_a (Au-Si)=0.38eV/molecule. The activation energy calculated here is correlated to void formation and diffusion and is less than the nucleation of cracks and dislocations. We define this energy being the minimum energy required to form the non-equilibrium phase. Therefore, we give an energy model for the LASPAN process as

$$E_a(Au - Si) \cdot V \cdot D_{Mole} \le E_{Mech} + E_{La} \tag{5.16}$$

In (6.16), $E_a(Au\text{-}Si)$ denotes the activation energy, V denotes the volume of designated nanostructure, D_{Mole} denotes the atomic density of nanostructure (for most solid phase, the value is 1x10^{23}/cm^3, WLOG). E_{Mech} and E_{La} were effective mechanical energy input and laser radiation energy input, defined in Chapter V. This model

represents the whole LASPAN process. It can be used to predict the amount of energy delivered to overcome the activation energy of eutectic reactions. Thus, designated nanostructures can be fabricated. On the other hand, we can use this model to help optimize experimental parameters.

Now we use our Au-Si system to explain how the energy model works. Assume we need to fabricate a 50μm long, 50nm wide, and 5nm thick line-like nanostructure. The volume of this structure is $1.25\text{x}10^{7}\text{nm}^{3}$, with the given value of activation energy and atomic density, and we can calculate the left hand side of equation (5.16) as $3\text{x}10^{-11}$J. The friction energy can be estimated following the same approach discussed in Chapter IV (section 4.3.5). By considering the heat loss through conduction and convection, the effective frictional energy is a small amount, 1% of E_f is a reasonable estimate, hence E_{Mech} is about $1.9\text{x}10^{-11}$J. According to (5.16), in order to overcome the total energy needed, we require E_{La} to be at least $1.1\text{x}10^{-11}$J. Based on the nature of the LASPAN process, it is more useful to calculate the temperature (due to laser radiation) of the system. Thus we can use the following equation to estimate T,

$$E_{La} \simeq \Delta Q = m \cdot c_p \cdot \Delta T = \rho \cdot V \cdot c_p \cdot \Delta T \qquad (5.17)$$

where ΔQ is the heat change, m is the mass of material, c_p is the specific heat capacity, ΔT is the temperature change, ρ is material density and V is the volume of material. By using the values for gold, we calculate ΔT as 355K. This means the laser radiation needs to raise the temperature to 628K (which corresponds to the power of 8mW). Note that the laser radiation focused area is larger than the area of the designated nanostructure, therefore in reality; the applied laser power could induce more than enough thermal

energy. In other words, the effective laser power needed could be less than the model predicts.

The energy model fits our Au-Si system in comparison to all experimental results. It is also an effective model to optimize all the experimental parameters. Furthermore, this energy model can be generalized as

$$E_a(A-B)\cdot V\cdot D_{Mole} \le E_{Mech} + E_{La} \tag{5.18}$$

where $E_a(A\text{-}B)$ denotes the activation energy in a generalized materials system A-B. The energy contribution from mechanical sliding and laser radiation can be estimated by using the specific value in system A-B. The experimental parameters can also be exercised and predicted from this generalized energy model, by following the approach described in the Au-Si system.

In this chapter, we have extensively investigated nanostructure fabrication through the LASPAN process. We established a non-equilibrium phase diagram of an Au-Si system to represent the new phase $AuSi_3$ found experimentally. Furthermore, energy analysis of the process was demonstrated, and a nano-energy model to represent the LASPAN process was also provided.

CHAPTER VI

CONCLUSIONS AND FUTURE RECOMMENDATIONS

6.1 Conclusions

This research is focused on a novel nanofabrication process, i.e. laser-assisted scanning probe alloying nanolithography (LASPAN). We designed and developed the laboratory setup in combinations of an existing atomic force microscope (AFM) and an external laser optical system. The LASPAN process is then exercised and optimized in a simple eutectic binary system, i.e. gold-silicon (Au-Si) system. Four aspects of nanostructures were produced through LASPAN process. Among them, a designated line-like nanostructure was fabricated under optimized condition. Morphological and structural characterizations have been done on the line-like nanostructure to investigate its physical and chemical properties. A new phase ($AuSi_3$) was discovered. Then a non-equilibrium phase diagram of Au-Si system was established to explain the presence of new phase. Mechanical sliding and laser radiation contribute to the fabrication simultaneously. It was found that well-defined nanostructure can be made with the aid of laser radiation. Detailed energy analysis and dissipation was conducted. The contribution from each side was calculated. Based on all results, we finally derive an energy model to represent the LASPAN process. This energy model is generalized and can be used to give guidance to optimize experimental parameters in any pre-selected materials system, such that a designated nanostructure can be fabricated.

In this study, we employed a novel approach to fabricate new nanostuctures with minimized dimensions, this process opened new areas of fundamental research in surface and materials science, especially nanoalloying and nanocrystallization. Potentially, the technique developed in this work can generate new ways to make nanodevices.

6.2 Future recommendations

1. Investigate new means to directly characterize the fabricated nanostructure, e.g. use high-resolution TEM to find out the structure information at atomic level
2. Investigate the electronic and optical properties of the fabricated nanostructures, which will be useful to create nanodevices
3. Modify our temperature measurement and employ thermal energy simulations to give more accurate energy analysis
4. Probe sharpening process will be expected, since it is directly related to the dimension of nanostructure

REFERENCES

[1] Richard P. Feynman, Speech at California Institute of Technology (1959).

[2] M. A. Reed, J. N. Randall, R. J. Aggarwal, R. J. Matyi, T. M. Moore, and A. E. Wetsel, Phys Rev Lett. **60**, 535 (1988).

[3] R. S. Wagner and W. C. Ellis, Appl Phys Lett. **4**, 89 (1964).

[4] D. P. Yu, Z. G. Bai, Y. Ding, Q. L. Hang, H. Z. Zhang, J. J. Wang, Y. H. Zou, W. Qian, G. C. Xiong, H. T. Zhou, and S. Q. Feng, Appl Phys Lett. **72**, 3458 (1998).

[5] A. M. Morales and C. M. Lieber, Science. **279**, 208 (1998).

[6] Y. F. Zhang, Y. H. Tang, N. Wang, D. P. Yu, C. S. Lee, I. Bello, and S. T. Lee, Appl Phys Lett. **72**, 1835 (1998).

[7] Z. W. Pan, Z. R. Dai, and Z. L. Wang, Science. **291**, 1947 (2001).

[8] X. Wu, R. Sharman, J. Mei, and W. Voice, Materials & Design. **23**, 239 (2002).

[9] Y. F. Chan, X. F. Duan, S. K. Chan, I. K. Sou, X. X. Zhang, and N. Wang, Appl Phys Lett. **83**, 2665 (2003).

[10] L. Schubert, P. Werner, N. D. Zakharov, G. Gerth, F. M. Kolb, L. Long, U. Gosele, and T. Y. Tan, Appl Phys Lett. **84**, 4968 (2004).

[11] A. A. Tseng, A. Notargiacomo, and T. P. Chen, J Vac Sci Technol B. **23**, 877 (2005).

[12] A. A. Seraphin, E. Werwa, and K. D. Kolenbrander, Journal of Materials Research. **12**, 3386 (1997).

[13] H. F. Zhu, S. F. Ai, Q. He, Y. Cui, and J. B. Li, Journal of Nanoscience and Nanotechnology. **7**, 2361 (2007).

[14] P. P. Bose, M. G. B. Drew, A. K. Das, and A. Banerjee, Chemical Communications. **30**, 3196 (2006).

[15] P. Prete, N. Lovergine, and L. Tapfer, Applied Physics A-Materials Science & Processing. **88**, 21 (2007).

[16] W. M. Moreau, *Semiconductor Lithography: Principles and Materials*. (Plenum, New York, 1988).

[17] H. J. Levinson, *Principles of Lithography*, Second ed. (SPIE Press, Bellingham 2005).

[18] K. Suzuki, *Sub-Half-Micron Lithography for VLSIs*. (Cambridge University Press, New York, 2005).

[19] Z. Cui, *Micro-Nanofabrication, Technologies and Applications*. (Springer, Beijing, 2005).

[20] A. A. Guzelian, J. E. B. Katari, A. V. Kadavanich, U. Banin, K. Hamad, E. Juban, A. P. Alivisatos, R. H. Wolters, C. C. Arnold, and J. R. Heath, J Phys Chem-Us. **100**, 7212 (1996).

[21] Z. L. Wang, P. Poncharal, and W. A. de Heer, J Phys Chem Solids. **61**, 1025 (2000).

[22] G. Binnig, H. Rohrer, C. Gerber, and E. Weibel, Phys Rev Lett. **50**, 120 (1983).

[23] H. P. Lang, M. Hegner, E. Meyer, and C. Gerber, Nanotechnology. **13**, R29 (2002).

[24] Philip B Meggs, *A History of Graphic Design*. (John Wiley & Sons, Inc., New York, 1998).

[25] M. M. J., *Fundamentals of Microfabrication*, 2nd ed. (CRC Press, Boca Raton, Florida, 2002).

[26] J. R. Maldonado, J Electron Mater. **19**, 699 (1990).

[27] L. A. Giannuzzi and F. A. Stevie, *Introduction to Focused Ion Beams: Instrumentation, Theory, Techniques and Practice*. (Springer, New York, 2005).

[28] J. I. Pascual, J. Mendez, J. Gomezherrero, A. M. Baro, N. Garcia, and V. T. Binh, Physical Review Letters. **71**, 1852 (1993).

[29] N. M. Miskovsky and T. T. Tsong, Physical Review B. **46**, 2640 (1992).

[30] G. S. Hsiao, R. M. Penner, and J. Kingsley, Applied Physics Letters. **64**, 1350 (1994).

[31] D. H. Huang, T. Nakayama, and M. Aono, Applied Physics Letters. **73**, 3360 (1998).

[32] A. Laracuente, M. J. Bronikowski, and A. Gallagher, Applied Surface Science. **107**, 11 (1996).

[33] H. Kawata, I. Matsumura, H. Yoshida, and K. Murata, Jpn J Appl Phys 1. **31**, 4174 (1992).

[34] R. D. Allen, P. J. Brock, L. Sundberg, C. E. Larson, G. M. Wallraff, W. D. Hinsberg, J. Meute, T. Shimokawa, T. Chiba, and M. Slezak, Journal of Photopolymer Science and Technology. **18**, 615 (2005).

[35] R. L. Brainard, G. G. Barclay, E. H. Anderson, and L. E. Ocola, Microelectronic Engineering. **61-2**, 707 (2002).

[36] B. Fay, Microelectronic Engineering. **61-2**, 11 (2002).

[37] Y. Hirai, Y. Kanemaki, K. Murata, and Y. Tanaka, Jpn J Appl Phys 1. **38**, 7272 (1999).

[38] P. Ruchhoeft, M. Colburn, B. Choi, H. Nounu, S. Johnson, T. Bailey, S. Damle, M. Stewart, J. Ekerdt, S. V. Sreenivasan, J. C. Wolfe, and C. G. Willson, J Vac Sci Technol B. **17**, 2965 (1999).

[39] M. Miwa, S. Juodkazis, T. Kawakami, S. Matsuo, and H. Misawa, Applied Physics A-Materials Science & Processing. **73**, 561 (2001).

[40] Y. A. Vlasov, X. Z. Bo, J. C. Sturm, and D. J. Norris, Nature. **414**, 289 (2001).

[41] H. K. Wu, T. W. Odom, D. T. Chiu, and G. M. Whitesides, Journal of the American Chemical Society. **125**, 554 (2003).

[42] G. Binnig, C. F. Quate, and C. Gerber, Physical Review Letters. **56**, 930 (1986).

[43] K. Salaita, S. W. Lee, X. F. Wang, L. Huang, T. M. Dellinger, C. Liu, and C. A. Mirkin, Small. **1**, 940 (2005).

[44] D. Bullen, S. W. Chung, X. F. Wang, J. Zou, C. A. Mirkin, and C. Liu, Applied Physics Letters. **84**, 789 (2004).

[45] J. Haaheim, R. Eby, M. Nelson, J. Fragala, B. Rosner, H. Zhang, and G. Athas, Ultramicroscopy. **103**, 117 (2005).

[46] R. D. Piner, J. Zhu, F. Xu, S. H. Hong, and C. A. Mirkin, Science. **283**, 661 (1999).

[47] S. H. Hong, J. Zhu, and C. A. Mirkin, Science. **286**, 523 (1999).

[48] S. H. Hong and C. A. Mirkin, Science. **288**, 1808 (2000).

[49] S. W. Lee, R. G. Sanedrin, B. K. Oh, and C. A. Mirkin, Advanced Materials. **17**, 2749 (2005).

[50] L. Fu, X. G. Liu, Y. Zhang, V. P. Dravid, and C. A. Mirkin, Nano Letters. **3**, 757 (2003).

[51] J. M. Nam, S. W. Han, K. B. Lee, X. G. Liu, M. A. Ratner, and C. A. Mirkin, Angewandte Chemie-International Edition. **43**, 1246 (2004).

[52] J. Jang, G. C. Schatz, and M. A. Ratner, Phys Rev Lett. **90**, 156104 (2003).

[53] P. E. Sheehan and L. J. Whitman, Phys Rev Lett. **88**, 156104 (2002).

[54] C. R. Lowe, Current Opinion in Structural Biology. **10**, 428 (2000).

[55] M. H. Hong, S. M. Huang, B. S. Luk'yanchuk, and T. C. Chong, Sensors and Actuators A-Physical. **108**, 69 (2003).

[56] V. Grigaliunas, S. Tamulevicius, R. Tomasiunas, V. Kopustinskas, A. Guobiene, and D. Jucius, Thin Solid Films. **453-54**, 13 (2004).

[57] V. Grigaliunas, D. Jucius, S. Tamulevicius, A. Guobiene, and V. Kopustinskas, Appl Surf Sci. **245**, 234 (2005).

[58] A. A. Gorbunov and W. Pompe, Physica Status Solidi A-Applied Research. **145**, 333 (1994).

[59] S. M. Huang, M. H. Hong, B. S. Luk'yanchuk, Y. W. Zheng, W. D. Song, Y. F. Lu, and T. C. Chong, Journal of Applied Physics. **92**, 2495 (2002).

[60] S. M. Huang, M. H. Hong, Y. F. Lu, B. S. Lukyanchuk, W. D. Song, and T. C. Chong, Journal of Applied Physics. **91**, 3268 (2002).

[61] Behrouz Shiari, Ronald E. Miller, and Dennis D. Klug, Journal of the Mechanics and Physics of Solids. **55**, 2384 (2007).

[62] In-Ha Sung and Dae-Eun Kim, Ultramicroscopy. **107**, 1 (2007).

[63] Narayanan Ramakrishnan, Patrick B. Chu, Earl C. Johns, Yongjun Zhao, and Xiaoping Yan, Sensors and Actuators A: Physical. **145-146**, 214 (2008).

[64] K. Hokkirigawa and K. Kato, Tribology International. **21**, 51 (1988).

[65] J. F. Archard, Journal of Applied Physics. **24**, 981 (1953).

[66] J. B. Adams, L. G. Hector, D. J. Siegel, H. L. Yu, and J. Zhong, Surface and Interface Analysis. **31**, 619 (2001).

[67] F. Iwata, Y. Suzuki, Y. Moriki, S. Koike, and A. Sasaki, J Vac Sci Technol B. **19**, 666 (2001).

[68] W. S. Kim, J. K. Kim, and P. Hwang, J Electron Mater. **30**, 503 (2001).

[69] W. Lu and K. Komvopoulos, Journal of Tribology-Transactions of the ASME. **123**, 717 (2001).

[70] T. Tokai, S. Umemura, S. Hirono, A. Imoto, and R. Kaneko, Surface & Coatings Technology. **169**, 475 (2003).

[71] S. Umemura, S. Hirono, Y. Andoh, and R. Kaneko, Journal of the Japan Institute of Metals. **67**, 286 (2003).

[72] B. Bhushan, Wear. **250**, 1105 (2001).

[73] M. W. Bai, K. Kato, N. Umehara, Y. Miyake, J. G. Xu, and H. Tokisue, Surface & Coatings Technology. **126**, 181 (2000).

[74] M. A. Baker and J. Li, Surface and Interface Analysis. **38**, 863 (2006).

[75] R. Berger, Y. Cheng, R. Forch, B. Gotsmann, J. S. Gutmann, T. Pakula, U. Rietzler, W. Schartl, M. Schmidt, A. Strack, J. Windeln, and H. J. Butt, Langmuir. **23**, 3150 (2007).

[76] A. Ghorbal, S. Bistac, and M. Schmitt, Journal of Polymer Science Part B-Polymer Physics. **44**, 2449 (2006).

[77] Bharat Bhushan and Kwang Joo Kwak, Nanotechnology. **18**, 345504 (2007).

[78] K. H. Chung, Y. H. Lee, D. E. Kim, J. Yoo, and S. Hong, IEEE Transactions on Magnetics. **41**, 849 (2005).

[79] K. Degiampietro and R. Colaco, Wear. **263**, 1579 (2007).

[80] R. Ribeiro, Z. Shan, A. M. Minor, and H. Liang, Wear. **263**, 1556 (2007).

[81] T. Kayaba and K. Kato, Asle Transactions. **24**, 164 (1981).

[82] S. Guruzu, M. Kulkarni, S. Ingole, G. Xu, C. Chen, and H. Liang, Wear. **259**, 524 (2005).

[83] *Merriam-Webster Dictionary*. (2002).

[84] R. Ferrando, J. Jellinek, and R. L. Johnston, Chemical Reviews. **108**, 845 (2008).

[85] F. Congiu, G. Concas, G. Ennas, A. Falqui, D. Fiorani, G. Marongiu, S. Marras, G. Spano, and A. M. Testa, Journal of Magnetism and Magnetic Materials. **272-76**, 1561 (2004).

[86] B. Rodriguez-Gonzalez, A. Burrows, M. Watanabe, C. J. Kiely, and L. M. L. Marzan, Journal of Materials Chemistry. **15**, 1755 (2005).

[87] P. Mulvaney, Langmuir. **12**, 788 (1996).

[88] S. C. Tjong and H. Chen, Materials Science & Engineering R-Reports. **45**, 1 (2004).

[89] F. Y. Chen and R. L. Johnston, Appl Phys Lett. **90** (2007).

[90] F. Y. Chen and R. L. Johnston, Acs Nano. **2**, 165 (2008).

[91] F. Y. Chen and R. L. Johnston, Appl Phys Lett. **92**, 023112 (2008).

[92] R. Nazir, M. Mazhar, M. J. Akhtar, M. R. Shah, N. A. Khan, M. Nadeem, M. Siddique, M. Mehmood, and N. M. Butt, Nanotechnology. **19**, 185608 (2008).

[93] V. Abdelsayed and M. S. El-Shall, Journal of Chemical Physics. **126**, 024706 (2007).

[94] H. Kim and J. Cho, Electrochimica Acta. **52**, 4197 (2007).

[95] H. Kim and J. P. Cho, J Electrochem Soc. **154**, A462 (2007).

[96] H. J. Chen, Z. W. Li, Z. S. Wu, and Z. J. Zhang, Journal of Alloys and Compounds. **394**, 282 (2005).

[97] S. Senapati, A. Ahmad, M. I. Khan, M. Sastry, and R. Kumar, Small. **1**, 517 (2005).

[98] F.P. Bowden and D. Tabor, *The Friction and Lubrication of Solids*. (Clarendon Press, Oxford, 1958).

[99] J. M. Martin, Tribol Lett. **6**, 1 (1999).

[100] J. A. Stroscio and D. M. Eigler, Science. **254**, 1319 (1991).

[101] A. Hiraki, A. Shimizu, M. Iwami, T. Narusawa, and S. Komiya, Applied Physics Letters. **26**, 57 (1975).

[102] K. Nakashima, M. Iwami, and A. Hiraki, Thin Solid Films. **25**, 423 (1975).

[103] A. Cros and P. Muret, Mater Sci Rep. **8**, 271 (1992).

[104] Rabinowi.E, Sci Am. **218**, 91 (1968).

[105] T. E. Fischer and W. M. Mullins, J Phys Chem-Us. **96**, 5690 (1992).

[106] T. E. Fischer and H. Tomizawa, Wear. **105**, 29 (1985).

[107] H. Liang, T. E. Fischer, M. Nauer, and C. Carry, J Am Ceram Soc. **76**, 325 (1993).

[108] T. E. Fischer, Annu Rev Mater Sci. **18**, 303 (1988).

[109] Gerhard Heinicke, *Tribochemistry*. (Carl Hanser, Munchen, 1984).

[110] J. M. Martin and T. LeMogne, Analusis. **25**, M28 (1997).

[111] D. A. Rigney and J. E. Hammerberg, Mrs Bull. **23**, 32 (1998).

[112] R. G. Pearson, *Chemical Hardness*. (Wiley-VCH Verlag GmbH Weinheim, 1997).

[113] F. G. Yost, J Electron Mater. **3**, 353 (1974).

[114] H. Kato, J Electrochem Soc. **134**, 1750 (1987).

[115] A. Hiraki, Jpn J Appl Phys 1. **22**, 549 (1983).

[116] C. D. Thurmond and M. Kowalchik, At&T Tech J. **39**, 169 (1960).

[117] M. K. Sunkara, S. Sharma, R. Miranda, G. Lian, and E. C. Dickey, Appl Phys Lett. **79**, 1546 (2001).

[118] J. Westwater, D. P. Gosain, S. Tomiya, S. Usui, and H. Ruda, J Vac Sci Technol B. **15**, 554 (1997).

[119] X. F. Duan and C. M. Lieber, Adv Mater. **12**, 298 (2000).

[120] S. Q. Feng, D. P. Yu, H. Z. Zhang, Z. G. Bai, and Y. Ding, J Cryst Growth. **209**, 513 (2000).

[121] G. Xu and H. Liang S. Guruzu, *Friction-Induced Nucleation of Nanocrystals*. (Springer, AA Dordrecht, 2006).

[122] S. Ingole, A. Schwartzman, and H. Liang, Journal of Tribology-Transactions of the Asme. **129**, 11 (2007).

[123] H. Liang, J. M. Martin, and T. Le Mogne, Journal of Applied Physics. **97**, 043525 (2005).

[124] Luohan Peng and Hong Liang, presented at the ASME/STLE International Joint Tribology Conference, Marriott Mission Valley, San Diego, California, 2007 (unpublished).

[125] M. Hansen and E. Anderko, *Construction of Binary Alloys. (second ed.)*. (McGraw-Hill, New York 1958).

[126] B. Satpati, P. V. Satyam, T. Som, and B. N. Dev, Applied Physics A-Materials Science & Processing. **79**, 447 (2004).

[127] M. Kalin, Materials Science and Engineering A-Structural Materials Properties Microstructure and Processing. **374**, 390 (2004).

[128] M. Jin, A. M. Minor, E. A. Stach, and J. W. Morris, Acta Mater. **52**, 5381 (2004).

[129] B. Bokhonov and M. Korchagin, Journal of Alloys and Compounds. **312**, 238 (2000).

[130] A. Hiraki, M. A. Nicolet, and J. W. Mayer, Appl Phys Lett. **18**, 178 (1971).

[131] A. Hiraki, J. W. Mayer, and E. Lugujjo, Journal of Applied Physics. **43**, 3643 (1972).

[132] *Goodfellow Catalog*. (Cambridge, England, 1996/1997).

[133] *Marcus Materials Co. Catalog*. (Internal Material, Newark, New Jersey 2006).

[134] A. M. Minor, E. T. Lilleodden, E. A. Stach, and J. W. Morris, J Electron Mater. **31**, 958 (2002).

[135] A. M. Minor, E. A. Stach, J. W. Morris, and I. Petrov, J Electron Mater. **32**, 1023 (2003).

[136] I. W. Lyo and P. Avouris, Science. **253**, 173 (1991).

[137] J. L. Huang, Y. E. Sung, and C. M. Lieber, Appl Phys Lett. **61**, 1528 (1992).

[138] D. H. Hoffmann, A. Rettenberger, J. Y. Grand, K. Lauger, P. Leiderer, K. Dransfeld, and R. Moller, Thin Solid Films. **264**, 223 (1995).

[139] L. Howald, R. Luthi, E. Meyer, G. Gerth, H. G. Haefke, R. Overney, and H. J. Guntherodt, J Vac Sci Technol B. **12**, 2227 (1994).

[140] P. E. Sheehan and C. M. Lieber, Science. **272**, 1158 (1996).

[141] Y. Kim and C. M. Lieber, Science. **257**, 375 (1992).

[142] U. Landman, W. D. Luedtke, and A. Nitzan, Surf Sci. **210**, L177 (1989).

[143] C. M. Lieber, J. Liu, and P. E. Sheehan, Angewandte Chemie-International Edition in English. **35**, 687 (1996).

[144] S. Fujisawa, Y. Sugawara, S. Morita, S. Ito, S. Mishima, and T. Okada, J Vac Sci Technol B. **12**, 1635 (1994).

[145] S. Nakahara, S. C. Langford, and J. T. Dickinson, Journal of Materials Research. **10**, 2033 (1995).

[146] N. S. Park, M. W. Kim, S. C. Langford, and J. T. Dickinson, Langmuir. **12**, 4599 (1996).

[147] N. S. Park, M. W. Kim, S. C. Langford, and J. T. Dickinson, Journal of Applied Physics. **80**, 2680 (1996).

APPENDIX A

General writing procedure of scanning probe alloying nanolithography (SPAN):

(1) Turn on the main computer and the TV screen

(2) Run the software package—"Cockpit"

(3) Turn on AFM main controller, wait a couple of minutes on synchronization

(4) Mount the probe on to the "L" shape lock on the scanner

(5) Load sample on the sample puck

(6) Click "Start" on the title bar

(7) Retract the tip, load configuration file (should be contact mode for all writing procedures), and linearize the tip position, check two boxes on the pop-up window

(8) Go to "Laser" window, turn the laser beam off

(9) Go to stage window, focus the objective until the image of the tip is shown on the screen (if not, check the zoom, and objective position)

(10) Use coarse approach and follow the instructions on the screen, to bring the probe close to the sample surface

(11) Move the stage to locate point of interest (POI), where the writing will be performed

(12) Go to the "Scan" window, and then choose desired writing distance (d), writing frequency (f), and writing angle (usually 90^{o})

(13) Perform a trial line scan, watch the probe shift until it is stabilized to raster scan

(14) Stop the line scan while the probe is moved to one end

Coarse z-height adjustments:

(15) Go back to “Stage” window, use stage Z control to move the scanner down manually, one click per second (each click makes a 5μm movement)

(16) Carefully watch the tip movement, stop moving the scanner down once a clear bending reflection on the back of cantilever appears

(17) Retract the scanner by clicking the upper arrow until the bending reflection just disappears and the cantilever does not have horizontal movement, which is the point that the probe barely in touch with sample surface

(18) Repeat (15) — (17) once

Fine z-height adjustment:

(19) Go to “Scan” window, click “manually tip up & down” button

(20) In the pop-up window, choose the step size for the tip movement, the step size can go as small as 160nm (usually 1μm is used)

(21) Manually move the tip up and down to finely adjust the distance between the tip and substrate until they are barely in contact

(22) Apply certain load in terms of z deflection

(23) Use timer to set up the time period, then click the “Line scan” button to start raster writing

(24) Stop writing after time is up, record the total time

(25) Retract tip by moving up the scanner, one click per second

(26) Restore the CCD camera by clicking “Zoom out”

(27) Restore the objective and stage by clicking “Change Sample”

(28) Take out the sample and probe

(29) Turn off the main controller

(30) Exit the program and turn off the computer

APPENDIX B

General writing procedure of laser-assisted scanning probe alloying nanolithography (LASPAN):

(1) Turn on the main computer, the TV screen, and the laser (beam is blocked)

(2) Run the software package—"Cockpit"

(3) Turn on AFM main controller, wait a couple of minutes on synchronization

(4) Mount the probe on to the "L" shape lock on the scanner

(5) Load sample on the sample puck

(6) Click "Start" on the title bar

(7) Retract the tip, load configuration file (should be contact mode for all writing procedures), and linearize the tip position, check two boxes on the pop-up window

(8) Go to "Laser" window, turn the laser beam off

(9) Go to stage window, focus the objective until the image of the tip is shown on the screen (if not, check the zoom, and objective position)

(10) Use coarse approach and follow the instructions on the screen, to bring the probe close to the sample surface

(11) Move the stage to locate point of interest (POI), where the writing will be performed

(12) Go to the "Scan" window, and then choose desired writing distance (d), writing frequency (f), and writing angle (usually 90^{o})

(13) Perform a trial line scan, watch the probe shift until it is stabilized to raster scan

(14) Stop the line scan while the probe is moved to one end

Coarse z-height adjustments:

(15) Go back to “Stage” window, use stage Z control to move the scanner down manually, one click per second (each click makes a 5μm movement)

(16) Carefully watch the tip movement, stop moving the scanner down once a clear bending reflection on the back of cantilever appears

(17) Retract the scanner by clicking the upper arrow until the bending reflection just disappears and the cantilever does not have horizontal movement, which is the point that the probe barely in touch with sample surface

(18) Repeat (15) — (17) once

Fine z-height adjustment:

(19) Go to “Scan” window, click “manually tip up & down” button

(20) In the pop-up window, choose the step size for the tip movement, the step size can go as small as 160nm (usually 1μm is used)

(21) Manually move the tip up and down to finely adjust the distance between the tip and substrate until they are barely in contact

(22) Apply certain load in terms of z deflection

External laser integration and

(23) Turn off the AFM illuminator and pull it out of AFM

(24) Introduce laser beam through the open inlet path

(25) Apply the maximum attenuation through the double spinner attenuator

(26) Use AFM objective to coarsely center the green laser dot onto AFM cantilever

(27) Use the mirror screws to finely center the green laser dot onto AFM cantilever

(28) Insert filter and reduce laser attenuation by double spinner attenuator

(29) Block the laser beam by a paper clip before it hits the AFM probe

(30) Use the power meter to measure the output laser power at the AFM objective

(31) Finely adjust the output laser power by the half way plate until it reaches the a testing power (normally around 10mW)

(32) Turn off the room light and remove the paper clip, watch a blackbody radiation induced flash dot on the cantilever in the screen. If a flash dot is appearing, move to next step, if not repeat steps (23) – (32) until the flash dot is seen

(33) Adjust the output laser power to the designated power

LASPAN writing

(34) Use timer to set up the time period, then click the “Line scan” button to start raster writing

(35) Stop writing after time is up, record the total time

(36) Retract tip by moving up the scanner, one click per second

(37) Restore the CCD camera by clicking “Zoom out”

(38) Restore the objective and stage by clicking “Change Sample”

(39) Take out the sample and probe

(40) Turn off the main controller

(41) Exit the program and turn off the computer

VITA

Luohan Peng received his Bachelor of Science degree in physics from Wuhan University in China in 2002. He entered the physics program at Texas A&M University in September 2002 and received his Master of Science degree in May 2005. In his master degree, he completed all the fundamental general physics coursework at graduate level. Luohan Peng enrolled in the Materials Science and Engineering program at Texas A&M University in June 2005, and worked with Dr. Hong Liang from the Mechanical Engineering Department. He has been a graduate teaching assistant (later teaching assistant coordinator) for four-and-a-half years. His research interests include nanofabrication and instrumentation of materials characterization, and semiconductor processing.

Mr. Peng may be reached at the Materials Science and Engineering Program, 3003 TAMU, College Station, TX 77843. His email is pengluohan@tamu.edu.